9-2014

Liquid Water Transport in the Reactant Channels of Proton Exchange Membrane Fuel Cells

Rupak Banerjee

R·I·T

Liquid Water Transport in the Reactant Channels of Proton Exchange Membrane Fuel Cells

by

Rupak Banerjee

A dissertation submitted in partial fulfilment of the requirements for the degree of Doctor of Philosophy in Microsystems Engineering

Microsystems Engineering Program
Kate Gleason College of Engineering

Rochester Institute of Technology
Rochester, New York

September 2014

Notice of Copyright

Rupak Banerjee

Title of Dissertation:

Liquid water transport in the reactant channels of proton exchange membrane fuel cells.

Signature of Author: _____ Date:_____

Liquid Water Transport in the Reactant Channels of Proton Exchange Membrane Fuel Cells

by

Rupak Banerjee

We, the undersigned committee members, certify that we have advised the candidate on the work described in this dissertation. We further certify that we have reviewed the dissertation manuscript and approve it in partial fulfillment of the requirements of the degree of Doctor of Philosophy in Microsystems Engineering.

Dr. Satish G. Kandlikar — Date
James E. Gleason Professor, Mechanical Engineering (Advisor)

Dr. Steven Day — Date
Associate Professor, Mechanical Engineering

Dr. Kathleen Lamkin-Kennard — Date
Associate Professor, Mechanical Engineering

Dr. Jiandi Wan — Date
Assistant Professor, Microsystems Engineering

Certified By:

Dr. David A. Borkholder — Date
Director, Microsystems Engineering Program

Dr. Harvey J. Palmer — Date
Dean, Kate Gleason College of Engineering

ABSTRACT

Kate Gleason College of Engineering
Rochester Institute of Technology

Degree: Doctor of Philosophy
Program: Microsystems Engineering
Author: Rupak Banerjee
Advisor: Satish G. Kandlikar

Dissertation Title: Liquid Water Transport in the Reactant Channels of Proton Exchange Membrane Fuel Cells

Water management has been identified as a critical issue in the development of PEM fuel cells for automotive applications. Water is present inside the PEM fuel cell in three phases, i.e. liquid phase, vapor phase and mist phase. Liquid water in the reactant channels causes flooding of the cell and blocks the transport of reactants to the reaction sites at the catalyst layer. Understanding the behavior of liquid water in the reactant channels would allow us to devise improved strategies for removing liquid water from the reactant channels. In situ fuel cell tests have been performed to identify and diagnose operating conditions which result in the flooding of the fuel cell. A relationship has been identified between the liquid water present in the reactant channels and the cell performance. A novel diagnostic technique has been established which utilizes the pressure drop multiplier in the reactant channels to predict the flooding of the cell or the drying-out of the membrane. An ex-situ study has been undertaken to quantify the liquid water present in the reactant channels. A new parameter, the Area Coverage Ratio (ACR), has been defined to identify the interfacial area of the reactant channel which is blocked for reactant transport by the presence of liquid water. A parametric study has been conducted to study the effect of changing temperature and the inlet relative humidity on the ACR. The ACR decreases with increase in current density as the gas flow rates increase, removing water more efficiently. With increase in temperature, the ACR decreases rapidly, such that by 60°C, there is no significant ACR to be reported. Inlet relative humidity of the gases does change the saturation of the gases in the channel, but did not show any significant effect on the ACR. Automotive powertrains, which is the target for this work, are continuously faced with transient changes. Water management under transient operating conditions is significantly more challenging and has not been investigated in detail. This study begins to investigate the effects of changing operating conditions on liquid water transport through the reactant channels. It has been identified that rapidly increasing temperature leads to the dry-out of the membrane and rapidly cooling the cell below 55°C results in the start of cell flooding. In changing the operating load of the PEMFC, overshoot in the pressure drop in the reactant channel has been identified for the first time as part of this investigation. A parametric study has been conducted to identify the factors which influence this overshoot behavior.

Acknowledgements

I begin by expressing my gratefulness to my advisor, Dr. Satish Kandlikar, for all the great opportunity that he has provided to me. It has been a great learning experience to work under his advisement, with his constant encouragement and support to depend on. His enthusiasm and excitement has been a constant source of motivation.

I would like to acknowledge and thank the US – Department of Energy for the support provided to me for my work presented here, under contract number DE-EE0000470. I am thankful to Jon Owejan, Jeffrey Gagliardo and Wenbin Gu of the General Motors for providing guidance, materials and encouragement for the research. Discussions with them always provided new ideas and avenues to explore.

I also express my gratitude to Diane Selleck, Venessa Mitchell, Diedra Livingston and Jill Ehmann of the Mechanical Engineering department and Lisa Zimmerman of the Microsystems Engineering program. They have made it possible for this work to be done, without having to worry about anything else. Dave Hathway, Rob Kraynik and Jon Maneti have always been of utmost help and made the smooth functioning of the lab possible. I would also like to thank our systems administrator Bill Finch, who is always jovial and is always available to help out with any technical difficulties that we run into.

The acknowledgements would be incomplete without a special mention of my parents, my grandmother and my brother, who have been encouraging throughout my years of study. Their unwavering support has made all of this possible.

Dedication

This work is dedicated to my grandmother,

Bina Banerjee.

Nomenclature

BEV	Battery Electric Vehicle
PEM	Proton Exchange Membrane
DOE	US - Department of Energy
GDL	Gas Diffusion Layer
MPL	Micro-Porous Layer
ACR	Area Coverage Ratio
PTFE	Polytetrafluoroethylene (Teflon)
CCL	Cathode catalyst layer
NIST	National Institute of Standards and Technology
MEA	Membrane Electrode Assembly
RH	Relative humidity
ΔP_{peak}	Peak pressure drop
ΔP_{ss}	Steady state pressure drop
ΔP_{MAG}	Magnitude of pressure drop overshoot
t_{ss}	Time to steady state
K_{over}	Percentage Overshoot

Table of Contents

List of Figures

List of Tables

1. Introduction

1.1 Motivation

Fuel costs have risen sharply for the past few decades. The Annual Energy Outlook 2013 predicts the cost of crude oil to increase to double the price of 2010 by the year 2040 [1]. We currently rely on fossil fuels as our primary fuel sources: petroleum products, coal, and natural gas. The share of electricity generation from renewable sources in the US is likely to grow from 13% in 2011 to 16% in 2040. The average electricity price is projected to increase by only 8% during the same period. This places electric vehicles (EVs) at an advantageous position.

With the global focus on reducing our carbon footprint, transportation remains one of the prime domains where emissions need to be controlled. Even with improved fuel efficiency of internal combustion engines and improvements in catalytic convertors, meeting the targets for cutting emissions remains difficult [2]. However, with the focus on improving efficiency and automakers focusing on hybrids, battery electric vehicles (BEVs) and fuel cells, the energy consumption by light duty vehicles has started to decrease (as seen in Figure 1) [3]. Hydrogen may prove to be the required energy carrier, providing a solution to reducing carbon emission from transportation [4]. With hydrogen, non-renewable power generation could be centralized, allowing the release of carbon to be controlled much more easily. Additionally, hydrogen can also be produced using renewable sources [5]. Hydrogen powered vehicles have an advantage over BEVs due to faster refueling times, longer range capability and improved applicability to larger and

heavier modes of transportation. These advantages place hydrogen powered vehicles in a better position than BEVs.

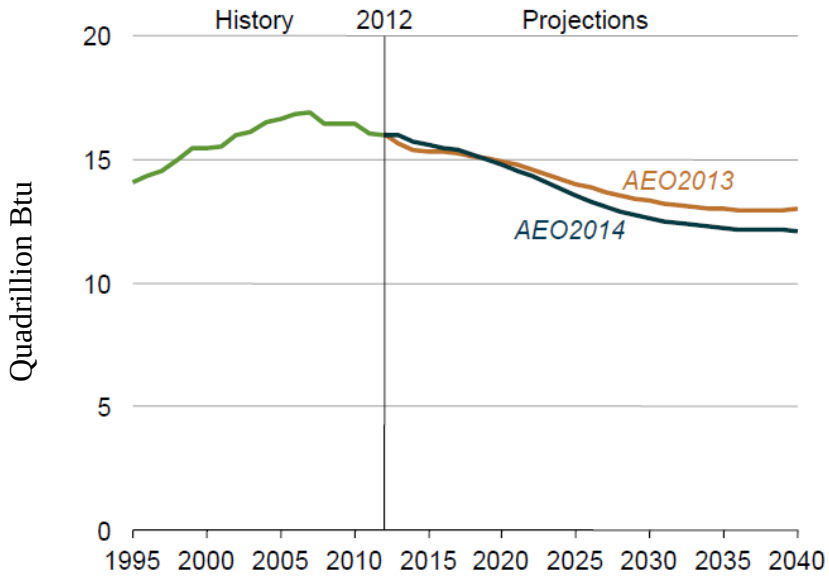

Figure 1: Energy consumption by light duty vehicles. Projections from 2013 and 2014 [3]. Projections have decreased in the 2014 report resulting from improved efficiency of vehicles and an increase in the popularity of hybrids and electric vehicles.

Proton Exchange Membrane fuel cells (PEMFCs) provide a feasible method for generating power from hydrogen for automotive drivetrains. Relatively short start up times, high power density (greater than 2.5 kW/L), low operating temperatures (less than 100°C) and clean exhaust gases make these feasible for the start-stop power requirements of the personal automobile [6–8]. Various auto manufacturers in accordance with the United States – Department of Energy (US-DOE) have selected PEM as their path for foray into developing hydrogen powered vehicles [9].

PEM fuel cells are electrochemical devices which combine hydrogen and oxygen to form water and energy. Maintaining a critical balance between the required liquid water in the

membrane and excess water elsewhere in the system makes water management in PEMFCs an important hurdle to overcome. The transport of the produced liquid water within the cell is of interest in this investigation. The effect of temperature on the cell performance and water management is investigated in this work.

1.2 PEM Fuel Cells

Polymer Electrolyte Membrane fuel cells are electrochemical energy conversion devices which convert chemical energy from the reactants into electrical energy. Given below are the cathode and anode half reactions, which result in the conversion of hydrogen and oxygen into water and energy. 226 kJ of useful energy can be extracted from a single mole of hydrogen with 59 kJ of heat energy being generated in the process. The full reaction below shows a balanced reaction with two moles of hydrogen and therefore doubles the values of useful electrical energy and the generated heat energy.

Anode half reaction:

$$2H_2 \xrightarrow{\text{catalyst}} 4H^+ + 4e^- \quad (1)$$

Cathode half reaction:

$$O_2 + 4H^+ + 4e^- \xrightarrow{\text{catalyst}} 2H_2O \quad (2)$$

Complete reaction:

$$2H_2 + O_2 \xrightarrow{\text{catalyst}} 2H_2O + 452\ \text{kJ (electrical)} + 118\ kJ\ (heat) \quad (3)$$

Figure 2 shows an electrochemical cell which represents an equivalent process. The electrochemical cell has hydrogen and oxygen gases coming in as input to the two electrodes. Hydrogen goes to one of the electrodes while oxygen is supplied to the other electrode. A platinum catalyst coated on the electrodes provides the required activation for the reaction to begin. The hydrogen molecule is split up at the catalyst to form a proton and an electron. The electron follows the path of least resistance through the electrical circuit to the other electrode. The proton goes through the electrolyte to combine with the oxygen atom and the electron to form water at the opposite electrode. By convention, the direction of the electrical current is opposite to the direction of the motion of the electrons, and the electrode from where the electrons move away from is classified as the anode. Thus, the electrode at which hydrogen is introduced is the anode, while the cathode is supplied with oxygen. The product is the electrical energy due to the flow of electrons, and generation of water.

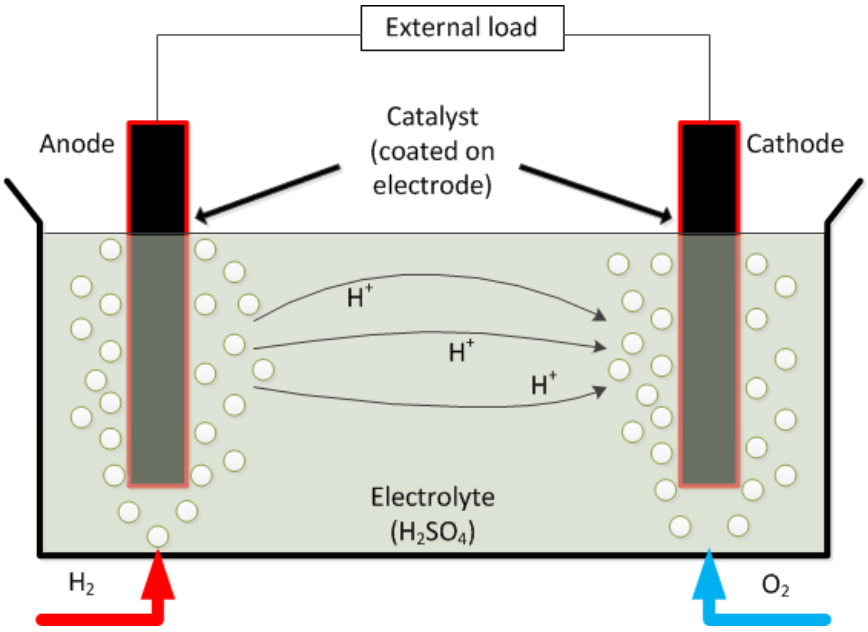

Figure 2: Electrochemical cell representation of the PEM fuel cell.

Figure 3 shows a schematic representation of the PEMFC. Bipolar plates house the reactant flow channels which supply the cell with reactant gases. The gases then diffuse through the gas diffusion layer (GDL) to the reactant sites at the catalyst layer. The half reactions take place on either side of the membrane with water as a by-product of the reaction. As seen in equations (1) - (3), water is produced at the cathode side of the cell. The water travels through the GDL in both liquid and vapor form. The reactant channels are responsible for removing the water from the cell along with supplying the cell with reactants. The flow of liquid water in the channels, along with the gaseous reactants, result in two-phase flow. Managing the product water is a key obstacle in commercialization of PEMFCs for automotive applications. Section 1.3 discusses the water management in greater detail. In depth discussion of fuel cells and their operation can be found in books such as [7,10–12] among others.

The most commonly used method for evaluation of fuel cell performance is through the polarization curve, which shows relationship between current density and the cell voltage relationship [7,10]. Figure 4 shows a typical polarization curve, with power density obtained and the heat generated. Figure 5 shows the polarization curve highlighting the losses experienced by an operating PEMFC. At the lower current densities, the performance is dominated by activation losses. At the mid-range of current densities, performance is dominated by the ohmic losses. At the high current density region, the performance depends on the mass transport losses. Fuel cells are designed to reduce mass transport losses to a minimum, allowing the fuel cell to reach higher current densities.

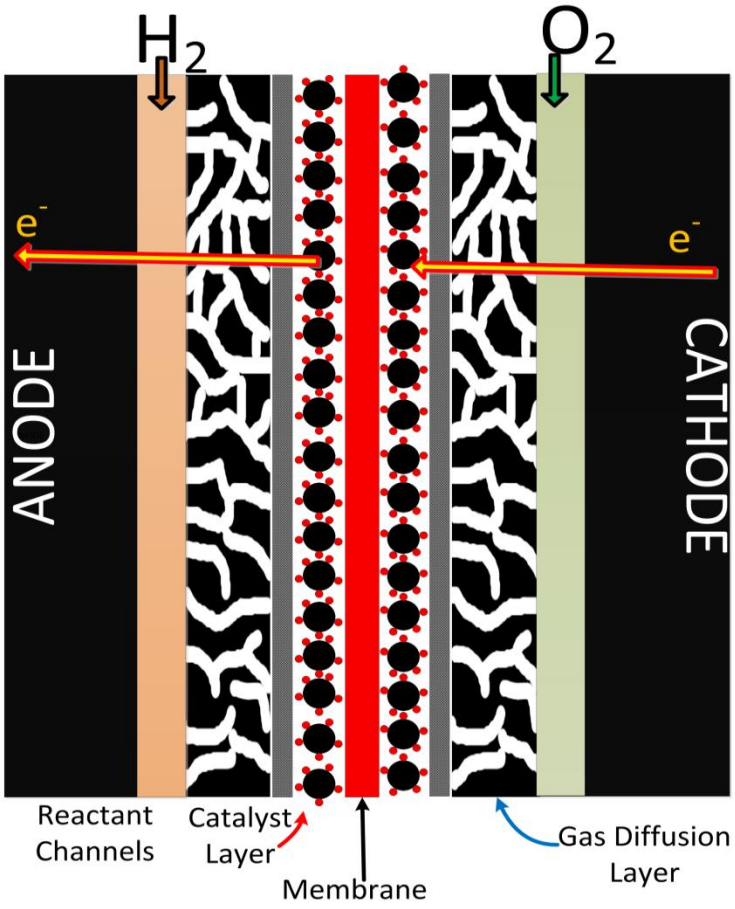

Figure 3: Schematic representation of a PEM Fuel Cell.

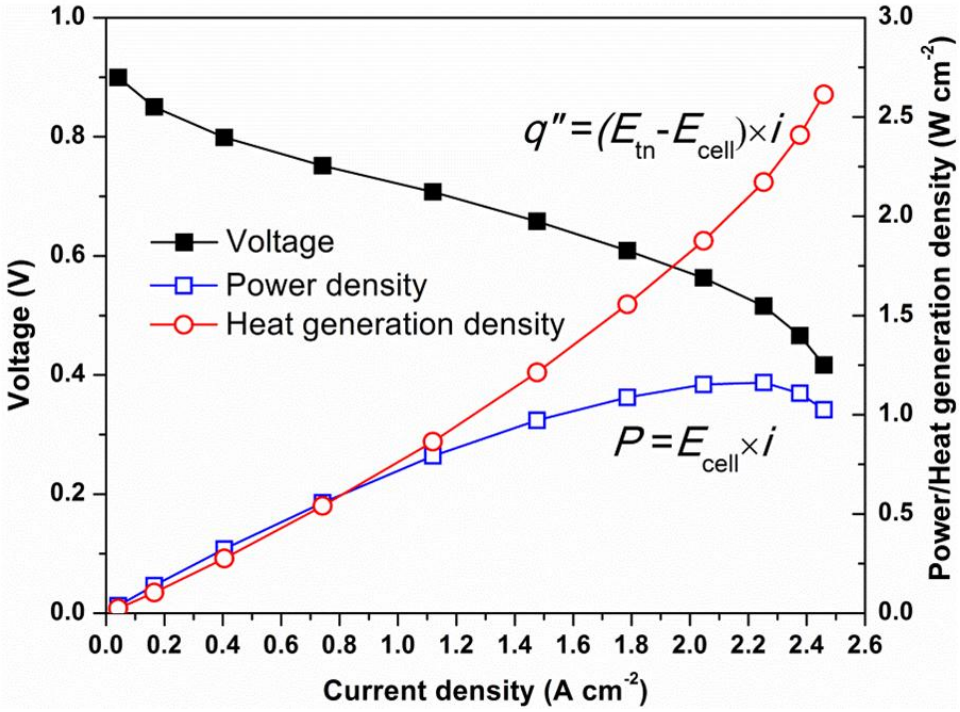

Figure 4: Typical polarization curve for PEMFC characterization showing the cell voltage, power density obtained and the heat generation as a function of the operating current density.

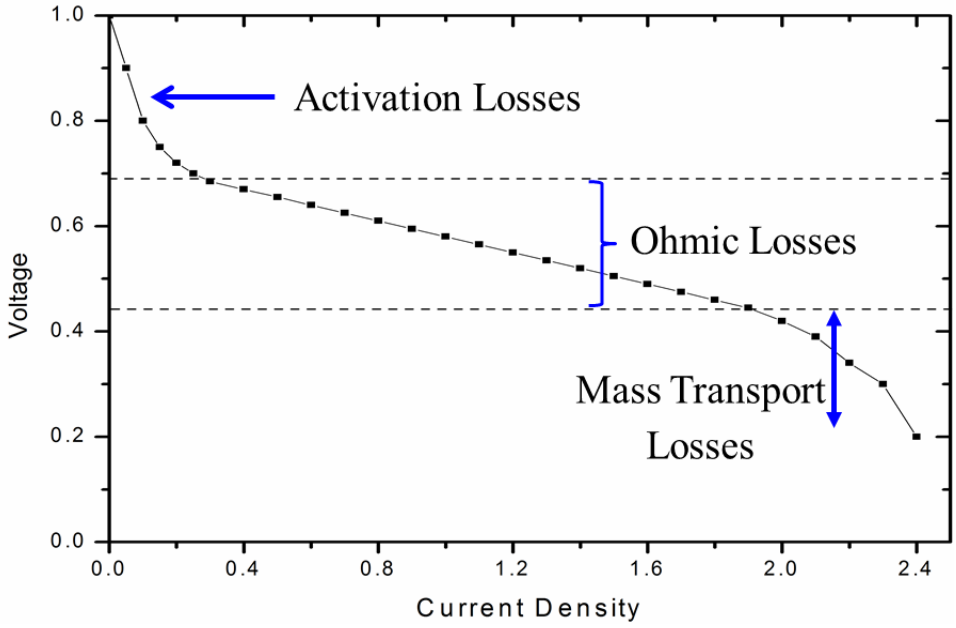

Figure 5: Typical polarization curve for PEMFC characterization showing the three different dominant loss regions - activation, ohmic and mass transport losses.

1.3 Water Management in PEM Fuel Cells

Water management involves multiple factors and remains a highly researched topic within the fuel cell community [6,13–21]. Water is generated on the cathode side catalyst layer and is removed through the GDL into the reactant channels, then exiting the cell.

It is important to note that water management is a challenge in each of the three loss regions shown in Figure 5. However, the challenges in each segment are unique. At the lower current densities (activation loss region), very little water is being produced due to the reaction. If the stoichiometry is kept high, the membrane is likely to suffer from dehydration. Additionally, the gas flow rates are very low, due to the low rate of consumption, leading to two-phase flow blockages, as described in greater detail in section 2.2. In the ohmic loss dominated region of the polarization curve, if the membrane becomes dehydrated, it's ionic resistance increases and leads to an increase in the overall resistance of the PEMFC. If there is excess water within the system, the mass transport resistance increases, leading to a higher overall resistance of the cell. An optimum balance needs to be maintained between the membrane hydration and the system water content. Finally, in the mass transport loss dominated region, the rate at which the reactants are consumed is very high. Any liquid water in the GDL or the reactant channel can significantly impact the concentration of reactants at the catalyst layer. Although the high gas flow rates removes water very efficiently, the high rate of water generation at the catalyst layer keeps the membrane well hydrated.

Water exists in the fuel cell in three different phases [13,22]. In the first phase, water remains absorbed in the membrane. The proton conductivity of the membrane depends on the hydration of the membrane. Higher saturation of the membrane results in higher

conductivity and lower cell resistance [23]. In the second phase, water is present in liquid form, in the catalyst layers, GDL and the gas channels. Liquid water increases the resistance to mass transport through the fuel cell to the reaction sites. This increases the resulting concentration losses and leads to mass transport limited performance from the cell. The presence of excess water within the fuel cell is known as flooding of the cell. In the third phase, water is present in vapor form in the GDL as well as the reactant channels. The saturation pressure of water vapor in the cell depends on the operating temperature. If the gas streams are not fully saturated at the inlet, water is also removed through the reactant channels in the vapor phase.

Maintaining a good balance of water in the different regions of the fuel cell is critical to obtaining a high performance from the cell. If the liquid water generated in the cell is not removed efficiently, the cell is likely to get flooded, increasing the mass transport resistance and therefore lower the performance. On the other hand, if excessive water is removed from the cell using dry gases, the membrane begins to dry out. This results in reduced membrane conductivity and thus lowers cell performance.

1.4 Two-Phase Flow in PEM Fuel Cells

Two-phase flow in PEMFCs exists in different layers of the cell. The liquid water in the catalyst layer and the GDL interact with the reactant gases and compete for pore space for transport through the GDL. Two-phase flow in PEMFCs can be characterized using a number of techniques. Pressure drop is a key method used to observe two-phase flow in the reactant channels [24–26]. The liquid water introduced in the channel interacts with the reactant gases flowing to create two-phase flow. Liquid water in the channel blocks

reactant transport in two domains. The flow down the channel is blocked by slugs / films resulting in an increased pressure drop along the channel. This reduces the reactant flow, causing localized starvation down the channel. Additionally, any liquid water on the surface of the GDL reduces the area available for diffusive reactant transport into the GDL (towards the reactant sites). This leads to mass transport limited performance, which is most significant at the higher current densities. The two forms of resistances are shown schematically in Figure 6.

The channels commonly used in PEM fuel cells have hydraulic diameters less than 1 mm [27]. The conditions of two-phase flow are unique in the PEMFC configuration [28]. Water is introduced along the length of the channel; the gas quality is continuously changing and the volume of liquid is significantly lower than the volume of gases in the channel. One of the four walls of the channel is a porous media (GDL) of very high porosity and a hydrophobic nature. All these factors contribute to make the two-phase flow in PEMFC different from the conventional two-phase flow in macro channels [28–30].

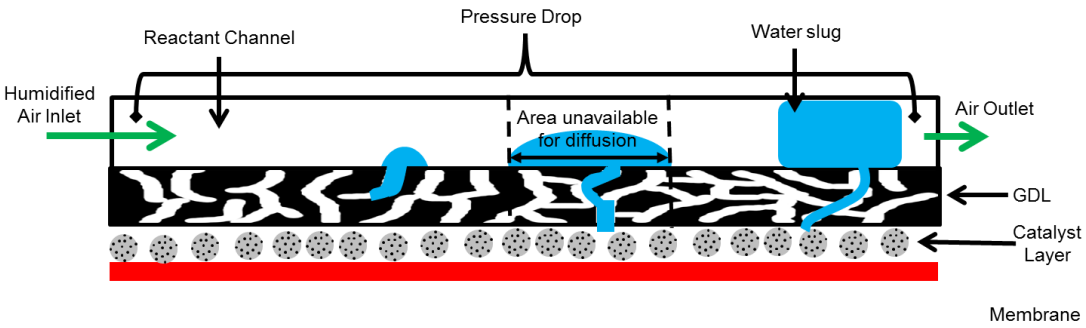

Figure 6: Transport resistance in two perpendicular directions due to presence of liquid water in reactant channels.

Two-phase flow in the reactant channels has different flow patterns. The commonly observed flow patterns in PEMFC channels are slug flow, film flow and mist flow [29,31,32]. Representation of the different types of flow patterns can be seen in Figure 7. Slug flow tends to block the channel and reduces channel area available for reactant transport to the catalyst layer. It also results in large fluctuations of pressure drop. Film flow is a partial constriction of the channel, which too reduces available area for transport. Frequency of fluctuation in pressure drop increases during film flow. Mist flow involves homogenized flow of gas and liquid through the channel. Therefore there is no observable reduction in channel area and the pressure drop remains constant. Figure 8 shows the pressure drop signatures associated with each of the flow patterns discussed here.

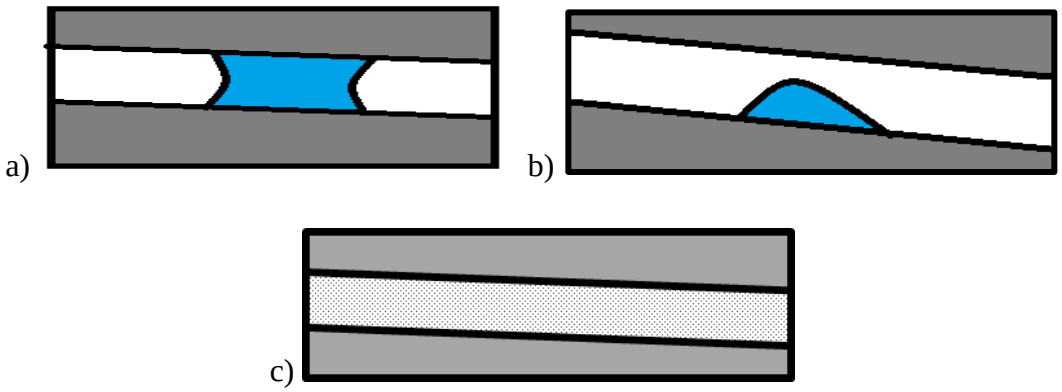

Figure 7: Flow patterns commonly observed in PEMFC reactant channels. (a) slug flow (b) film flow (c) mist flow.

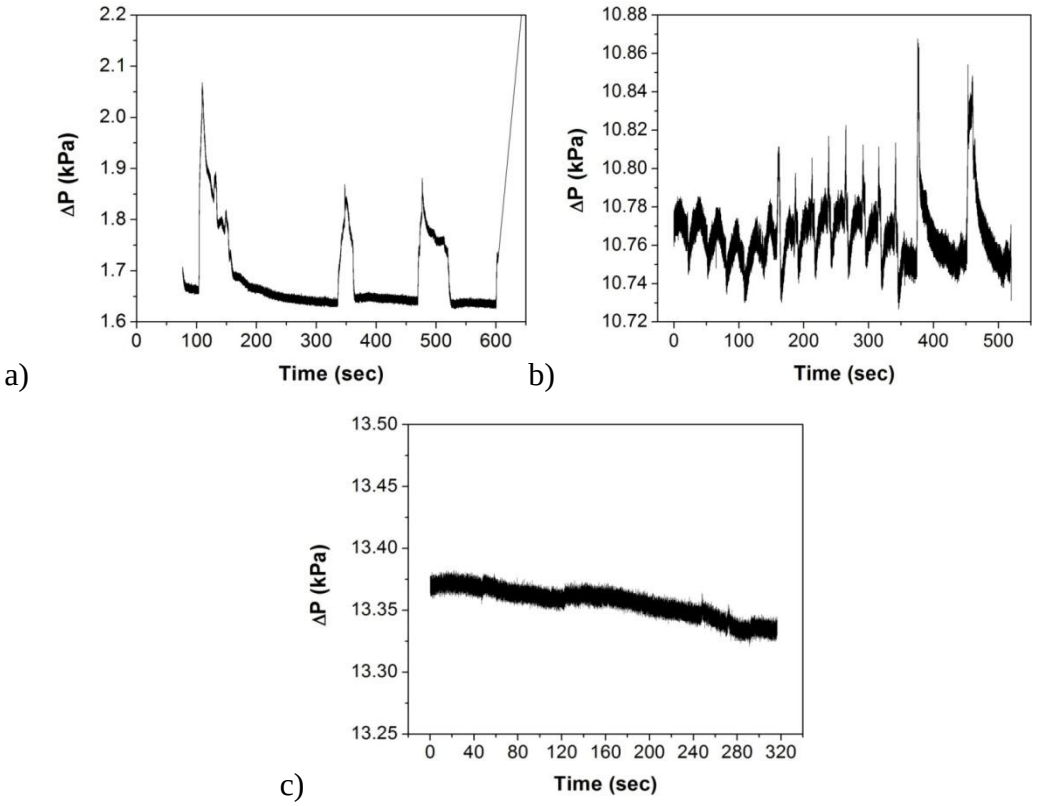

Figure 8: Pressure drop signatures associated with flow patterns commonly observed in PEMFC reactant channels. (a) slug flow (b) film flow (c) mist flow [32].

1.5 Transient Operation of PEM Fuel Cells

The current work focuses on improving the water management of PEMFCs for automotive applications. Automotive transportation power trains are expected to respond to rapid changes in speed / acceleration and therefore are designed for a rapid power output response [33–35]. The water management of fuel cells during transient operating conditions needs investigation as it plays a critical role in the transient power response of a fuel cell.

Currently, PEMFCs are used in conjunction with a conventional battery, which supplements the power during high power demand and stores the excess and regenerated

power during low demand. However, relying on batteries entirely results in excess vehicular weight and lower system efficiency. The requirement for large energy storage devices on board can be reduced significantly by improving the response time from the PEMFC, and making the powertrain “load-following” [35,36].

The transient behavior of PEMFCs can be categorized into three contributors - electrochemical, thermal and two-phase behaviors. Although the three are well interlinked in producing the performance of the cell, they have distinct characteristics which need to be investigated individually. Electrochemical transients are very rapid with transient phenomenon lasting less than 1 second. Comparatively, thermal and two-phase transients occur over longer time periods. The impact of thermal and two-phase transients on the electrochemical performance of the cell needs to be further investigated. After start-up, the PEMFC stack requires some time before it reaches the optimal temperature. Any changes in the operating load of the cell also results in a change in the system temperature, while the coolant system attempts to bring the temperature back to steady target temperature. It had also been shown by See [37] that two-phase flow requires significant amount of time to reach steady state and the fluctuations in the two-phase pressure drop can have direct impact on the performance of the PEMFC. Therefore, a closer look at the two-phase flow in the PEMFC under transient operating conditions is warranted.

1.6 Project Partners

Significant portions of this work completed as part of this dissertation is done to improve our understanding of liquid water transport in the PEM fuel cells. The target application of the work is the utilization of PEM fuel cells in automotive drivetrains. The work was supported by a grant from the US- DOE under contract no. DE-EE0000470. The project was completed in partnership with General Motors, Pennsylvania State University and the University of Tennessee at Knoxville. Several parameters were kept constant between the project partners in order to make results compatible with each other throughout the project. The findings from the project were combined into a pseudo one dimensional (1+1D) down-the-channel fuel cell model incorporating two-phase behavior in the study. The flow field geometry used in this study (and described in a later section) remains constant throughout the studies conducted by the project partners and is considered as the baseline flow field for this project. Similarly, the MRC GDL with 5% PTFE is considered as the baseline GDL. The baseline membrane used in this project is 18 μm thick and sourced from Gore Associates. The main objectives of the project were to generate valuable data for the characterization of the different components and validation of the 1+1D down-the-channel model. RIT was responsible for the two-phase flow modeling in the reactant channels and the coolant channels. PSU was responsible for the protonic transport in the membrane and UT – Knoxville was responsible for an increased understanding of the porous media and the flow through it. The modeling team at General Motors combined these understandings into a comprehensive 1+1D down-the-channel model for performance prediction from PEMFCS. The data generated from the project is

publicly available for the overall growth in the fuel cell community. In order to disseminate the data, the data was placed in easy to use form on www.pemfcdata.org.

1.7 Objectives

This work investigates different aspects related to water management in PEMFCs. The impact of temperature on the water management within fuel cells is crucial to this investigation. In situ and ex-situ experiments have been conducted to understand transport phenomenon within the reactant channels. Operating conditions such as temperature, inlet relative humidity, current density and stoichiometry are altered within the operating range of automotive PEMFCs. The two-phase flow patterns and behavior that is observed is used in understanding the mass transport limitations due to the presence of liquid water.

The loss in performance due to the change in water content in the reactant channels is investigated. Different operating parameters are changed to understand the impact of reactant water on cell flooding and membrane dehydration. Ex-situ experiments are conducted to quantify the liquid water in the reactant channels using a new parameter defined as the area coverage ratio (ACR). The ACR defines the area blocked by the presence of liquid water on the surface of the GDL for transport of oxygen into the GDL and through to the reaction sites at the catalyst layer.

Additionally, in situ experiments have been conducted to investigate the effect of transient changes in two-phase flow (in the PEMFC) on the cell performance. The effect of changing load and temperature on the performance of the cell is investigated. Although

three types of transients are present in PEMFCs, very little focus has been given to two-phase transient behavior. Detailed investigation of two-phase transients in PEMFCs has been conducted as part of this study. The objectives of the study can be summarized as follows:

1. Identify relationship between liquid water content in the reactant channels and performance of PEMFC.
2. Quantify liquid water in the reactant channels, through two-phase flow visualization, as a function of operating temperature and relative humidity.
3. Investigate parameters that affect the transient performance of PEMFCs.
4. Investigate influence of parameters on two-phase transients in PEMFCs.

1.8 Document Layout Overview

This dissertation brings together my work done to investigate the behavior of liquid water in the reactant channels of PEMFCs. Section 2 provides an insight into the pioneering work done by other authors. It provides the details of work done in literature relating to the transport of liquid water in the reactant channels. A summary is provided at the end of the section, followed by the expected contributions from this work. Section 3 begins to delve into the effect of liquid water on the performance of the PEMFC. It is observed that a detailed understanding of the quantity of liquid water in the reactant channels is warranted in improving our understanding of the effect of liquid water on the performance of the cell. Therefore a visualization study is pursued. The visualization study is conducted in an ex-situ (in the absence of the electrochemical reaction) environment and is presented in Section 4 of this document. During the experimental

routines of section 3 and 4, it is observed that significant time is required for the two-phase pressure drop in the PEMFC reactant channels to reach a steady state behavior. The transient behavior of two-phase flow has not been the focus of much work in the literature. Therefore, an exhaustive experimental routine was developed to investigate the factors influencing the two-phase transient behavior in the PEMFC reactant channels. The effect of different transient changes on the PEMFC performance was also explored as part of this investigation. The work done relating to the transient behavior observed in PEMFCs is reported in section 5 of this work.

Each of the sections 3, 4 and 5 has a summary from those findings at the end. All over-arching conclusions are presented in section 6, which combines all the findings from this work and explores the relationships between them. The key contributions of this work are highlighted in section 7, while section 8 lists the publications that have resulted from this work. Section 9 is the bibliography and contains a list of all the works cited throughout the text. The citations, figures and tables are numbered incrementally throughout this work. Finally, section 10 contains the excess matter relevant to this work, but not directly applicable in the text. It also contains the MATLAB® codes used in the quantification study of section 4, data processing techniques used in section 5 and the checklist required to be completed for the success of this dissertation.

2. Literature Review

This section provides a summary of the literature reviewed before proposing the work. Some of the topics touched upon in the introduction (Section 1) will be discussed in greater detail. The current status of our understanding present in current literature is discussed and niche openings are brought forth. In summary, the scope of future work is formed based on the current knowledge of the fuel cell community and the microfluidics community.

2.1. Water management – Effect on PEMFC Performance

Water management in PEMFCs is considered to be a major roadblock to the efficient application to automotive platforms. Water management of PEMFCs has been the focus area of significant research in the past several years. Review papers [13,14,17,18,38] have provided an overview of the work done and have highlighted the need for further investigations into water management. Both excess water and a lack of adequate water in the system lead to loss in performance and durability [39,40]. Water management is important at the different component layers of the PEMFC system [13,14].

Water is generated at the cathode catalyst layer and then transported through the MPL and GDL to the reactant channels, from where it is removed from the cell. Water in the membrane is transported from the anode to the cathode side by electro-osmotic drag, while back diffusion causes water from the cathode side to move towards the anode side due to concentration gradients [41,42]. However, accumulation of liquid water at the

catalyst layer increases mass transport to the reaction sites resulting in an increase in mass transport resistance and a loss in cell performance [13]. Excess liquid water at the catalyst layers is known as cell flooding and is to be avoided for efficient operation of PEMFCs. Li et al. [17] show the impact of cell flooding on the cell performance using polarization curves with different levels of flooding. With increased flooding, the cell performance suffers significantly at the higher current densities. However the study does not describe the cell flooding in terms of the liquid water present which causes the flooding. Different aspects of the cell structure and composition play important roles in the water management capability of the cell, which includes the GDL, its PTFE content, its porosity, the MPL and the design of the flow fields as well as the cathode catalyst layer (CCL).

Flow field design has been shown to play a key role in influencing the water flooding in the channels. Both serpentine and interdigitated flow fields have shown reduced channel flooding compared to straight channel configurations [43]. To target low current density operation, serpentine and interdigitated flow fields are preferred due to better water removal characteristics. However, at the higher gas flow rates, straight parallel channels may be preferred due to the low pressure drop and reduced reactant starvation [17,44]. Serpentine flow fields have reduced flooding and a higher pressure drop associated with them resulting from longer channel lengths compared to equivalent parallel channels. Owejan et al. [40] argued that the large number of channels and shorter channel length associated with parallel channels balance out, resulting in even reactant distribution.

Liquid water in the reactant channels blocks reactant transport in two ways. Liquid water reduces the area available for reactant transport, which can be quantified as Area

Coverage Ratio. Sergi and Kandlikar [45,46] implemented dual visualization of an in situ PEMFC to obtain the ACR on both the anode and cathode sides. Liquid water also increases the pressure drop along the length of the channel, which can be characterized using two-phase multipliers. The two-phase multiplier is the ratio of the two-phase pressure drop to the single-phase pressure drop for a given flow condition as shown by equation 3.

$$\phi_g^2 = \frac{\textbf{Two-Phase Pressure Drop}}{\textbf{Single-Phase Gas Pressure Drop}} = \frac{\Delta P_{2\phi}}{\Delta P_g} \quad (3)$$

Liquid water in the GDL reduces the pores available for reactant transport. With increasing saturation of liquid water in the GDL, it becomes increasingly difficult for reactant transport [47]. Ramos-Alvarado et al. [48] showed that with increased saturation of the GDL, the capillary pressure increases, which indicates an increase in the difficulty of water removal. The higher capillary pressure also means that a higher pressure of reactant gases would be required for their displacement from the pores of the GDL. Jang et al. [49] used numerical modeling to show the loss in performance due to the presence of liquid water in the pores of the GDL.

The optimal temperature of operation for PEMFCs lies between 60 and 80°C [50–52]. Low temperature (below 60°C) operation of PEMFCs are dominated by cell flooding issues due to low saturation pressures of water in air, resulting in poor water removal rates in the vapor form. At the higher temperatures, with high saturation pressure of water in air, all the water being produced can be removed in vapor form in the cathode gas stream. This tends to decrease the hydration of the membrane, thereby reducing the membrane conductivity and performance of the cell [14,53,54].

For maintaining an adequate level of hydration in the membrane, the inlet gas streams on both the anode and cathode sides are humidified to a certain extent [55]. The dew point temperatures for the inlet gas streams should always be maintained below the cell temperatures (partially humidified gas stream) to ensure that water does not begin to condense out in the reactant channels increasing the two-phase pressure drop. Therefore, the cell needs to be operated up to temperatures of 80°C, with adequate levels of humidification, for optimum performance.

Multiple authors have worked at identifying the effects of operating conditions on the cell performance. Temperature has a strong impact on the cell performance [55–61]. Cell performance increases with temperature. However, the trend reverses at temperatures above 80°C as shown by Yan et al. [56,57]. This is attributed to a variety of reasons [57,59,61] such as increased gas diffusivity, membrane conductivity, improved kinetics of the oxygen reduction reaction (ORR) and hydrogen oxidation reaction (HOR) along with increased removal of water in the vapor phase in the reactant gas streams.

In the automotive setting, the PEM fuel cell operates at about 20% of the rated power of the fuel cell stack [40], for most of the time (during highway cruising and normal city driving). This operation is dominated with low current densities, low gas flow rates and low heat generation. Low heat generation indicates that the temperature of the cell will not reach optimum operation temperature of at least 60°C during short trips. Hence, it becomes imperative to investigate the water transport characteristics at the lower temperatures below 60°C.

Increasing the operating temperature leads to the problem of membrane dehydration. Zhang et al. [23] showed an increase in the resistance of the membrane at the higher temperatures of operation for low inlet RH. Therefore, inlet RH of the reactant gases plays a key role in dictating the performance of PEMFCs. Multiple works have shown that there is a distinct improvement in the performance of the cell with increase in the cell humidity [23,57–59,61–63], although Yan et al. [57] and Tohidi et al. [61] indicate that a fully humidified cathode stream results in a decreased performance. This could be attributed to the loss in water removal capability resulting in flooding conditions. Sahel et al. [63] suggested the use of asymmetric inlet RH among the anode and cathode sides to optimize the fuel cell performance. They highlighted that a lower inlet RH is preferred at the lower temperatures, while a higher inlet RH is to be used at the higher temperatures.

Reactant gases are consumed along the length of the active area. As more of the gases are consumed, there is little reactant concentration left near the outlet of the flow field. This can result in uneven reactant distribution, uneven current densities leading to lower performance and the generation of hot spots. All of this is detrimental to the overall durability of the cell and lower output performance. To counter this, an even reactant distribution is sought and the inlet gases are usually supplied at a higher stoichiometry to avoid reactant starvation towards the end of the active area. With increase in stoichiometry, air flow velocities are higher within the reactant channels. High flow velocities are more effective at removing water from the reactant channels as shown by low ACR at the high current densities in [46] and also by the transition to mist flow at the higher air flow velocities [32,64]. Therefore higher stoichiometric ratios help in water removal and improve the current distribution. However, maintaining a high stoichiometry

comes with its disadvantages. An increase in the stoichiometry on the anode side results in unused hydrogen being sent out of the exhaust, resulting in unused fuel and increased operating costs. The increase in cathode side stoichiometry does not involve additional fuel costs as the air is obtained from the atmosphere; however the increased pressure drop in the system results in increased pumping power and higher parasitic losses. This means the total system efficiency decreases. Hence, an optimized stoichiometric ratio needs to be maintained during the operation of the cell.

PEMFC stacks are also operated at different operating pressures [55,57–59,61]. Increasing the operating pressure of the cell increases the partial pressure of the reactants thereby increasing the concentration of reactants available for consumptions. This results in an increase in the performance of the cell. However, the change in operating pressure does not play any significant role in the water management of the PEMFC.

Some of the major concerns of water management involving the presence of water in the reactant channels arise from the blockage of channel by liquid water resulting in high pressure drop and parasitic power losses and reduced interfacial area for the diffusion of gases into the GDL. Both these can lead to reactant starvation, non-uniform current distribution, and localized hot-spots, enhancing the chances of MEA degradation [65].

A number of diagnostic tools have been used in the investigation of water management in PEM fuel cells [24–26,66–68] including different forms of visualization techniques as reviewed by Daino and Kandlikar [69] and Bazylak [70]. Although visualization provides an insight into the dynamics of the two-phase flow, the PEMFC needs to be modified for most visualization methods. In 2005, Kramer et al. [71] reported the effect of liquid water

in the fuel cell on the cell performance. As the liquid volume increased, the cell performance suffered. Owejan et al. [72] also focused on the impact of presence of liquid water on the cell performance. They used different GDL samples in an operating cell and visualized it using neutron radiography. Toray showed the highest mass of water in the system and resulted in the poorest performance of the different GDL samples tested. Other studies have also used neutron radiography [73–78] to study the presence of liquid water in the PEMFC, but without any direct comparison with the cell performance. Similarly, X-ray radiography has also been used in the visualization of water in PEMFCs [20,79–83]. However, as the x-ray studies focus on the water emergence at the pore scale, the overall impact on performance has not been reported. The same is also true for optical imaging, which evaluates the water content in the reactant channels without correlating it to the performance of the cell [43,46,84–86]. Visualization techniques are good for obtaining trends in water transport. However, these do not serve as a good diagnostic tool for operating fuel cells and stacks. Further discussion of visualization studies is provided in a future section.

Pressure drop has been shown to be a good diagnostic tool for identifying the presence of liquid water in the PEMFC [24–26], and can be used without any significant modification to the operating fuel cell. A number of investigations have related the loss in performance due to flooding of the cell. The above investigations delve into different factors which impact the cell performance and the water management within the PEMFC. However, a direct relationship between the quantity of liquid water present in the reactant channels and the loss in cell voltage has not been presented in literature. This provides a niche

research direction, to obtain a direct relationship between the presence of liquid water in the reactant channels and the cell performance.

2.2.Two-Phase Flow in PEM Fuel Cell Reactant Channels

Liquid water is introduced into the channel, along the length, through the GDL. The combined flow of liquid water and reactant gases in the channels of PEMFCs create the two-phase flow. The two-phase flow in PEMFC reactant channels have been an area of interest in order to identify, quantify and minimize the mass transport resistances introduced due to the two-phase flow [28–30,32,64,65,84,87–92]. Various researchers have investigated the two-phase flow behavior through visualization. The visualization studies have been discussed in detail in the next section (Section 2.3).

Different pressure drop models have been used to predict the two-phase pressure drop in PEMFCs. However, most models do not predict the pressure drop in the reactant channels of PEMFCs with accuracy as shown by English and Kandlikar [93]. Most of the two-phase pressure drop models mentioned by English and Kandlikar were developed for large tubes and ducts and therefore do not take microscale effects into consideration. Additionally, the two-phase flow in PEMFC reactant channels have unique properties such as continuous water introduction along the length of the channel, reactant consumption, change in liquid quality in the reactant channels, evaporation of liquid water into the reactant stream, condensation of vapor due to change in temperature among others [28,29,37,38]. The channel itself is also bounded on one side by a porous wall (GDL), with a very hydrophobic tendency.

Several in situ and ex situ studies have been used to investigate the two-phase interactions in the microchannels of PEMFCs [32,45,64,87,91,94–97]. The increase in pressure drop is non-linear in nature [37,87] for two-phase flows with increasing gas flow rate. However, the single-phase pressure drop associated with the same gas flow rates is inherently linear. Therefore, the two-phase pressure drop gas multiplier (Equation 3) is used to compare the two-phase behavior in PEMFC reactant channels. The single-phase pressure drop associated with flow in the microchannels can be obtained analytically using equation 4 and 5 obtained from Kandlikar et al. [98].

$$\Delta P = \frac{2f\rho u^2 L}{D_h} \tag{4}$$

where f is the friction factor, ρ is the density of air, u is the gas velocity, L is the length of the channel and D_h is the hydraulic diameter of the channel. The expression can be expanded to be written out as

$$\Delta P = \frac{2uL\mu(Po)}{D_h^2} \tag{5}$$

where Po is the Poiseuille number, which depends on the flow geometry.

Two-phase flow patterns in the reactant channels have a major impact on the pressure drop in the channels. The flow patterns are characteristic of the interaction between the gas phase and the liquid phase. Experimental data on two-phase pressure drop can be presented in the form of flow pattern maps [29,32,37,45,64]. It is observed that there is a decrease in the two-phase multiplier with increase in superficial gas velocity in the reactant channels [37,99]. Therefore, with increase in the superficial gas velocity, there is a reduced impact of the liquid water present in the reactant channels.

Slug flow remains dominant at the lower gas flow rates and introduces a large pressure drop multiplier. With increasing gas flow rate, film flow becomes the dominant flow pattern and results in a lowered liquid impact on the two-phase flow. This is observed through a lowered two-phase multiplier. When the gas flow rate is further increased, the flow goes into mist flow, which is characterized by small droplets of water flowing within the main gas stream and results in a very small resistance to the flow due to the liquid water. This can be seen with a very low two-phase multiplier (near unity). Figure 9 shows the two-phase flow patterns obtained from an in situ study by See [37], clearly distinguishing the three flow patterns discussed here.

Figure 10 shows the two-phase pressure drop gas multipliers obtained from experimental routines by See [37] and Anderson [94]. It can be observed from their results that with an increase in the operating current density, the pressure drop multiplier decreases rapidly to reach an asymptotic value of near unity. This demonstrates that with increasing current densities, there is an increase in the impact of the increased gas flow rates, and that the impact of liquid water in the reactant channels is significantly reduced.

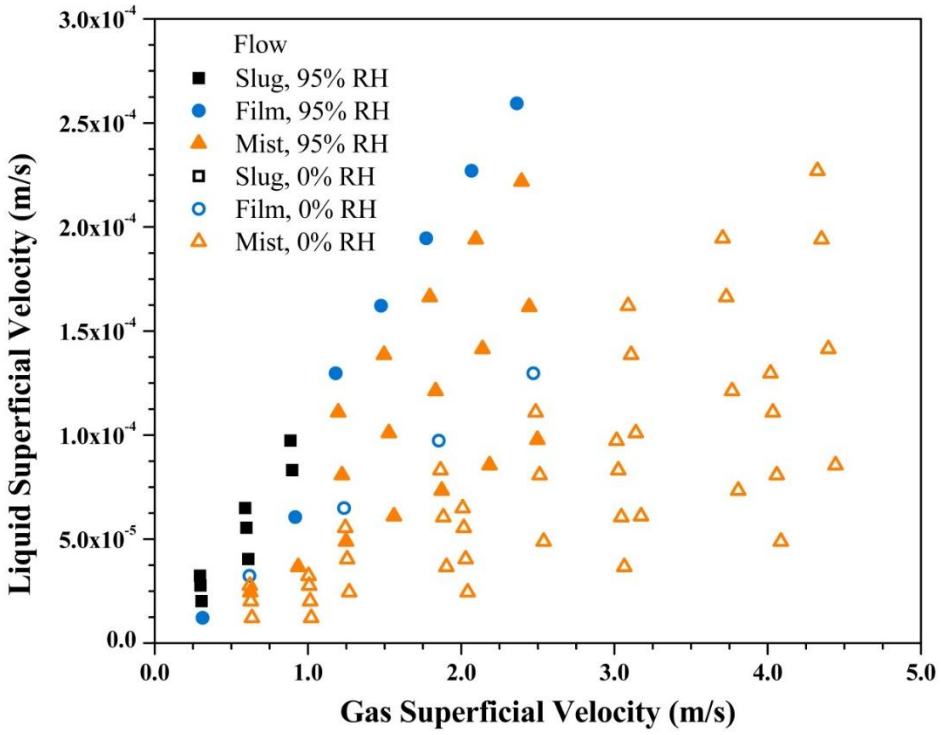

Figure 9: Flow pattern map over a range superficial water and gas velocities at dry and fully humidified inlet conditions [37].

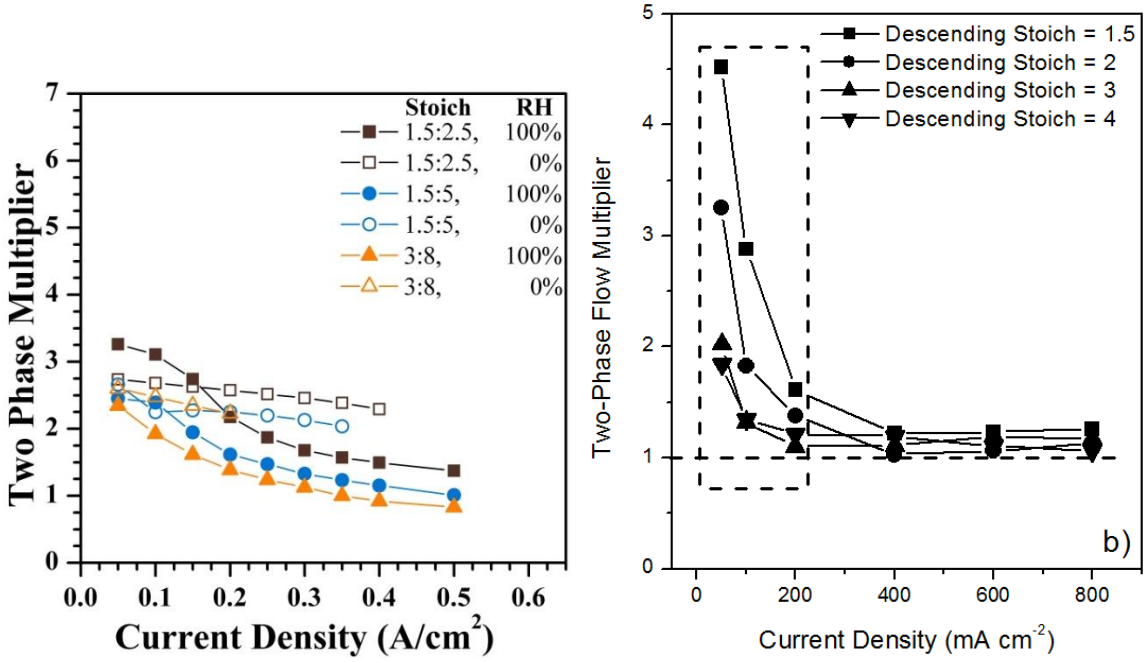

Figure 10: Two-phase pressure drop multiplier from experimental investigations by See [37] (left) and Anderson [94](right).

The visualization of two-phase flow provides an opportunity to understand the dynamics of the liquid flow within the reactant channels. The following section delves into the visualization techniques used in investigation two-phase flow in PEM fuel cell reactant channels.

2.3. Visualization of PEMFC Water Content

In characterizing the two-phase flow in PEMFCs reactant channels, the visualization of two-phase flow plays an important role. Different visualization techniques have been used to investigate the liquid water present in the reactant channels [69,70].

Neutron imaging has been successfully used in studying the presence of water in PEMFCs [40,71–78]. Water has high interaction with the neutrons, whereas PEMFC materials have low interactions. Obtaining a high spatial resolution with neutron imaging is extremely difficult due to the absence of optical lenses, and is limited by the spread of the scintillator light. Different authors have tried to obtain neutron radiographs to quantify liquid water. Trabold et al. [74] used neutron radiography in 2006 to image an active area of 50 cm^2. The spatial resolution obtained was approx. 250 μm per pixel.

Satija et al. [76] had also used the neutron imaging facility at NIST, and obtained a spatial resolution of 160 μm and a temporal resolution of 2 seconds per image. The temporal resolution is too low for rapidly moving objects, which may travel at up to 1 m/s and would display as a thin film, leading to incorrect conclusions [78]. Satija et al. [76] also conducted a tomography study using the neutron imaging system. The time

required for obtaining a tomographic image is between several minutes and several hours. They established that the dynamic nature of the water in the PEM system invalidated tomography data.

Kramer et al. [71] used neutron imaging to investigate liquid water in the flow fields, achieving a spatial resolution of 115 μm / pixel. The lowest temporal resolution used was 2 frames per second (fps). Their tests were performed at the neutron radiography facility NEUTRA, Paul Scherrer Institute, Villigen, Switzerland.

There are very few Neutron radiography centers worldwide, and the technique is rather expensive to execute. The low spatial resolution attainable makes it further unsuitable for quantifying liquid water in the reactant channels. Even with the 115 μm/pixel, each channel width would be represented by only 6 pixels (~700 μm). This is too low to quantify the water accurately. Therefore, neutron imaging, best suited to measure saturation of GDL or the MEA, would not be as accurate for quantifying liquid water in the flow fields.

X-rays have also been used for imaging of fuel cells [20,79–83,100]. However, as metals attenuate the high energy waves, modifications must be made to enable the x-rays to pass through. Manke et al. [79] utilized the high spatial resolution to study the formation of liquid water inside the single pores of GDL. The work, conducted at synchrotron BESSY in Berlin, allowed a spatial resolution as low as 3 μm. The temporal resolution obtained was over 4 seconds per image. This work brought focus upon the transport of liquid water within the GDL and its emergence into the channel.

Lee et al. [80] utilized the Pohang Light Source, Pohang (Korea), in their quantification study of water evolution using X-rays. The facility had a spatial resolution capability of 1 μm. The work focused on the temporal change of liquid water in the gas channels from the in-plane direction. Images were captured at intervals of 3 minutes to measure the liquid water in the channels. They showed that although the voltage and the anode water accumulation reach a steady state within the first 30 minutes, water accumulation in the cathode side channels don't reach steady state even after 60 minutes of operation. High temporal resolution can also be obtained using x-rays, but at the cost of spatial resolution.

Lee et al. [100] used the Biomedical Imaging and Therapy Beam line at the Canadian Light Source Inc. They struck a balance between the temporal and spatial resolutions by obtaining ~ 3 seconds per image and 8 – 10 μm/pixel respectively. The authors investigated the effect of MPL on the water transport through the GDL showing reduction in flooding and improved water transport mechanisms.

Dunbar and Masel [101] used magnetic resonance imaging to study water distribution. A 3D water concentration profile was reported for the operational fuel cell. They successfully demonstrated that the majority of the water content was present on the cathode side. Minard et al. [102] also used magnetic resonance imaging to study the propagation of a water front in the PEMFCs.

Optical imaging systems have been around for centuries. They are easy to operate, accessible and cost effective. The maximum resolution is limited by the Rayleigh criterion at about 200 nm. However, the operating region for water management research in the flow fields is limited by the quality of camera being used. Typical PEMFCs are not

manufactured using optically transparent materials and hence, require modifications and inclusion of optically transparent windows. One of the concerns of introducing modification is the effect on the parameter being studied: in this case, the two-phase flow in reactant channels.

Optical imaging has been used to study water management in PEMFCs using in situ studies [43, 46, 78, 84–86, 89, 103–107] as well as ex situ investigations [32, 64, 87, 90, 91, 108, 109]. Tuber et al. [84] first used optical imaging to investigate water transport behavior in PEMFC reactant channels. Hussaini and Wang [104] quantified the liquid water in the cathode channel for the first time in 2009. However, the focus of their work remained spatial quantification: they recorded static images after 30 minutes of operation, assuming steady state condition had been achieved. Nirunsin and Khunatorn [105] used optical imaging to quantify the water in a single serpentine channel PEMFC. They investigated the change in liquid water coverage of the channel area with temperature and stoichiometry. Nishida et al. [110] also used image processing to begin to quantify the size of the water features in the reactant channels.

Sergi and Kandlikar [46] developed a dual visualization setup to simultaneously observe both the anode and cathode gas channels to understand the two-phase flow. They used a frame rate of 60 frames per second for the optical visualization and found they were able to track the motion of slug and film flow features along the length of the channels. They reported the development of an image processing algorithm to quantify the liquid water in the channels. An additional algorithm was also developed to investigate the transition between flow patterns in the channels. However, trends in the data were not discussed. A

new method had been established for using optical imaging with image processing to observe and quantify the two-phase flow in PEMFC gas channels.

Table 1: Comparison of imaging techniques for visualization of PEMFC.

Imaging Technique	**Spatial Resolution** *(μm/pixel)*	**Temporal Resolution** *(fps)*	**Authors**
Neutron Imaging	115	0.5	Kramer et al. [71]
X-ray Radiography	3	0.25	Manke et al. [79]
Optical Imaging	~25	60	Sergi and Kandlikar [46]

Table 1 shows a summary of the comparison of imaging techniques used in the visualization of PEM fuel cells. It is observed that optical imaging is best suited for quantifying liquid water in the reactant channels, in both temporal and spatial domains. With minimal modifications to the cell, the PEMFC can be operated to quantify the liquid water in the reactant channels. Using high resolution and high speed imaging, good temporal and spatial resolutions can be obtained. However, with modifications to the cell for optical imaging, the current densities to which the PEMFC is able to maintain steady operation is reduced. Most optically transparent cells become limited to below 1 A/cm^2. Therefore, quantification studies described above, conducted in situ, do not present data for high current density. Additionally, there is a dearth of data for visualization cells operating at above ambient temperatures (20 - 30°C). This provides a niche research direction where optical visualization and quantification of two-phase flow in the PEMFC reactant channels needs to be undertaken for high current densities and higher

temperatures. Therefore, to test for a large range of current densities, a well-designed ex-situ cell might be more suitable.

The presence of liquid water plays a key role in the performance of the PEMFCs. However, the effect becomes amplified under transient conditions as the cell is more likely to suffer from starvation or flooding as the conditions change. Therefore, the impact of two-phase flow changes on the transient behavior of PEMFCs needs further investigation. The following section delves into the work done in literature dealing with the transient behavior of PEMFCs.

2.4. Transient Behavior of PEMFCs

Automotive transportation powertrains are expected to respond to rapid changes in speed/ acceleration and therefore are designed for a rapid power output response [33,34]. Although significant research efforts have been directed towards understanding the steady state performance of PEMFCs in the past two decades, only a limited number of studies are devoted to the transient response. A brief literature review is presented here with the focus on the transient behavior of PEMFCs. The review further highlights the need to focus research efforts on transients in PEMFCs.

Amphlett et al. [111] highlighted the need for investigating the transient behavior of PEMFCs by combining a steady state electrochemical model with a thermal model. They introduced a heat accumulation term to generate the transient information during start-up, shut-down or step changes in current. The fuel cell voltage was calculated through three terms: the thermodynamic potential, activation potential and the ohmic potential. The

heat accumulation was calculated using the theoretical energy produced by the reaction, the electrical energy output and the heat lost from the stack. This work showed the time dependent change in performance of the cell due to the change in temperature.

Pukrushpan et al. [112] developed a model for the entire automotive fuel cell system based on the transient characteristics of the flow dynamics. Although the model components were verified, the complete model was not validated in their work due to non-availability of transient experimental data. However, their model did not incorporate thermal effects on the cell along with the effect of porous gas distribution layers on the cell. The porous layers impose resistances that have not been considered in this work.

Several experimental studies have highlighted the complexities of transient operation and the need for further investigation of transients with regard to automotive drivetrains [113–119]. The transient behavior of PEMFCs can be categorized into three contributors: electrochemical, thermal and two-phase behaviors. Although the three are very well interlinked in producing the performance of the cell, they have distinct characteristics which need to be isolated and investigated.

The need to understand the transient behavior of fuel cells is increased, as these transient conditions lead to several mechanisms of degradation. The membrane (PEM) suffers more from cyclic loading compared to constant operation, as demonstrated by Liu and Case [120]. At the end of 1000 hours of operation, the MEA subjected to cyclic loading resulted in increased hydrogen cross-over whereas the MEA operated at constant current had a larger mass transport resistance but performed better than the earlier case. Lin et al. [121] also found physical degradation (cracks and pin-hole formation) of the membrane

resulting from operating the cell under dynamic drive cycles. Detailed reviews of the mechanisms for degradation of the catalyst layers are provided by Wu et al. [122] and Schmittinger and Vahidi [123]. With dynamic cycles, occurrence of cell flooding, reactant starvation and local hotspots are increased. Reactant starvation is a primary cause for carbon corrosion and leads to loss in durability of the catalyst [122]. Reactant starvation is likely to introduce cell reversal which promotes carbon corrosion.

Electrochemical Transients

Yan et al. [57] tested for the effect of cathode stoichiometry on the transient performance of PEMFCs. With increasing stoichiometry ratios, the transient response is significantly improved with shorter transients. The authors also observed overshoot / undershoot behavior in the current density, resulting from change in cell voltage. The magnitude of overshoot / undershoot was lower for the case of higher stoichiometric ratios. The effect of temperature was also investigated and showed that at higher stoichiometry and at a higher temperature, the dynamic performance began to suffer. This was attributed to the loss in membrane hydration caused by excess water removal by the high temperature and high stoichiometry combination. The operating pressures also play a role in the transient overshoot / undershoot. As the operating pressure is increased, the magnitude of transient variation and the time to steady state decreases. Zou [124] showed that the transient times are less than 1 second and further decreases with GDL porosity. However, they do not indicate any direct effect of temperature or two-phase flow on the transient times of the electrochemical process.

In 2000, Um et al. [125] used numerical modeling to develop a transient model for PEMFCs. They observed the overshoot in current density when the cell voltage was changed and suggested further investigation. Kim et al. [119] investigated the overshoot and undershoot behavior for various rates of change of voltage with constant reactant flow rates. Meng [115] implemented a transient two-phase non-isothermal model using computational fluid dynamics package FLUENT®. Meng also observed the presence of current overshoot when the cell voltage was changed. The overshoot tendency was more prominent under two-phase condition compared to single-phase condition. This was attributed to the change in liquid water saturation in the GDL which changes the resistance. The time required for the saturation to reach steady state results in the overshoot. However, the time of transience was shown to be on the order of 1 - 2 seconds. An opposite trend (of current undershoot) was observed when the cell voltage was increased resulting in a decrease in the current density.

Temperature Transients

Water management in PEMFCs is not isolated from the thermal management. Kandlikar and Lu [14] highlighted the close relationship between water and thermal management, and the impact of temperature non-uniformity on the change in water transport through-out the PEMFC layers. Tiss et al. [126] introduced a non-isothermal model for the prediction of cell voltage. Yan et al. [127] used numerical modeling to highlight the temperature dependence of PEMFC performance and the impact on water management. They concluded that increasing temperature and current density introduces dehydration on the anode side due to increased electro-osmotic drag. The temperature distribution

also changed sharply at high current densities resulting in damage to the membrane and uneven current and water distributions.

Kim et al. [128] used a 1.2 kW Nexa PEMFC stack from Ballard Power Systems and developed a model based on its results. By applying cyclic current step functions fluctuating between 5 A and 25 A, the output voltage and temperature was observed. Both the output voltage and the stack temperature followed the changes in current load. The temperature profile follows a saw-tooth profile with temperature increasing with increase in load and decreasing when the load is decreased. The voltage showed an overshoot when the current is decreased and undershoot when the current is increased before stabilizing to reach the steady state condition. The authors discussed the temperature profile and modeled the stack temperature. No discussion was provided on the overshoot / undershoot behavior. The temperature takes several minutes to reach a steady state condition which is significantly longer compared to the electrochemical transients as discussed above. Additionally, the results show that due to the time taken by the temperature to reach steady state, the voltage too requires significantly longer duration to reach steady state.

Hwang et al. [129] simulated PEM operation on a CFD software package focusing on the overshoot observed in the current density when the cell voltage is changed from 0.5 V to 0.7 V. They showed that the temperature does not show any overshoot but requires several seconds to reach the steady state value. Additionally, the ionic conductivity decreased with the increase in temperature, which leads to increased cell resistance.

More recently, Rabbani and Rokni [130] used a 21.2 kW stack to investigate the systems level issues of PEMFCs and the transient behavior involved. It was observed that with an increase in current density of operation, the operating temperature would increase immediately due to increase in heat being generated by the cell. It would require several minutes for the temperature to be returned to the steady state value, by increasing the mass flow rate of the coolant. The authors show that the power required for the increased pumping power of the coolant is not large; however the majority of parasitic power is consumed by the air radiator. With a decrease in the operating current density, the temperature drops immediately, creating a large spike in the liquid fraction due to the increased condensation. This could in turn impact the flooding considerations of the cell, and should be avoided.

Tang et al. [118] investigated the impact of changes in electrical load on the temperature of fuel cell stack and reported the absence of any overshoot behavior in the temperature response. They did observe and report on overshoot in the current output during changes in constant voltage mode of operation, and overshoot in the cell voltage when operated under constant current operation.

Two-Phase Transients

Two-phase flow in PEMFCs occurs over a variety of scales. Kandlikar [13] highlighted the need for research investigating the localized presence of liquid water within the fuel cell. Water (in both liquid and gaseous form) in the reactant channels impact the partial pressures, reactant concentration and transport resistance. Liquid water in the GDL

reduces the path available for gaseous transport of reactants thereby increasing the mass transport resistance. Both these cases of water in the GDL and the reactant channels are at micro scale. However, liquid water in the membrane is at nano scale. Two-phase flow in PEMFCs involves investigating water transport inside the membrane, catalyst layer and GDL as well as in the reactant channels.

The transient behavior of two-phase flow within the different components would have a direct impact on the instantaneous performance of the PEMFC. Therefore it is important to obtain a better understanding of the time scales over which these transients affect the performance of the cell.

In 2006, Yan et al. [113] reported the effect of changing stoichiometry to alter the two-phase flow and improve the performance of the cell. Although performance begins to suffer with changing current density at the lower stoic ratios, higher stoics result in higher air flow velocities and therefore a more effective removal of water, leading to improved performance. When the current is cycled, a higher relative humidity shows shorter transients. They also reported that operating at a higher inlet relative humidity at 80°C led to rapid transient response. Operating at the higher inlet RH results in more liquid water throughout the system, but also avoids tendencies of membrane dehydration. At the lower inlet RH, the cell takes significantly longer to reach steady state.

Chang et al. [131] showed that the initial transients are dominated by the electrochemical process, which reaches steady state within the first 1 seconds. Beyond 1 second, the current density begins to fluctuate again and is attributed to the two-phase effects. The authors investigated the effect of porosity of the GDL and the catalyst layer through

parametric analysis. Low porosity of the GDL hinders oxygen transport and increases transient time. There is a distinct change in behavior when the porosity of the catalyst layer is below 0.1, where there is a definite effect of liquid water. Above the value, liquid water does not play a significant role in the performance.

Wu et al. [132] numerically investigated the impact of liquid water on the reactant concentration profiles at the catalyst layer. At startup, no water blockage is assumed with the concentration decreasing with an increase in water generation. However, they established that the concentration profiles reach steady state within the first two seconds under all conditions. Experimental validation of these findings is warranted.

Natarajan and Nguyen [133] modeled the oxygen concentration and the liquid water saturation in the GDL under transient conditions. The oxygen profile reaches a steady state before the 50 seconds mark, whereas the water saturation takes at least 100 seconds. This shows the increasing amount of time required for the two-phase effects to reach steady state after a transient event.

In 2005, Wang and Wang [134] used a commercial software package to investigate the effect of transient behavior in PEMFCs. On changing the inlet humidity levels of the reacting gases, the current density changes over tens of seconds under constant voltage operation. They also showed that the transient behavior changes when the inlet reactant gases are humidified or dry. While a fully humidified set of reactants showed an undershoot behavior when the current density reduced, the dry cathode inlet resulted in undershoot followed by an overshoot. In 2006, the authors [135] conducted parametric

changes to the amplitude of change in current density and inlet relative humidity of the reactant to observe the effect of transient behavior.

In 2007, the same authors [114] numerically investigated the drying phenomenon of the GDL and the membrane under the application of dry gases. They observed that the cell voltage dropped by 100 mV over 20 seconds under the influence of dry gases. The drying of the GDL begins under the channel and is followed by the in-plane drying under the land. The cathode side showed a more prominent transient behavior, highlighting the need for further investigation into cathode transients. They explained this behavior through the lower diffusivity of water on the cathode. However, this behavior can also be explained through the water production replenishing the water removed by dry gases. Although the work by Wang and Wang [114,134,135] showed significant effect of the transient changes on the cell performance, there remained the need of experimental validation of the findings.

Chen et al. [136] investigated the time for the membrane water content to reach a steady state condition. The current density was changed, and the time to return to steady state is calculated. They found the time required to reach steady state decreases at the higher current densities. They attributed it to the higher water generation rates which help in maintaining a high membrane hydration, and thus short transient times.

Song et al. [137] studied the transient dynamics of water transport using numerical simulations. They concluded that the water saturation reaches a steady state in uniformity when the saturation is greater than 0.1. Also, with higher water saturation, reactant transport reaches steady state at a faster rate. Therefore, with larger water content, the

transient stage was reduced. This helped to explain the shorter transients observed by Chen et al. [136] at the higher current densities, when there is larger water saturation in the porous layers.

The majority of the research reported in literature has been focused towards the investigation of two-phase transients done in the numerical domain. There is a dearth for the experimental validation and further work into the saturation of the porous materials which impact the two-phase transients in the PEMFCs. The two-phase transients in the reactant channels have not been addressed hitherto and need to be investigated in detail.

2.5. Summary of Literature Review

Above presented is a review of the literature referred for this work. It has been segregated by the different focus areas which are addressed. Based on the reviewed literature, a summary is now presented to bring forth the niche openings that need to be investigated further. This will form the basis of the current work.

i. Extensive work has been done in characterizing the different parameters which affect the performance of a PEMFC. Temperature, inlet RH, stoichiometric ratio of operation and the operating pressure are all important factors in obtaining a good performance from the PEMFCs. Water management also plays a key role in improving the performance.

ii. Pressure drop has been shown to be a key diagnostic tool in detecting liquid water in the cell. However, no work has shown the direct relationship between

two-phase pressure drop multipliers (used to quantify liquid water in reactant channels) and the performance of the cell.

iii. Significant experimental work has been done to investigate the two-phase pressure drop in the reactant channels. Many modeling studies have investigated the two-phase pressure drop in the microscale channels, though the conditions in the PEMFC reactant channels are considerably different. More data on the quantity of liquid water present in the channels would be helpful in future modeling efforts.

iv. A variety of imaging techniques have been used in the investigation of water management in PEMFCs. Neutron imaging, X-ray radiography, MRI and optical imaging have been used successfully for fulfilling different objectives. An optical imaging system is selected for this work because of the high spatial and temporal resolution and the ease of operation. Previous works have shown the feasibility of using optical imaging systems to observe and investigate the two-phase flow in PEMFC reactant channels.

v. A common problem encountered in using an optically clear fuel cell is mass transport driven cell performance loss at low current densities. Current densities above 1.0 A/cm^2 have not been tested in the in situ visualization studies due to this problem. However, state of the art fuel cells are able to achieve much higher current densities (~3.0 A/cm^2) and therefore an ex-situ study is necessary to complement and provide the quantification data for liquid water presence in the channels.

vi. Transient behavior of PEMFCs has not received the same focus as the steady state operation. The transient behavior can broadly be classified into three categories: electrochemical transients, temperature transients and two-phase transients. Electrochemical transients have been investigated and showed a very small transient time.

vii. Thermal and two-phase transients have received less focus. These two types of transients operate over longer time frames and can play a key role in the overall transient performance. Overshoot exists in both the current and voltage response. There is no overshoot observation in the temperature profile. However, the two-phase flow behavior has not been investigated for the presence of transients.

viii. Two-phase transients have been investigated inside the GDL and the change in saturation levels as a function of time have been reported. The transient behavior of two-phase flow in the reactant channels have received no attention.

2.6. Objectives of the Present Work

The review of literature provided above highlight the gaps that exist in our understanding of liquid water transport in the reactant channels of PEMFCs. The objective of this work is to enhance this knowledge and the following objectives are identified in an attempt to improve our understanding.

i. A direct quantitative relationship needs to be developed between the liquid water present in the reactant channels and the performance of the cell.

ii. The liquid water present in the reactant channels needs to be quantified for different PEMFC operating conditions, providing a better understanding of the behavior.

iii. The dominant flow patterns need to be identified for the full range of PEMFC operating conditions.

iv. Transient operation of PEMFCs needs to be investigated with a special focus on the temperature and two-phase transient behavior.

v. The two-phase transient behavior needs to be characterized through experimental data.

3. In situ Water Management Investigation

Water management in PEMFCs is considered to be one of the major roadblocks in their application to automotive platforms. Both excess water and a lack of adequate water in the system lead to loss in performance and durability [39,40]. Water management is important at the different component layers of the PEMFC system, i.e. at the membrane, catalyst layer, MPL, GDL and the reactant channels [14]. This section examines the relationship between the liquid water in the reactant channels and the performance of the fuel cell. The findings from this work have been submitted to the International Journal of Hydrogen Energy and are currently under review.

3.1. Objectives of Water Management Investigation

Several studies have explored the relationship between operating conditions and water management, as discussed in the review of studies present in literature (Section 2.1). However, no focus has been given to the impact of liquid water in the reactant channels on the cell performance. Changing operating conditions are modes of changing the saturation conditions within the reactant channels and thereby controlling the quantity of liquid water in the channels.

The liquid water is characterized using the two-phase pressure drop multipliers, while the cell voltage is indicative of the cell performance. The quantity of liquid water present in the reactant channels is manipulated by changing the operating temperature and the inlet RH of the reactant gases. Changing these two parameters results in a change in the saturation pressure of water within the channels and therefore affects the quantity of

liquid water in the channels. The impact of liquid water in the channels on the cell performance is investigated.

The saturation pressure of water in air increases exponentially with increase in temperature. The values for the range of fuel cell operating conditions (20 – 80°C) are shown in Figure 11. This can also be seen using the expression shown in equation 6, where P_{sat} is in Pascals and temperature is measured in °C. Thus, with increase in temperature, the amount of water that can be carried in the vapor phase increases significantly. Using a stoichiometric ratio of 2, commonly used on the cathode side, an order of magnitude change in the percentage of water being removed in the vapor phase is observed as the temperature is increased from 40 to 80°C, as seen in Table 2. Whereas at 80°C with dry inlet gases 88% of the generated water can be removed in the vapor phase, only 7.84% can be removed at 40°C. Both percentages decrease with increase in the inlet RH of the reactants, resulting in less water being removed in the vapor phase.

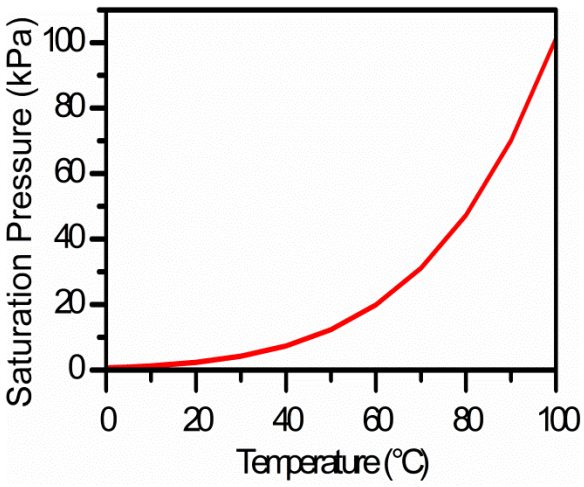

Figure 11: Saturation pressure of water in air as a function of temperature.

$$P_{sat}(T) = -2846.4 + 411.24T - 10.554T^2 + 0.16636T^3 \quad (6)$$

Therefore, as the temperature and inlet RH conditions change, there is a drastic change in the quantity of liquid water in the reactant channels. A deeper understanding of the effect of this liquid water presence on the cell voltage and cell performance is warranted. The cell performance is evaluated by comparing the cell voltage at a constant current load on the cell. This means the power generated can be compared directly with relation to the different operating conditions. The cell performance is directly correlated to the liquid water in the reactant channels.

Table 2: Percentage of water generated being removed in the vapor phase at a constant stoichiometry of 2, with different temperatures and levels of inlet relative humidity on the cathode side.

Temperature (°C)	Inlet Relative Humidity (%)	Percentage of Water Generated being Removed in Vapor Phase (%)
40	0	7.84
40	50	4.07
40	95	0.42
60	0	24.24
60	50	13.43
60	95	1.49
80	0	88.89
80	50	58.12
80	95	8.04

3.2. Experimental Setup for Performance Prediction

Towards meeting the objective of obtaining a relationship between liquid water present in the reactant channels and the cell performance, an in situ setup was used. The PEM fuel cell had an active area of 50 cm^2 and catalyst loading of 0.1 and 0.3 mg/cm^2 were used on the anode and cathode sides, respectively. The membrane used is sourced from Gore Associates and is 18 µm thick. MRC 105 with 5% PTFE loading was used as both the anode and cathode GDL, with a proprietary MPL coated by General Motors (GM). The GDL has a thickness of 230 µm while the MPL is 30 µm; resulting in a combined thickness of 270 µm.

The current collector was gold plated copper for reduced contact resistance and high corrosion resistance. Parallel channel configuration was used for the reactant channels, which were housed in the current collector plate. The flow field design and development has been discussed in detail by Owejan et al. [40]. The parallel channel 50 cm^2 single cell design represents a segment of the flow field geometry of fuel cell hardware being utilized in the automotive drivetrain and meeting the performance targets of the US-Department of Energy, as shown in **Figure 12**. The reactant channels were 400 µm deep, 700 µm wide and 183 mm long with 11° of switchback. On the cathode side, the land widths are 500 µm wide while on the anode the width is increased to 1500 µm. In order to maintain an active area of 50 cm^2, the width of the active area is just 27.3 mm. This results in a rectangular flow field design, housing 22 parallel channels on the cathode side and 11 on the anode side. The channel and land dimensions have been optimized based on experimental and numerical results available in literature. The depth of the channel had been decided with considerations for the repeating distance of bipolar plates in the

stack, in keeping with the US-DOE target for volumetric power density of 2 kW/L. In our single cell unit, a unipolar plate is used. However, for the equivalent stack, the repeating unit would be just 2 mm per cell.

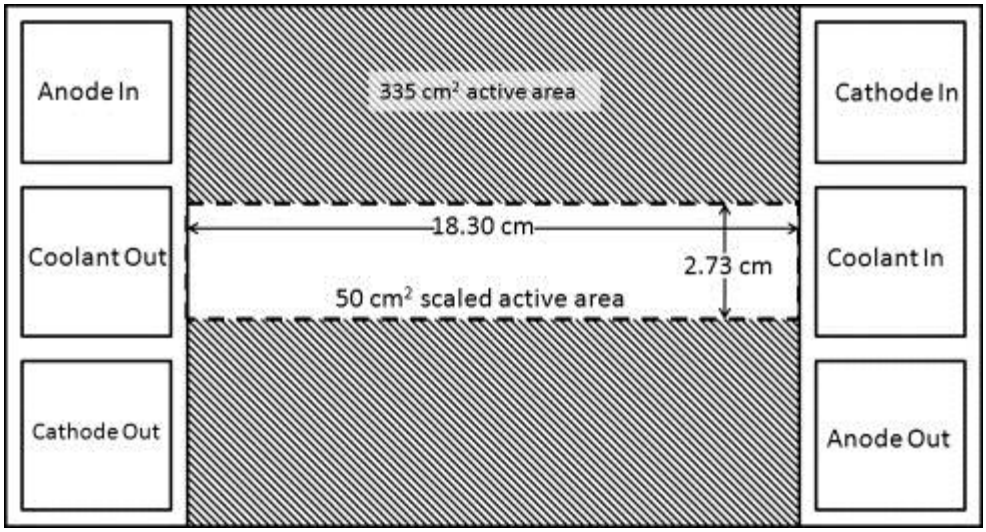

Figure 12: Scaling active area for single cell geometry – 50 cm^2.

Pressure taps were included into the inlet and exit manifold design to measure the channel pressure drop along the length of the channel [32,88]. The compression plates were fabricated in aluminum to minimize thermal gradients. The compression plates also housed the coolant channels, which were serpentine and were divided into four segments for a uniform temperature control. Water was used as the coolant in the compression plates.

The fuel cell test facility was built around a G40 fuel cell test stand by Greenlight Innovation. The test stand was supplied with bottled hydrogen and air from a 'dry air generator'. The test stand was responsible for supplying the PEMFC with reactants,

maintaining the reactant inlet temperatures and the respective dew point temperatures. A Siemens' de-ionized (DI) water system was connected to the G40 test stand, to provide the pure water for the adequate humidification of the reactants. The gas temperatures and the dew point temperatures are set at the test stand to monitor the gas temperature and the relative humidity is controlled through the dew point temperatures. Additional heated gas lines connect the test stand fuel lines to the PEMFC inlet ports to avoid condensation within the supply lines. Temperature of the coolant being circulated through the compression plates of the PEMFC was controlled by a temperature controlled water bath with a heating and cooling capacity of 0.5 kW. Additionally, eight 0.8 kW heaters were placed in-line with the PEMFC coolant line inlets to provide rapid heating of the cell. The coolant channels were divided into four segments on each of the cathode and anode side, with a total of eight segments, to avoid any temperature gradients. The in-line heaters mentioned above line up with each segment to provide direct temperature control for each segment. Figure 13 shows the schematic of the test setup.

The voltage, current, dew point temperatures and gas temperatures were measured at the test stand (Greenlight G40), using the Hyware II custom software by Greenlight Innnovation. The test stand recorded the data at 1 Hz. The cell voltage was measured to an accuracy of 0.5% while the current was measured to 0.25%. Cell temperature and pressure drop data was recorded using a PXIE chassis from National Instruments with a custom in-house developed LabVIEW VI. The temperature data was recorded at 1 Hz to an accuracy of ±1°C, and the pressure drop was recorded at 100 Hz with an accuracy of 0.25% over the full scale. This results in an uncertainty of ±0.08 kPa in pressure drop readings.

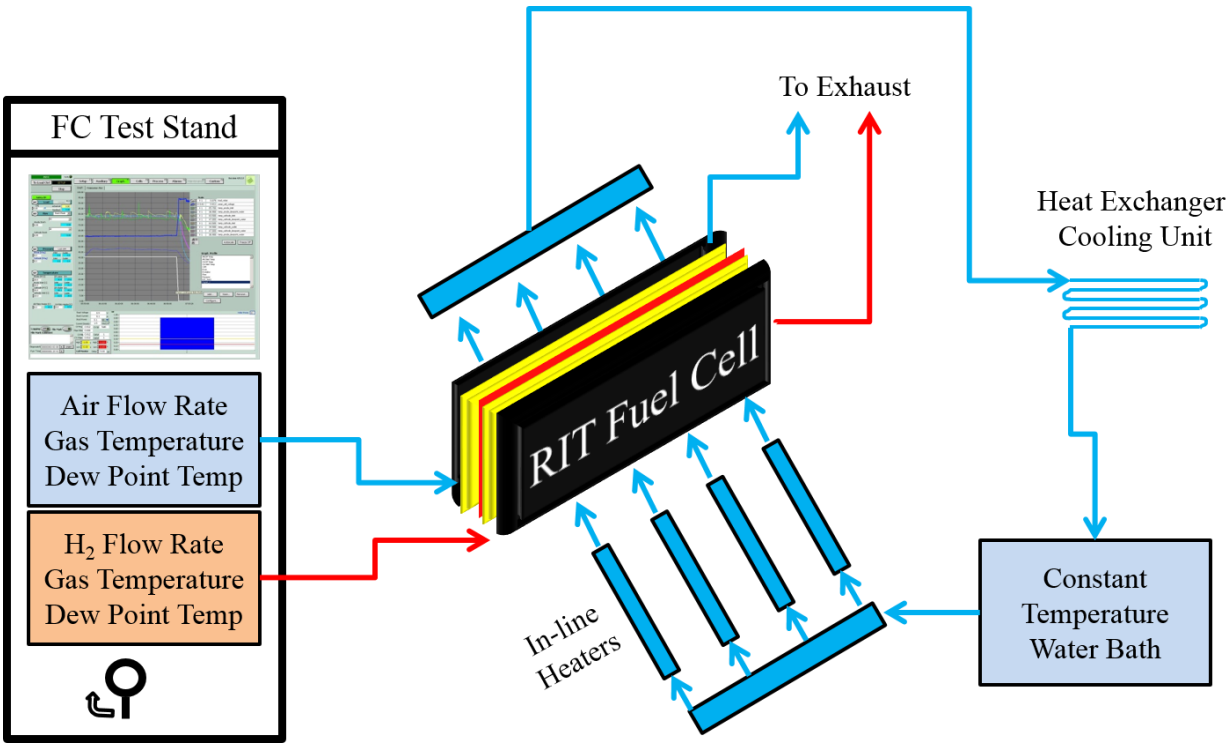

Figure 13: Schematic of the in situ test setup. A Greenlight G-40 test stand controls the reactant conditions, while external controls are setup for controlling cell temperature.

Ten thermocouples record the cell temperature at the compression plates (five on anode side and five on cathode side). Additionally, two thermocouples measure the temperature of the incoming reactant gases and eight thermocouples are dedicated to measure the temperature of the coolant before it is introduced into cell coolant channels. Four thermocouples are used in the control loop to monitor the temperature of the inlet gas lines to prevent condensation of the water vapor in the humidified gases or overheating of the gases. Temperature controllers from WATLOW® are used to implement PID control of the temperature of the reactant gases being supplied to the PEMFC.

Conditioning and Cell Preparation:

After assembly, the PEMFC was conditioned by operating through a six hour cycle. This involved increasing the operating current density to reduce the cell voltage to 0.6 V where it was maintained for 60 minutes. This was followed by a current cycling resulting in alternating low and high operating voltage. At the start of each set of tests, a shorter conditioning cycle was run, which involved 30 minutes of operation at constant voltage of 0.6 V followed by current cycling as described. The conditioning was conducted to bring the cell to adequate hydration and improve the repeatability and reproducibility of the results [138].

For each of the tests, the conditions were set and the cell was allowed to stabilize for 60 minutes. Data was recorded at steady state for 15 minutes which was then averaged to obtain the data points shown as part of these tests. A total of 50 tests have been conducted to study the water management and the corresponding performance of the cell as a function of changing temperature and inlet RH conditions. Additional single-phase tests have been conducted, at no load condition for comparison cases.

Test Conditions:

The test conditions for this investigation were chosen to change the saturation conditions within the fuel cell reactant channels, keeping within the bounds of automotive PEMFC operating conditions. The conditions were obtained from www.pemfcdata.org under the aegis of the US-DOE project described in section 1.6. The cell temperature was changed

between 30 – 80°C, while the reactant inlet humidity was maintained between 0 – 95%. The reactant stoichiometry was kept constant at 1.5 for anode and 2.0 for the cathode inlet.

The cell was operated at temperatures of 30 to 60°C to compare the effect of temperature on the cell performance. The tests were also performed at 70 and 80°C (under dry conditions). However, stable operation could not be obtained as the membrane began to dry out. Large fluctuations in the cell voltage and a significant drop in performance were observed, and a steady state could not be maintained for the 60 minutes and therefore no results are reported for those temperatures. Table 3 shows the operating conditions used for investigating the effect of temperature. The performance and two-phase multipliers are compared for cases with current density of 0.4, 0.6 and 0.8 A/cm^2. To investigate the effect of cathode inlet relative humidity, the cell was operated between 40 and 80°C with different inlet relative humidity. The operating conditions used for investigating the effect of inlet relative humidity on cell performance are also seen in Table 3. The same dew point temperature is set for both anode and cathode sides and the gas temperatures are maintained at the same level. Therefore, the inlet RH on both the anode and cathode sides is maintained accordingly. The table below shows the target values for the inlet RH, while the results are reported with the relative humidity value recorded at the test stand. The reported inlet RH is for the cathode side.

Table 3: Operating conditions for investigating the effect of temperature and inlet relative humidity on the cell performance and liquid water content in the channels.

Temperature (°C)	Cathode Inlet RH (%)	Current Density (A/cm^2)	Investigated Parameter
30, 40, 50, 60	0	0.4, 0.6, 0.8	Temperature
40, 50, 55	0, 50, 95	0.8	Inlet RH
60, 70, 80	0, 50, 95	0.8	Inlet RH

Before commencing with the above mentioned tests for the current investigation, a polarization curve was obtained by operating the cell at 60°C with both the gas streams humidified to 95% RH at the inlet of the flow fields. Figure 14 shows the polarization curve. No changes were made to the cell between obtaining the cell polarization curve and operating it for the investigated conditions, discussed in Table 3. As described above, the investigation focuses on the cell operating between 0.4 and 0.8 A/cm^2. It can be observed from the figure, that the cell remains within the region dominated by ohmic losses for the tested conditions. It is important to remain within the ohmic losses region as this section is linear. The region of high current densities is dominated by mass transport loss dominated cell potential. This region is inherently non-linear, making the analysis of results more complicated.

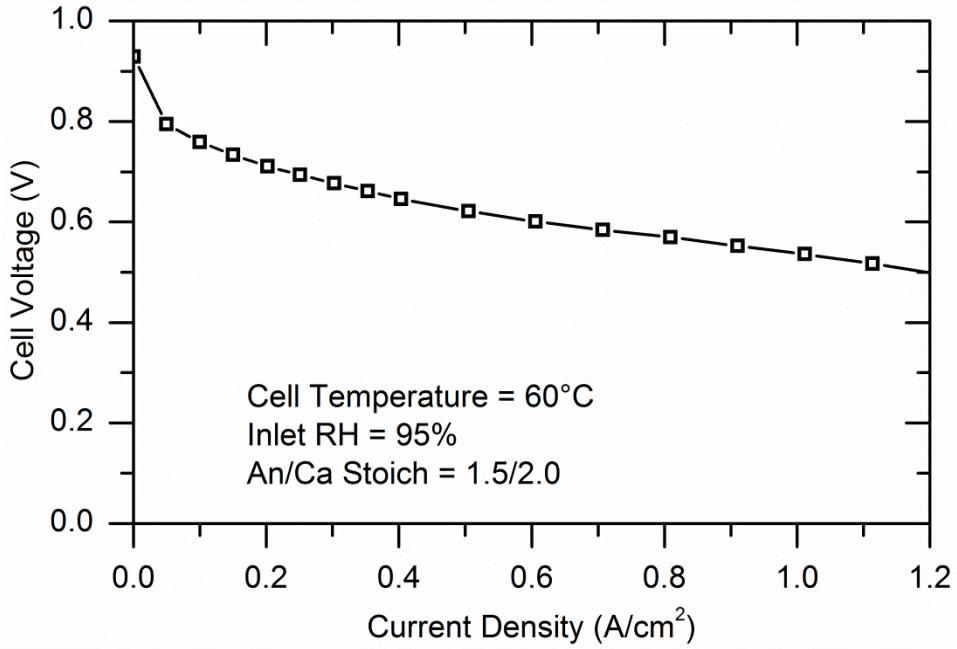

Figure 14: Polarization curve for validating performance of PEM fuel cell. Operated at 60°C with 95% inlet RH. Stable operation up to 1.2 A/cm^2 without mass transport limitation.

3.3. Results

The experiments are first conducted for single-phase flow in the channels in the absence of any reaction to obtain the single-phase flow characteristics of the cathode gas channels. These are followed by actual fuel cell testing under different operating conditions. Two-phase flow results are plotted as a function of the two-phase flow multiplier and the associate performance of the fuel cell.

Single-phase pressure drop trends

Single phase pressure drop tests were conducted with dry air flow in the gas channels without any reaction. In laminar flow, the single phase pressure drop increases linearly

with increase in flow rate. Single phase pressure drop also increases with increase in temperature. This behavior is expected since the flow in the channels is laminar, and the entrance effects are not significant in relation to the total channel pressure drop. This behavior is confirmed with the experiments as seen in Figure 15. The pressure drop is plotted as a function of cathode air flow rate with air temperature as a parameter. With increase in temperature, the density of the gases reduces, therefore the velocity increases resulting in a higher pressure drop along the same length of channel.

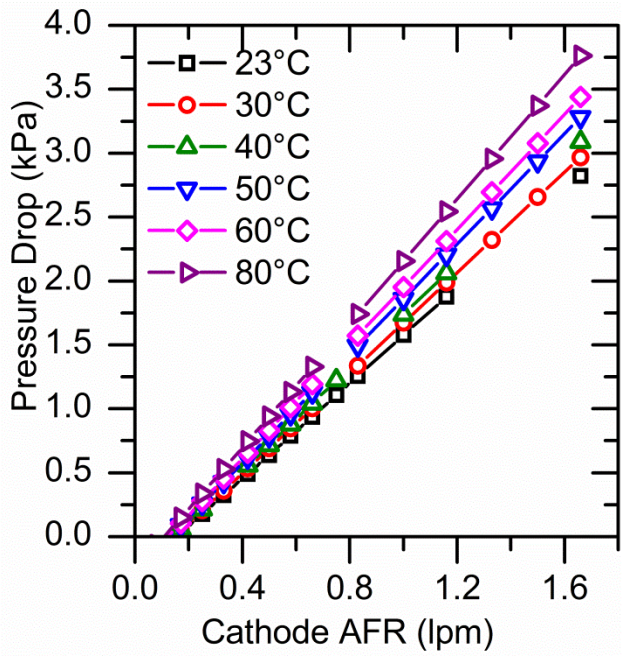

Figure 15: Single-phase pressure drop as a function of air flow rate (current density with cathode stoichiometric ratio of 2) and temperature.

Single-phase pressure drop can be predicted analytically with ease. Equations 4 and 5 show the analytical expression used to predict the pressure drop as a function of the gas velocity. Equation 5 shows the parameters which depend on the temperature, resulting in

the change in pressure drop with temperature. Of the factors shown, viscosity is a function of temperature of the system. The velocity u, is based on the density of the gases and therefore varies as a function of temperature.

The highest air flow rates shown in Figure 15 are used to calculate the change in pressure drop with temperature, as they show the largest changes in pressure drop and account for the smallest errors. The change in results from 23 to 80°C at the highest air flow rate come is 33%.

$$\frac{\Delta P_{80}}{\Delta P_{23}} = \frac{3.76}{2.82} = 1.33 \approx 33\%$$

The air flow reported in liters per minute (lpm) is the direction conversion of the mass consumption at room temperature and pressure. The gases are heated after they are metered, in order to maintain constant mass flow rates. The pressure drop is a function of both viscosity and density of air, both of which are functions of temperature. The change in temperature from 23 to 80°C results in an increase in the viscosity by 15% and a decrease in density by 16%, which combine to form an increase in pressure drop of 31%. Experimental uncertainty in the air flow rates, rounding errors and the error in the pressure sensors account for this remaining difference between the experimental results and the theoretical change expected.

Two-phase pressure drop trends

Two-phase pressure drop is measured during the operation of the PEMFC. It involves the flow of air through the cathode flow field and interaction with the water being generated

in the cell. Additional liquid water can also be formed due to condensation of the humidified gas streams resulting from fluctuations in the cell temperature and loss of reactant gas volume due to condensation [28,37]. Figure 16 shows the two-phase pressure drop as a function of the air flow rate at the four different temperatures for dry inlet air and fully humidified (95% RH) inlet air. The two-phase pressure drop also increases with increase in air flow rate. However, the increase in two-phase pressure drop is not linear with increase in flow rate. This was shown for the lower current densities by See [37] and can also be observed here. With dry inlet gases (Figure 16a), there is a larger variation in the pressure drop as a function of temperature. However, with fully humidified gases, the deviation in two-phase pressure drop with temperature is much less. Due to this non-linear change of two-phase pressure drop with increasing gas flow rates and increasing temperature, pressure drop for changing fuel cell conditions is best described using two-phase multipliers.

The two-phase multiplier is defined as the ratio of two-phase pressure drop to the single-phase pressure drop at the same gas flow rate and is given in equation 3. The two-phase multiplier is a direct parameter to represent the influence of the liquid water on the two-phase pressure drop. An increase in the liquid water in the stream directly increases the two-phase multiplier whereas a decrease in the liquid water results in a decrease in the two-phase multiplier. Therefore, this can be used as a direct quantifying tool for the quantity of liquid water in the reactant channels.

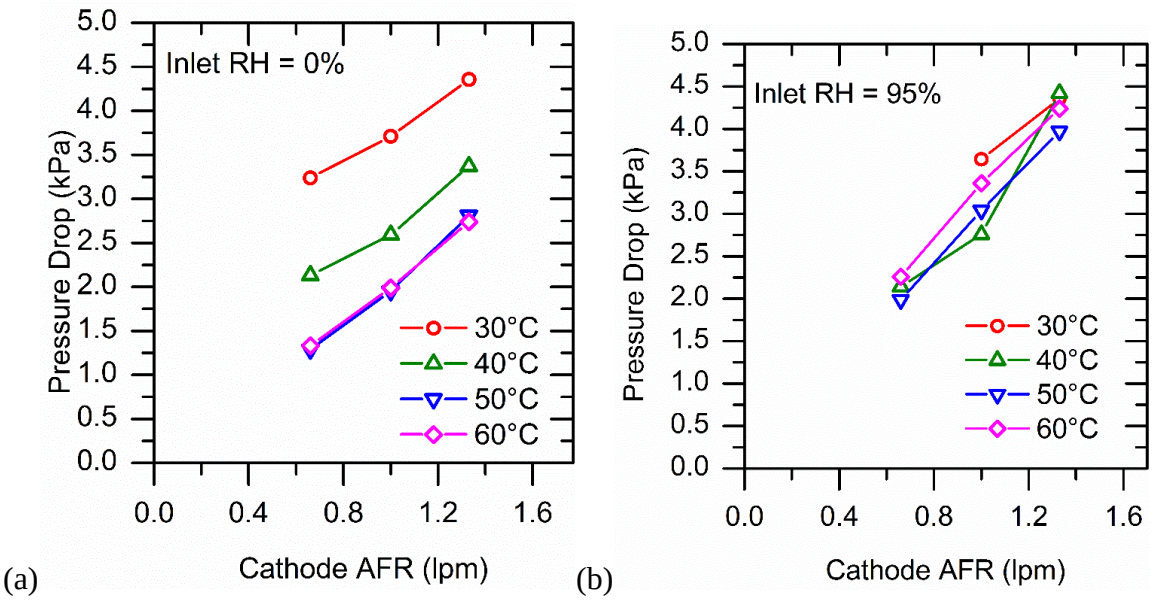

Figure 16: Two-phase pressure drop as a function of air flow rate (current density with cathode stoichiometric ratio of 2) and temperature. Operated with (a) dry inlet gases and (b) with inlet RH of 95%.

Effect of increasing current density

Figure 17a shows the two-phase pressure drop multiplier and cell voltage as a function of increasing current densities from 0.4 A/cm^2 to 0.8 A/cm^2 with temperature increased from 30 to 60°C and dry inlet gases (i.e. inlet RH of 0%). It is noted that the two-phase multiplier decreases with increasing current density. This has been shown in prior works [32,37,94] and indicates lower impact of liquid water on the pressure drop. The increasing air flow velocities associated with increased current density removes the liquid water being generated more effectively, and reduces the two-phase multiplier. The increase in gas flow velocity results in a change in the flow regime from slug flow regime to film flow and subsequently to mist flow regime. The decrease in two-phase multipliers is much more prominent at the lower temperatures as there is more liquid water present in the reactant channels and flow regimes play an important role on the two-phase

multipliers. With increasing temperature, it can be observed that the two-phase multipliers remain low, near a value of 1. There is little liquid water to create an impact on the two-phase pressure drop. Thus, we may conclude that with increase in temperature most of the water is being removed in the vapor phase or in the form of mist, resulting in the quantity of liquid water in the channels being insignificant. This can be observed for both temperatures of 50 and 60°C.

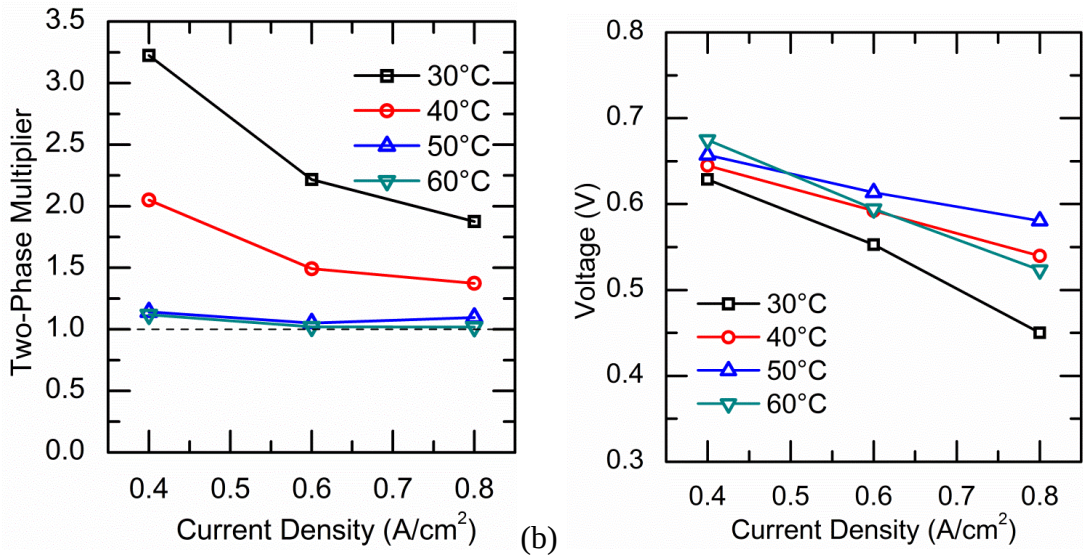

Figure 17: Cathode channel two-phase multipliers (fig. a) and voltage (fig. b) as a function of increasing current densities for the temperatures of 30 to 60°C, with dry inlet gases.

Figure 17b shows the cell voltage as a function of increasing current density. This can be expected from the standard polarization curve and is attributed to the increase in resistive loss in potential due to the increasing current density. With more current flowing through the circuit, the same resistance results in higher potential loss. As the current densities being reported are in the central segment of cell operation (Figure 14), it can be assumed

that the operation is dominated by the ohmic resistance, which is linear with regard to increasing current density. The trends in the figure also reflect a linear relationship between the current density and cell voltage. However, with increasing temperature, it can be observed that the slope of the linear relationship becomes less steep. A lower gradient indicates a lower resistance of the cell. The resistance reported includes electronic resistance in the system, protonic resistance in the membrane as well as mass transport resistance in the porous layers. This lower resistance can be attributed to the decrease in liquid water in the reactant channels (and in the other components / layers) of the cell. However, with dry inlet gases, as the cell temperature reaches 60°C, the voltage decreases and the cell resistance increases. This is observed from the slope of the voltage plot in Figure 17b. The increased cell resistance can be attributed to the decrease in membrane hydration due to the increase in temperature. The dry gases reduce the water content in the cell leading to reduced membrane hydration. The reduced hydration results in higher proton resistance and thus higher overall cell resistance.

Effect of temperature

Figure 18 shows the cell voltage and the two-phase pressure drop multiplier as a function of temperature. The lower half of the plot shows the cell voltage as a function of temperature, whereas the upper half of the plot shows the two-phase multiplier for the same conditions. Temperature is varied from 30 to 60°C with an inlet relative humidity of 0% (dry inlet gases). The results are shown for a single operating condition of 0.6 A/cm^2 at the different temperatures. It can be observed that the cell voltage increases with temperature. However, at 60°C there is a decrease observed in the voltage.

Simultaneously, the two-phase multiplier decreases to reach a value of 1.05 at 50°C and then stabilizes with further increase in temperature.

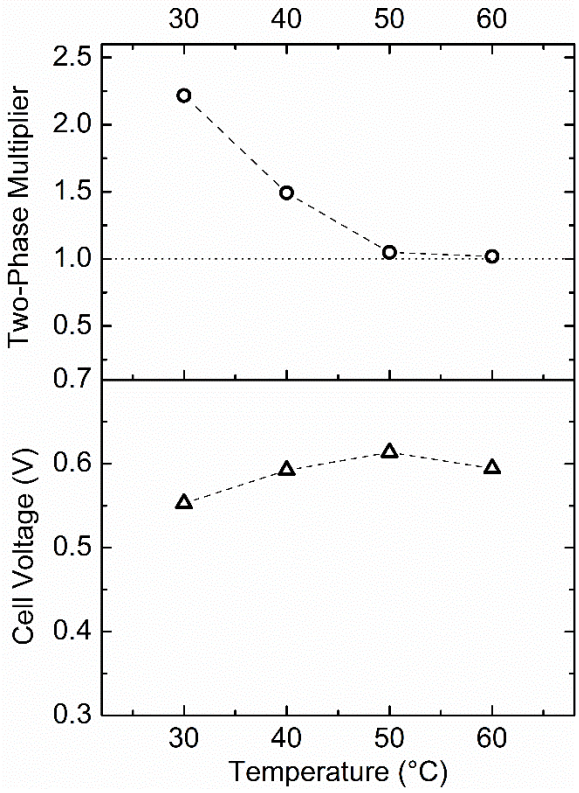

Figure 18: Cell voltage and two-phase pressure drop multiplier as a function of increasing temperature (30 - 60°C) for a current density of 0.6 A/cm^2 operated with 0% inlet RH.

At the lower temperatures, the high two-phase multiplier indicates a large presence of liquid water in the reactant channels. This corresponds to a low cell voltage. The cell voltage improves with decrease in the two-phase pressure drop multiplier. This indicates an improvement in performance with decrease in liquid water in the channels. At the influx point of 50°C, the two-phase multiplier is close to 1, indicating negligible presence of liquid water with the peak cell voltage obtained. As the temperature is further

increased to 60°C, the two-phase multiplier remains constant suggesting no change in liquid water content in the reactant channels. At the same temperature, the cell voltage shows a decrease. This decrease can be attributed to the decrease in membrane hydration, thus increasing the cell resistance and decreasing the cell voltage. This can be verified in the plot for 60°C in Figure 17. Figure 19 shows the same trend for a current density of 0.8 A/cm^2 at the same operating conditions. The drop in cell voltage at 60°C is more pronounced at the higher operating current density. This larger drop at 60°C can be attributed to the higher gas flow rates which are associated with a higher current density, leading to more water being removed from the membrane, and a higher membrane resistance.

As discussed earlier, the resistance of the cell changes with change in temperature. The cell resistance is dominated by the resistance of the membrane and the liquid water in the reactant channels, as there is no change in the electrical resistance of the porous layers. Figure 20 shows the cell resistance as a function of temperature. The cell resistance is calculated from the cell voltage obtained at different current densities, using values from Figure 17b being used in equation 7. We observe that the cell resistance decreases with increasing temperature. This can be attributed to the decrease in liquid water content with rising temperature. However, as the temperature reaches 60°C, the cell resistance increases. This can be attributed to an increase in the membrane resistance, as there is insignificant water in the reactant channels. The dry-out causes the ionic resistance of the membrane to increase significantly resulting in this increased resistance of the cell.

$$\mathbf{R} = \frac{\mathbf{\Delta V}}{\mathbf{\Delta I}} \tag{7}$$

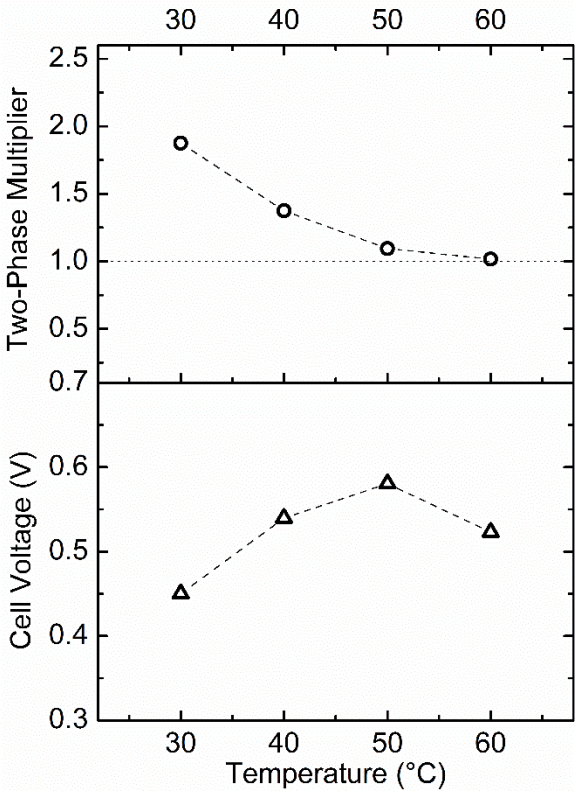

Figure 19: Cell voltage and two-phase pressure drop multiplier as a function of increasing temperature (30 - 60°C) for a current density of 0.8 A/cm^2 operated with 0% inlet RH.

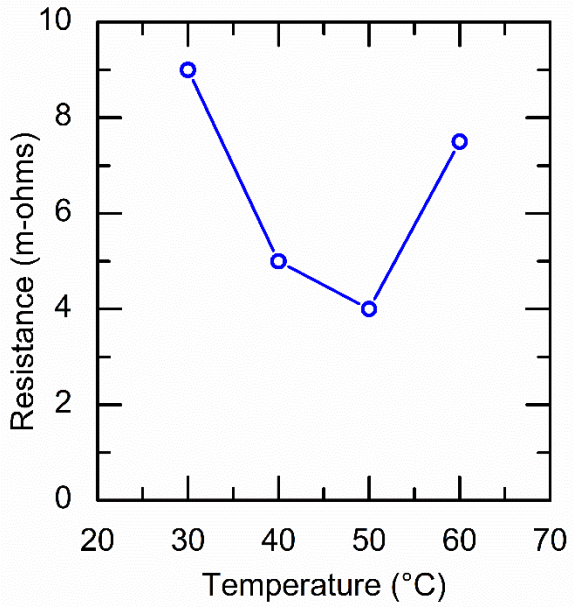

Figure 20: Cell resistance as a function of increasing temperature (30 - 60°C) when operated with dry inlet gases.

Cell voltage predictions

Didierjean et al. [139] proposed an equation, shown in equation 8, to predict the cell voltage at different temperatures. The equation shows the thermodynamic cell voltage at the different operating conditions considering water to be generated in the liquid phase.

$$E_{th}(T,P) = E_{th}(T^0,P^0) - 8.5\,x\,10^{-4}(T - T^0) + \frac{RT}{2F}\ln(a_{H_2}a_{O_2}{}^{\frac{1}{2}}) \quad (8)$$

The first term, E_{th} is the baseline voltage at the baseline temperature, which has been selected to be 50°C for our investigation. T^0 is the baseline temperature, which in this case is in Kelvin and is taken to be 323 K (50°C). T is the temperature of the condition being predicted, which varies from 30 to 60°C. R is the universal gas constant, with a value of 8.314, F is Faraday's constant (F = 96485). a_{H2} is the activity of hydrogen, which

is unity and a_{O2} is the activity of oxygen, which is equal to the mass fraction of oxygen in air with a value of 0.21.

From Figure 18 and 19, we note that the cell voltage reaches maximum at a temperature of 50°C. Therefore, the reference temperature T^0 is taken at 50°C (323 K). The cell voltages for the other temperatures are predicted based on this reference temperature. Figure 21 shows the comparison of experimental and predicted cell voltages. Figure 21(a) shows both the experimental and predicted cell voltages for a current density of 0.6 A/cm^2 while Figure 21(b) shows the voltage values for 0.8 A/cm^2. It can be observed that at the lower temperature, there is significant difference between the two voltages. This may be attributed to the liquid water in the cell, as seen by the two-phase multipliers in Figure 18 and 19. The increased presence of liquid water causes the loss in cell performance. The voltage lost due to this poor water management can be seen in Figure 22. With increase in temperature, the voltage loss decreases. As the temperature is increased to 60°C, there is a slight increase in this lost voltage. This can be attributed to the loss in membrane hydration, leading to an increased membrane resistance and thus a loss in cell voltage. This reinforces the finding from Figure 17 and 20. The effects of cell flooding at the lower temperatures and membrane dehydration at the higher temperatures are seen at both current densities, though the magnitude of the effects is larger for the higher current density of 0.8 A/cm^2. This shows why mass transport losses become more pronounced at the higher current densities when adequate water management strategies are not utilized.

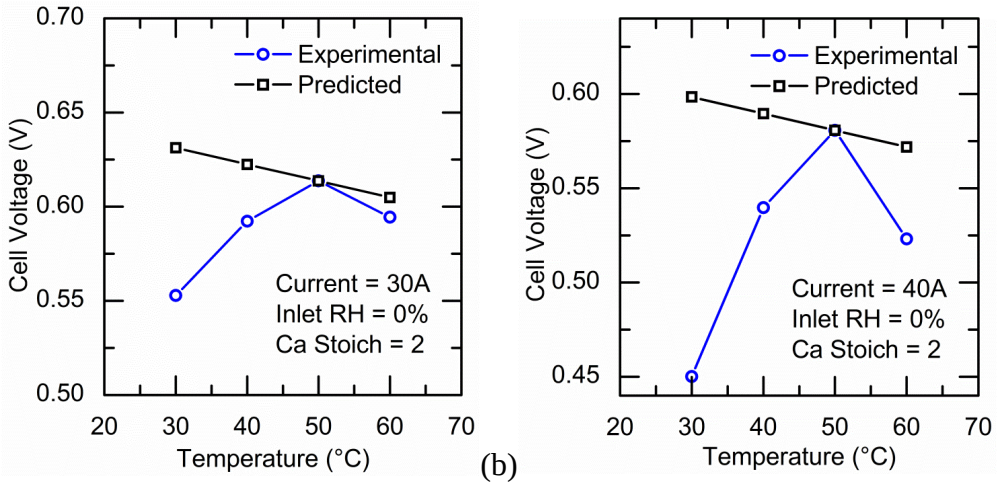

Figure 21: Comparison of experimental and predicted cell voltage for changing temperature conditions for (a) 0.6 A/cm^2 and (b) 0.8 A/cm^2. T^0 is considered at 50°C. All other parameters remain constant.

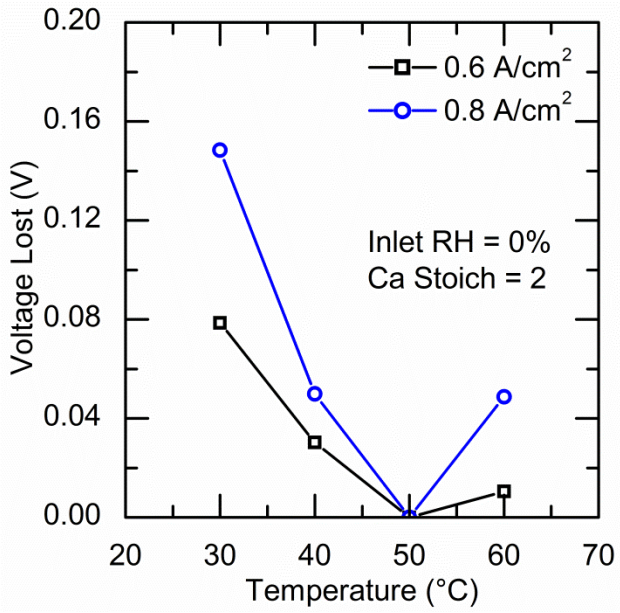

Figure 22: Difference between experimental and predicted cell voltage, attributed to voltage lost to poor water management.

Effect of inlet relative humidity

Figure 23 and 24 show the effect of cathode inlet relative humidity on the cell performance at temperatures of 40 and 50°C, respectively. The cell is maintained at a constant temperature and the dew point temperature is changed in order to obtain different inlet relative humidities. The lower half of the plots show cell voltage as a function of increasing inlet relative humidity, whereas the upper half of the plot shows the two-phase multiplier obtained. The data is presented as a function of the inlet RH as calculated by the test stand based on the gas temperature and the dew point temperature.

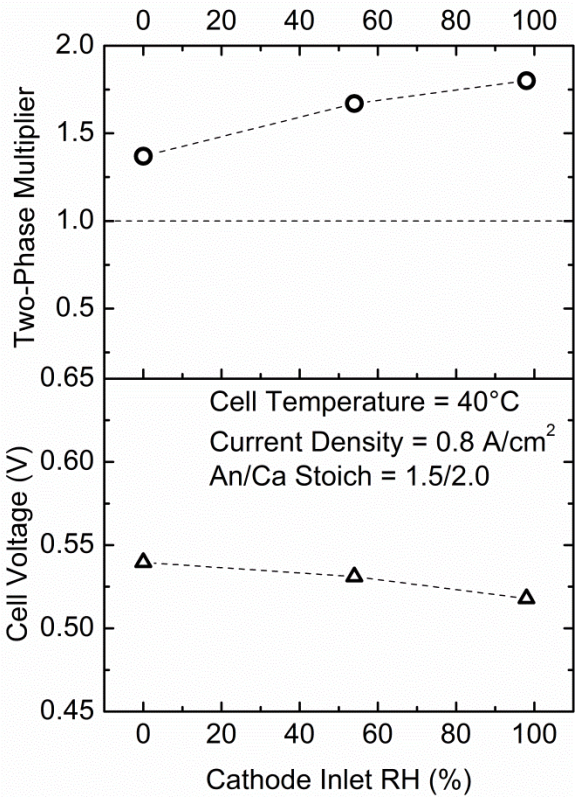

Figure 23: Effect of RH on cell performance and the two-phase multiplier, at a cell temperature of 40°C.

With increasing inlet RH, the performance decreases. Simultaneously, the two-phase multiplier increases with an increase in the inlet RH. The increase in the two-phase multiplier indicates increased presence of liquid water in the channels. As the inlet RH increases, the ability of the gas stream to remove water in the vapor phase decreases, thereby increasing the two-phase multiplier. The increased quantity of liquid water in the reactant channels, increase the reactant transport resistance, leading to a lower performance from the cell. This is observed due to the lower cell voltage. Thererfore, with increase in cathode inlet RH, the two-phase multiplier increases and the cell performance decreases.

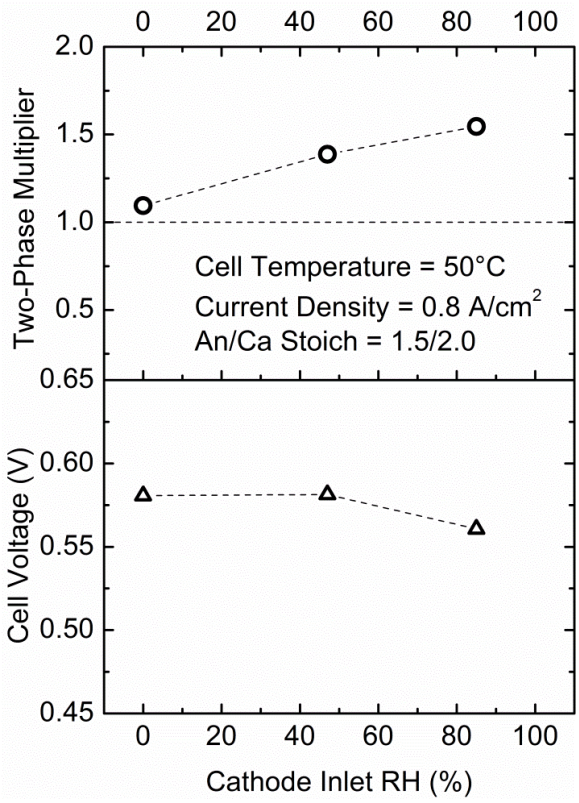

Figure 24: Effect of RH on cell performance and the two-phase multiplier at a cell temperature of 50°C.

Figure 25 and 26 show the effect of cathode inlet relative humidity on the cell performance at temperatures of 60, 70 and 80°C. A reversal of cell performance trend is observed at these temperatures. The cell performance improves with an increase in the inlet RH of the reactants. The two-phase multiplier also increases with increase in the inlet RH. The increase in two-phase multiplier indicates increased presence of liquid water in the channels. As the inlet RH increases, the ability of the gas stream to remove water in the vapor phase decreases, thereby increasing the two-phase multiplier. However, at these higher temperatures, the higher inlet RH keeps the membrane hydrated thereby increasing the performance. At the lower inlet RH, water is removed very effectively and thus leads to the loss in hydration of the membrane.

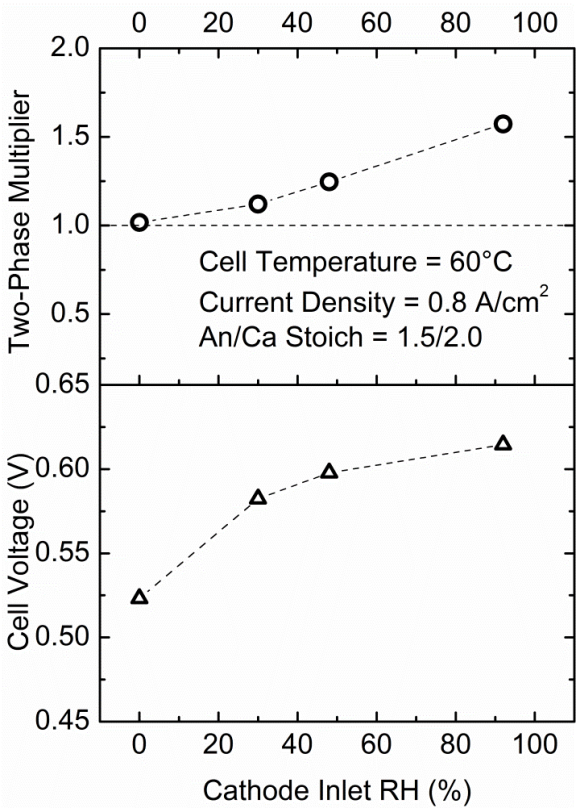

Figure 25: Effect of RH on cell performance and two-phase multiplier, at a cell temperature of 60°C.

In Figure 26, we see the results for the cell temperatures of 70 and 80°C. The results for the lower inlet RH values are not reported. Although the tests were performed at the lower RH settings, stable operation of the fuel cell could not be established due to the onset of membrane dehydration. Therefore, the results under conditions of membrane dehydration have not been reported in these plots.

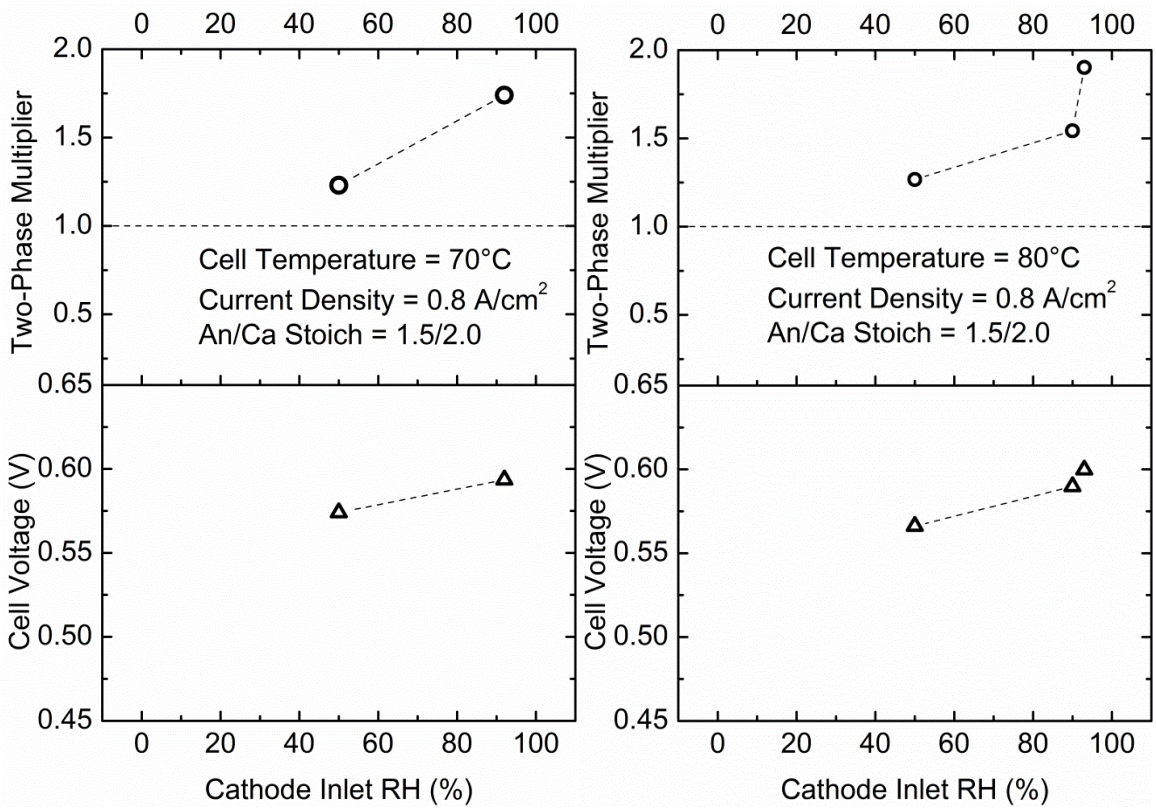

Figure 26: Effect of RH on cell performance and two-phase multiplier, at a cell temperature of 70°C and 80°C.

Relationship between cell voltage to two-phase multiplier

Figure 27 shows the cell voltage as a function of the two-phase multiplier for different temperature conditions. The two-phase multiplier cannot be controlled as an independent variable, but depends on the saturation conditions within the flow fields. Therefore, changing the temperature and the inlet relative humidity can result in different two-phase multipliers. Two different trends were observed for the cell voltage with increasing two-phase multipliers. At the lower temperatures, below 60°C, a two-phase pressure drop multiplier above 1.5 indicated the start of flooding conditions and resulted in a loss in the performance. However, at the higher temperatures (60°C and above), increasing the two-

phase multiplier improved the performance. Using dry gases resulted in very low two-phase multipliers but also led to the dry-out of the membrane resulting in very low performance. From this we may conclude that a lower two-phase multiplier is preferred at the lower temperatures and a higher two-phase multiplier is preffered at the higher temeprature. Additionally, this information can be used to diagnose the flooding and dry-out scenarios in operating single cell and stacks of PEMFCs.

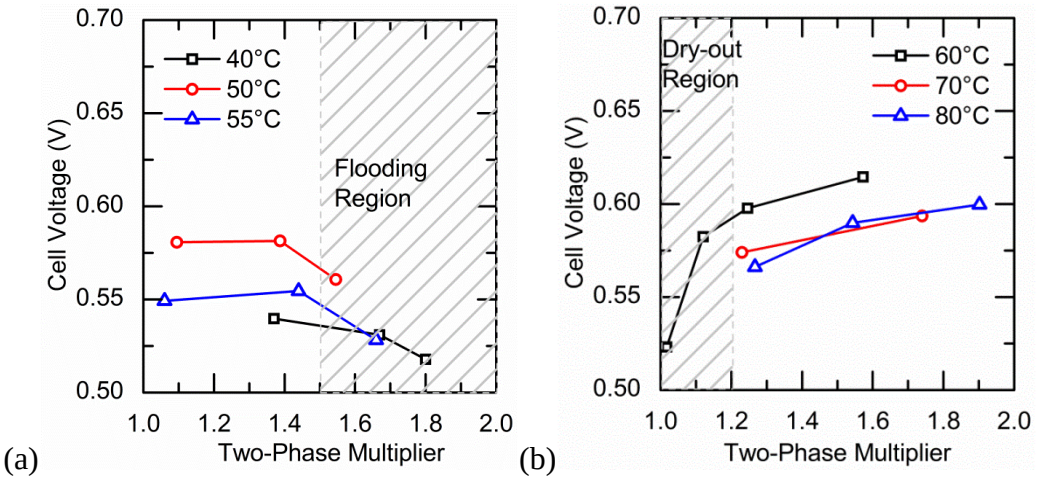

Figure 27: Cell voltage as a function of two-phase multiplier indicating flooding and dry-out conditions. (a) At low temperatures, a high two-phase multiplier results in flooding and decrease in performance. (b) At higher temperatures, a low two-phase multiplier indicates membrane dry-out, again decreasing the performance.

3.4. Discussion of Findings

This investigation was aimed at identifying the impact of liquid water on the performance of PEMFCs. The impact of liquid water was characterized by the two-phase multiplier whereas the performance of the fuel cell is characterized by the cell voltage (for a constant current density). In order to vary the quantity of liquid water in the reactant channels, the saturation pressure of water in air needs to be manipulated. Cell

temperature and the relative humidity of the incoming reactant gases dictate the saturation conditions in the reactant channels.

With increasing temperature, the saturation pressure increases. In the first part of the study, we observe that with decreasing quantity of liquid water in the reactant channels (due to decreasing two-phase multiplier), the cell performance improves. However, when the temperature is significantly high, and the two-phase multiplier is close to unity, the cell performance begins to decrease. This clearly shows the presence of an optimum quantity of liquid water to remain present in the system for the performance to be at its maximum. An increase in the liquid water results in the onset of cell flooding, increase in mass transport losses and therefore a decrease in the cell performance. On the other hand, if there is too little water in the system, the membrane begins to suffer from dehydration, leading to increased protonic resistance and therefore a loss in the cell performance. This reinforces the requirement of an optimum quantify of liquid water in the reactant channels.

It was observed that the change in behavior occurs at 60°C and therefore the findings from the change in inlet RH was categorized into temperatures below 60°C and the test cases at or above 60°C. Below 60°C, three test temperatures were considered, i.e. 40, 50 and 55°C. All three conditions showed similar behavior of increase in the two-phase multiplier and a decrease in cell performance with increase in the inlet RH of the cathode stream. Therefore, increase in liquid water in the reactant channels promoted flooding tendencies resulting in loss in cell performance.

At the higher temperature, tests were performed at 60, 70 and 80°C. At these cell temperatures, with low inlet RH conditions, an onset of membrane dehydration was observed. This can be verified for the temperature of 60°C in Figure 17 to 20, where we observe the cell resistance to be increasing on reaching 60°C and we see a drop in the cell performance. For temperatures of 70 and 80°C, when the cell was operated at the lower inlet RH values of 0 and 25%, a stable operation could not be achieved. The cell voltage would fluctuate and the cell performance would not provide a steady operation for the data to be recorded. Therefore, it is clear that the membrane was losing hydration and therefore a sustained operation was not possible.

At these higher temperature (≥60°C), a reversal in the trend is observed. With increase in inlet RH, the two-phase multiplier continues to increase. The performance, unlike at the lower temperatures, also continues to increase. This shows, that at the higher temperatures, even with humidified reactant streams, there is no onset of flooding. The high air velocities and very high saturation pressure allow for efficient removal of water, so as to prevent the onset of flooding. The increased quantity of liquid water present in the reactant channels allows for good membrane hydration. Therefore, the protonic conductivity is sustained and the cell continues to improve its performance. At the higher temperatures, the activation energy is lowered, resulting in lower activation potential and improved cell performance.

The final results section shows the presence of a relationship between the two-phase multiplier and the cell performance. Although, the two-phase multiplier is not a controlled parameter, it is a direct function of the saturation conditions and can be manipulated by changes in the reactant flow rates. From Figure 27, we inferred that a

two-phase multiplier higher than 1.5 is indicative of cell flooding, especially at the lower temperatures. It is also observed that a two-phase multiplier of lower than 1.2, is indicative of the onset of membrane dryout. This provides a clear overlap between the two conditions. The overlap region is $1.2 < \varphi < 1.5$. This can be utilized in the form of a diagnostic tool for the performance of the fuel cell.

A significant portion of the PEMFC stack cost is towards the measurement of individual cell voltages in order to monitor their performance and take precautions to prevent cell reversals. Cell reversals result in significant degradation of the membrane. The new diagnostic technique can be put in use with a single manifold-to-manifold differential pressure transducer monitoring the pressure drop between the manifolds in real time. When the fuel cell is being operated, the manifold-manifold pressure drop can be mated to a real-time data processing system (e.g. LabVIEW®) to obtain the two-phase multiplier. The single-phase pressure drop needs to be established before the operation, under no-load conditions, and fed into the data processing system as the baseline pressure drop. When the flow conditions change (due to change in temperature, flow or inlet humidification) and the multiplier drops below 1.2, the flow rates can be decreased to get higher multipliers. Conversely, if the multiplier increases to values greater than 1.5, the cell starts to flood; the flow rates can be increased remove the water blockages and counter the flooding behavior. Therefore, the real time two-phase multiplier can be used as a low cost, non-destructive diagnostic tool, to identify and monitor the optimal operation of the fuel cell.

3.5. Summary of Performance Predictions from Water Management

The current study investigates the relationship between the liquid water present in the reactant channels and the cell performance. Temperature of the cell and the inlet relative humidity of the reactant gases play a key role in impacting the quantity of liquid water in the reactant channels, as they both influence the saturation pressure of the water in air. These two operating parameters are changed parametrically to impose different liquid water content in the reactant channels and the effect on performance is investigated. The two-phase pressure drop multiplier is used to quantify the effect of liquid water present in the reactant channels. The following conclusions can be drawn from the current investigation:

i) Two-phase multipliers decreased with increase in current density as the air flow velocity increased and improved water removal characteristics.

ii) Cell resistance decreases with increase in temperature. This is due to reduced mass transport resistances with reduced water content. However, at 60°C with dry gases, the cell resistance begins to increase due to loss in hydration of the membrane.

iii) Two-phase multipliers decrease with increase in temperature due to increased removal of water in the vapor phase.

iv) Loss in cell voltage due to cell flooding is more pronounced compared to voltage loss due to membrane dehydration. Therefore operating the cell in partly dry conditions is better than operating under flooding conditions.

v) Cell voltage prediction using the relationship given by Didierjean et al. [139] works accurately under optimum hydration conditions. However, it does not bring cell flooding and membrane hydration into discussion.

vi) At the lower temperatures of 40 and 50°C, the cell performance decreases with an increase in inlet RH as the cell begins to flood and therefore the mass transport resistance increases. At the higher temperature of 60 and 70°C, the cell performance increases with an increase in the inlet RH. For higher temperatures, with dry gases, the water removal rate is very high and therefore leads to loss in hydration of the membrane. With increasing RH, the membrane hydration is improved and therefore the cell performance increases dramatically.

vii) At lower temperatures (below 60°C), a lower two-phase pressure drop multiplier results in better performance. At higher temperatures (at or above 60°C), a two-phase pressure drop multiplier should be higher than 1.2 to avoid dry-out tendencies of the membrane. This information can be used to diagnose cell flooding and membrane dry-out in operational PEMFCs.

viii) A two-phase pressure drop multiplier has been proposed as a diagnostic tool for the accurate prediction of cell flooding and membrane dehydration in operational PEMFCs.

ix) The work done in this section has been submitted to the International Journal of Hydrogen Energy and is currently under review.

4. Visual quantification of liquid water in the cathode reactant channels

The previous study shows the value of the two-phase multiplier as a diagnostic tool in predicting the performance of PEMFC under various operating conditions. However, it does not provide us with any information on the flow patterns dominant in the reactant channels. Finally, there also exists the need to introduce a parameter to quantify the mass transport resistance due to the presence of liquid water in the reactant channels. This study addresses these issues by quantifying the liquid water in the cathode reactant channels through a two-phase flow visualization study.

The liquid water present in the gas channels affects the performance in two ways. Increased flow resistance decreases the reactant flow and causes localized starvation down the channel from the liquid water features. It also reduces the area available for diffusive mass transport into the GDL and increases the diffusion resistance for the reactants. Therefore it is important to quantify the liquid water present in the gas channels.

Transparent fuel cells have been used by different researchers to understand the behavior of liquid water in the reactant channels of an operating PEMFC [43,46,78,84–86,89,103–107,110]. However, most studies have focused on the qualitative evaluation of the liquid water features, such as identification of flow patterns, without providing quantitative information. Additionally, visualization cells are often modified from the standard structure and therefore result in decreased performance. Therfore, there is a dearth of visualization data at the higher current densities, although state-of-the-art fuel cells today

are capable of operating up to current densities of 3.0 A/cm^2. This section of work is an attempt at quantifying the liquid water present in the reactant channels using image processing techniques. The findings of this segment of the work have been published in the Journal of Power Sources in the February 2014 issue [140].

4.1. Objectives of Visual Quantification

Although several attempts have been made to quantify the liquid water in the PEMFC gas channels, a systematic study showing the effect of operating conditions on the liquid water presence in the cathode reactant channels is still lacking. This work attempted to generate quantitative data in the form of area coverage ratio (ACR) and to establish trends for two-phase flow in PEMFC gas channels. An ex-situ experimental setup was used to emulate the cathode side gas channels of the PEMFC. A modified form of the algorithms used by Sergi and Kandlikar [40] were utilized in this work to obtain water quantification data at different flow and temperature conditions.

An optical imaging system was selected for this work because of the high spatial and temporal resolution and the ease of operation. Previous works had shown the feasibility of using optical imaging systems to observe and investigate the two-phase flow in PEMFC reactant channels. However, a common problem encountered in using an optically visual cell is mass transport driven cell performance loss at low current densities. Current densities above 1.0 A/cm^2 have not been reported in the in situ visualization studies due to this problem. However, state-of-the-art fuel cells are able to achieve much higher current densities (up to 3.0 A/cm^2) and therefore an ex-situ study

was necessary to complement and provide the quantification data for liquid water presence in the channels. The aim of this study was to provide the quantification of liquid water in the PEMFC reactant channels for different operational conditions simulated in an ex-situ setup.

The liquid water coverage of the GDL surface reduces the available surface area for gas transport from the channels to the catalyst layer. Quantifying this effect, in terms of the ACR as a function of operating parameters was the major goal of this work. The results discussed in this work can directly be incorporated into a modeling effort, and used as a reduction in surface area for gas transport and a flow resistance in the reactant channel. The down-the-channel (DTC) modeling effort, by General Motors (GM) as outlined in section 1.6 plans on utilizing the data presented here.

4.2.Experimental Setup for Ex situ Visualization Study

An ex-situ setup was used for this work. The setup was modified from an earlier setup used in previous studies [32,64,88]. Being an ex-situ setup, the electrochemical reaction was not taken into consideration. A schematic of the test setup is shown in Figure 28 and a cross sectional view is given in Figure 29.

Ultra zero grade air was supplied from pressurized bottles. The flow was metered, based on the equivalent current density being tested. The volumetric flow rate of air required to sustain an equivalent current density with appropriate stoichiometry (of 2) was calculated at room temperature and atmospheric pressure using Faradays' law, shown here using

equations 9 - 11. The calculations steps and values used have been elaborated in Appendix 10.2.

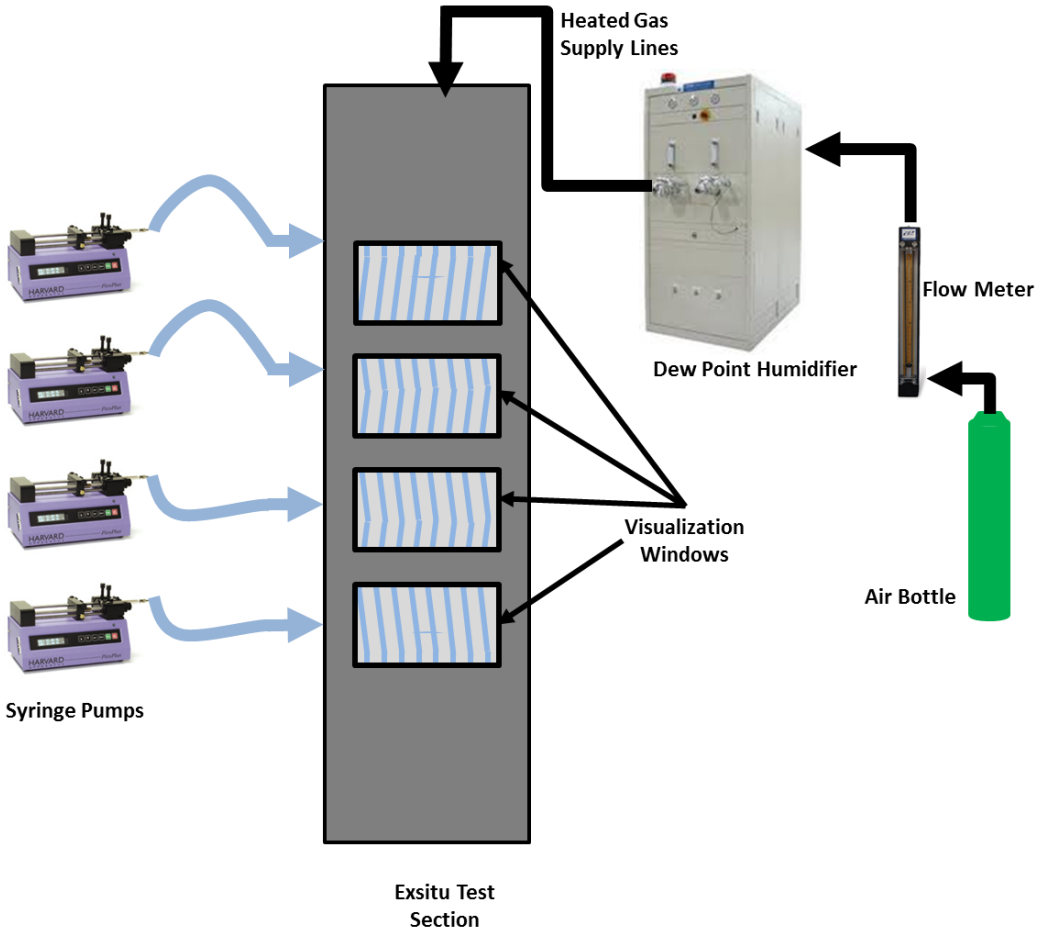

Figure 28: Schematic of the ex-situ test setup used in this section of the work. The four visualization windows are used to observe the two-phase flow interactions at four locations along the channel length.

Table 4 shows the corresponding air flow rate and rate of water generation calculated for each current density. The air was heated and humidified to the appropriate level using an Arbin dew point humidifier (DPHS-D50), which controlled the dew point and gas temperatures. The gases were delivered to the test section via heated gas lines to ensure

no loss in temperature and to avoid condensation. The test section was heated to ensure an isothermal setup. Two sets of electrical heaters were used to heat the front and back plates. Twelve thermocouples were placed throughout the test section and the heater plates to monitor the system temperature. Any change in temperature was compensated accordingly to bring the temperature back to testing conditions.

$$\dot{m} = \frac{iA}{nF} \tag{9}$$

$$Air\ Flow\ Rate = \frac{iA}{nF} * Stoic * \frac{1}{0.21} * Molecular\ Wt. \tag{10}$$

$$Water\ Flow\ Rate = \frac{iA}{nF} * Molecular\ Wt. \tag{11}$$

The test section shown in Figure 29 consisted of heater blocks, gas channels, water channels, and the GDL. The GDL was compressed between the air channel and the water channels. The dimensions for the air channels represented the reactant channels on the cathode side. The water channels distributed water evenly over the MPL side of the porous media, mimicking water generation at the catalyst layer. The water channels were supplied through a buffer of water chambers which damp out any pressure fluctuations from the syringe pumps. The water chambers were also heated to ensure the water was injected into the system at isothermal conditions. Four separate chambers were used to promote an even distribution of water along the length of the channels, and reduce the effect of hydraulic pressure due to the height of the liquid above. A single chamber would have led to increased flow towards the lower end of the channel and a low flow at the start of the channel.

Table 4: Flow rates associated with eq. current densities reported in this work.

Eq. Current Density (A/cm^2)	Stoichiometry	Air Flow Rate (ml/min)	Rate of water generation (µl/min)
0.1	3	101	2.6
0.4	2	268	10.3
0.7	2	470	18.1
1.0	2	671	25.8
1.3	2	872	33.6
1.5	2	1006	38.7
2.0	2	1342	51.7
2.5	2	1677	64.6
3.0	2	2013	77.5

The channel design is the same as used in the earlier study as the results need to be comparable. The equivalent area under consideration (18.4 cm^2) houses 8 channels in the cathode side reactant channel configuration. The gas channels were manufactured in Lexan® for optical clarity. The contact angle of Lexan® matches graphite very closely, which is commonly used in fuel cell bipolar plates. The resulting test section simulated the water generation on the cathode side and the two-phase flow of air and water in the cathode side reactant channels.

The gas channels were supplied through an inlet manifold and the two-phase fluid was collected at the exit manifold. The manifolds also served the purpose of two-phase pressure measurement using a Honeywell differential pressure sensor with a range of 0 –

35 kPa and an accuracy of 0.25% of the full range, i.e. a maximum uncertainty of 88 Pa in the reading.

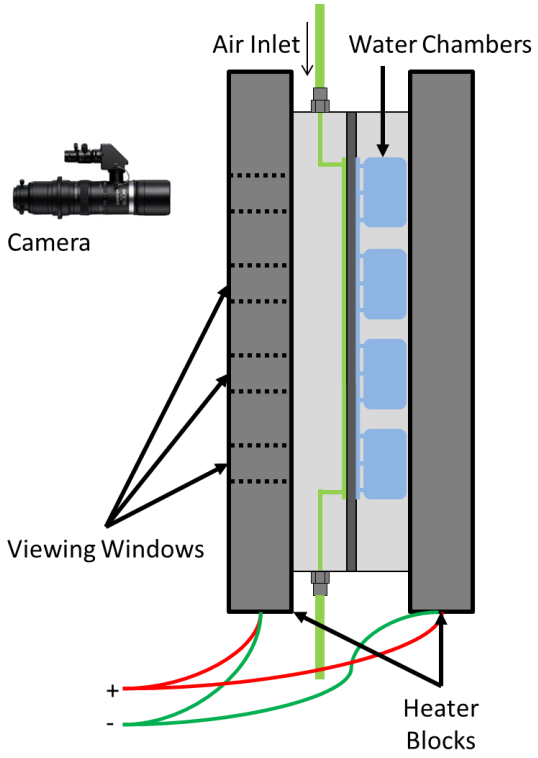

Figure 29: Cross-sectional schematic of the of the test section used in this work.

The GDL used in this work was MRC U-105 with 5 wt. % PTFE, provided by GM and coated by GM in-house with an MPL on one side. The GDL had an uncompressed thickness of 235 µm and had a PTFE gasket of 178 µm thickness surrounding it on all four sides. PTFE gasket was used to act as a 'hard stop' ensuring a known thickness after the initial compression.

Fuel cell operating conditions in automotive applications change depending on environmental conditions, operational time and performance requirement. Gas

temperatures being supplied to the cell start at ambient temperatures, though they are supplied at higher temperatures later. The cell temperatures reflect the ambient temperatures at start-up. As the time of operation increases, the cell reaches higher temperatures due to the heat generated (which can be up to 100 kW for a commercial stack). Cell temperatures are maintained using a cooling system. Different cooling techniques used for regulating temperatures within the fuel cell are discussed by Zhang and Kandlikar [51]. The cell temperatures are often maintained between 60 and 80°C to obtain high cell efficiency and for efficient water removal [11,50,141,142]. One of the parameters investigated in this study was the effect of different temperatures on the liquid water coverage in the reactant channels. However, for short commutes and during start-up conditions, the cell is operating at sub-optimal temperatures. This constitutes a significant portion of the drive cycle of the PEMFCs. Therefore, lower temperatures also need to be studied when focusing on the water behavior in the fuel cell reactant channels.

At 80°C, the saturation pressure increases significantly as compared to 20°C (2.62 kPa at 22°C vs. 51 kPa at 80°C [7,143]) and the mass of water required to saturate the air stream is much higher. This was also explained using equation 6 and Figure 11. If dry gases are introduced at the inlet of the fuel cell, the water being generated at the cathode catalyst layer is insufficient to keep the membrane hydrated. Therefore inlet gases are humidified in order to maintain the hydration of the membrane. Changing the humidification of the incoming reactant gases would in effect change the saturation condition of the channel and impact the ACR. The effect of different levels of humidification of the inlet gases on the liquid water coverage in the reactant channels has been studied.

A typical polarization curve and a power generation curve show that peak power density is obtained at higher current densities (Figure 4). Increased current densities require higher air flow rates and result in higher air flow velocities. They also result in higher pressure drop along the length of the channel. Table 4 maps the different air flow rates required for the different current densities and the rates of water generation. The stoichiometry used to calculate the air flow rates is 2 for all conditions, but is changed to 3 for the current density of 0.1 A/cm^2. The higher current density is used to match the data with in situ studies which are limited by the operation of the fuel cell and require a minimum flow rate to maintain a stable voltage. Higher flow rates are required to minimize the losses and keep the reaction going. The resulting set of test conditions is shown in Table 5.

Table 5: Matrix of experimentally tested conditions used in the ex situ visualization study.

Tested Parameters	Values
Eq. Current Density	0.1 – 3.0 A/cm^2
Temperature	23, 40, and 60°C
Relative Humidity of inlet gases	0, 50, and 100% RH
Stoic	2 (3 for 0.1 A/cm^2)

For obtaining the liquid water coverage in the gas channels, videos were recorded at 30 frames per second for 360 seconds at each of the four windows. A shutter speed of 1/250 seconds was employed to reduce blurring of images in case of faster moving water features. Spernjak et al. [78] highlighted the fast moving water features in the reactant

channels, prompting our decision to use a high shutter speed in order to reduce the blurring of the images. The total time required for recording at each window was 6 minutes with equal time required to save the file, requiring 48 minutes to capture videos for all four windows.

Linear motorized stages manufactured by Velmex Inc. were used to accurately and repeatedly position the camera to exactly the same location on each window. This allowed test videos to be recorded at the same locations for each condition. In addition to the test videos, dry videos were recorded before introducing any water to the test sections. These dry videos were used to provide reference frames for detecting water in the test videos.

Pressure drop was recorded using the differential pressure sensors described earlier. Single phase pressure drop was recorded for each of the air flow rates corresponding to the equivalent current densities shown in Table 5. During each test, the two-phase pressure drop was recorded for a total of 60 minutes to average the fluctuations in the two-phase pressure measurements. The commonly observed flow patterns of slug flow, film flow, and mist flow result in their characteristic pressure drop signatures [26,29]. The same pressure drop signatures were observed during the current tests. Averaging the pressure-drop data over 60 minutes avoided biasing from the pressure spikes associated with two-phase flow, especially in the slug flow regime.

The videos recorded, as described in this section, were subsequently processed for obtaining the ACR and the image processing technique has been discussed in detail in the following section.

4.3.Methodology of Image Processing

The videos recorded as part of the testing protocol are used to quantify liquid water in the gas flow channels. Figure 30 shows the image of the reactant channel with water features visible through the Keyence VW 6000 motion analysis microscope with the VW – Z2 lens. The lens was specifically used for the large working distance required to keep the camera and the lens away from the heated compression plates and to account for the thickness of the compression plates, making the flow field significantly distant from the camera. The liquid shows up darker on the surface of the GDL compared to the surrounding materials due to its high absorbance of the incident light.

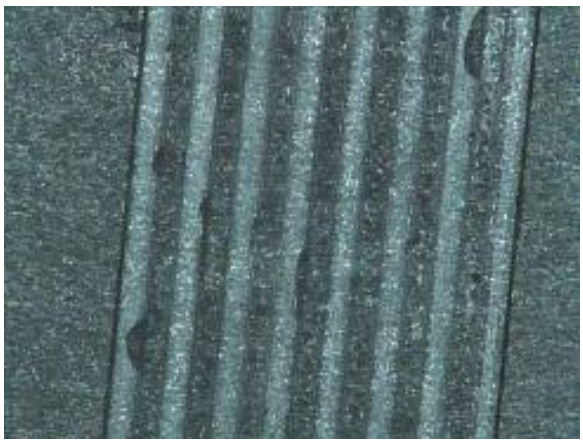

Figure 30: Liquid water present in the reactant channels - observed through Keyence VW6000 motion analysis microscope with a VW-Z2 lens.

Each test video is treated as a sequence of images and an algorithm was developed in MATLAB® to extract the relevant information about liquid water present in the channels. The water is quantified as the Area Coverage Ratio (ACR) and is defined as the fraction

of the interfacial area covered by liquid water present in the gas channels. Another algorithm is used to identify the water features present in the channels, classifying them in terms of slug flow or film flow. Details of both algorithms are mentioned in the following sections.

Morphological Operations for ACR

Morphology is the analysis of spatial structures [144]. Morphological image processing is used to detect water features in the current study. This sub section discusses the different morphological terminology discussed in the chapter.

In morphological operations, a key element is the 'probe' used to inspect, quantify and process the image features. This 'probe' is known as the structuring element (SE). The morphological processing involves the fitting or not fitting of the structuring element in the image. Therefore the information extracted from the image is dependent on the structuring element used [145]. In this study, we investigate two dimensional objects, or water features. Therefore, we use a two-dimensional structuring element. A disc of radius 5 pixels is used as the structuring element.

Erosion of an image object A by the structuring element B is represented in set theory as shown in equation (12), and is defined as consisting of all points x for which the translation of B by x fits inside A. For a structuring element with the origin inside, erosion results in a shrinking effect. Small uneven edged and sharp objects are removed using this process. Figure 31 shows the effect of erosion on an image object shown in part (a) and (c). If an object does not fit in the structuring element, the object is removed.

$$A \ominus B = \{x | B_z \subseteq A\} \quad (12)$$

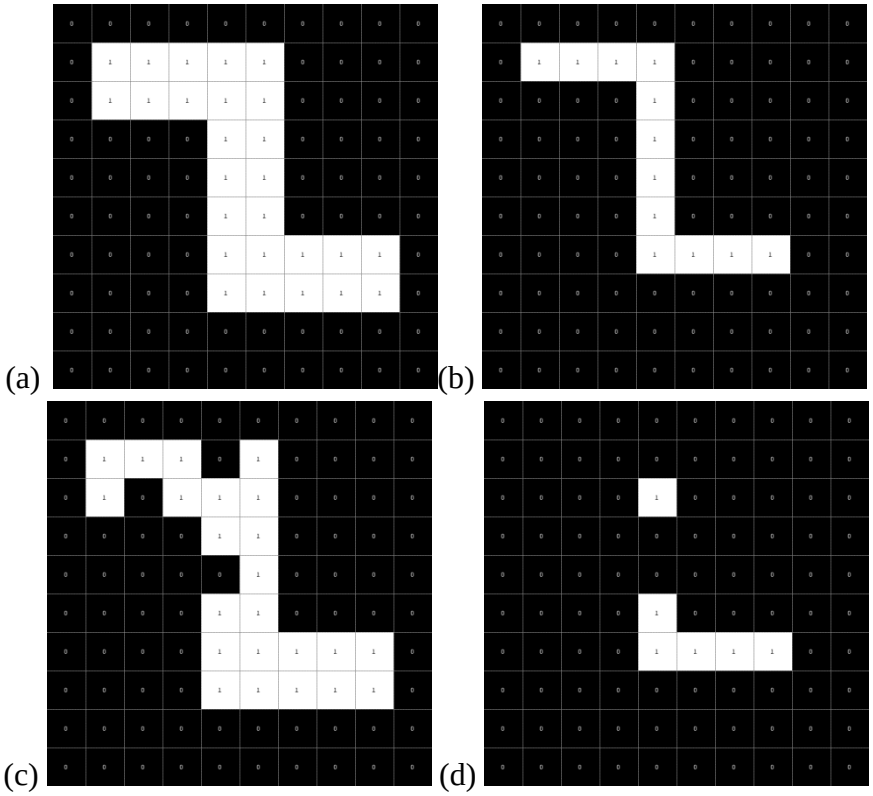

Figure 31: Effect of erosion on an image object (a) is eroded to get (b) and (c) is eroded to (d).

Dilation of the same image object A by the structuring element B is represented in set theory as shown in equation (13), and is defined as the locus of points where the structuring element lies inside the dilated object. For a structuring element with the origin inside, dilation results in a thickening effect. Small uneven edged and sharp objects are removed using this processing by filling them in. Figure 32 shows the effect of dilation on an image.

$$A \oplus B = \{x | [B_z \cap A] \subseteq A\} \quad (13)$$

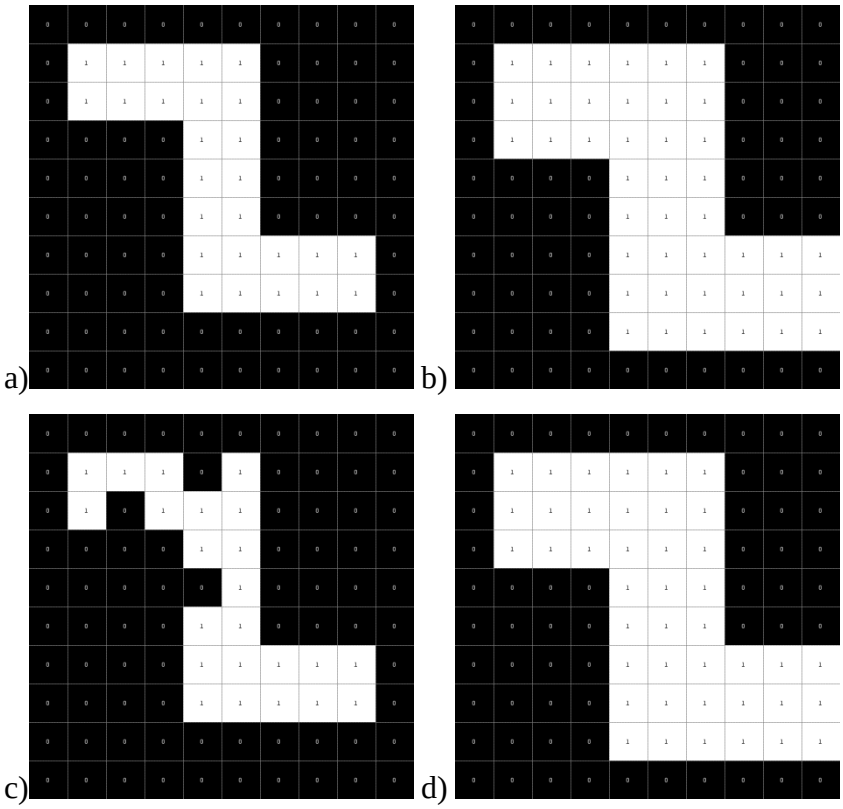

Figure 32: Effect of dilation on an image object (a) is dilated to get (b) and (c) is dilated to (d).

Opening (shown in equation (14)) is defined as erosion followed by dilation. It is often used to remove noise from the images.

$$A \circ B = (A \ominus B) \oplus B \quad (14)$$

Closing (shown in equation (15)) is defined as dilation followed by erosion. It is often used to close holes in the image objects that have developed due to noise in the images.

$$A \bullet B = (A \oplus B) \ominus B \quad (15)$$

Pixel connectivity is used to understand whether a particular feature / object in an image is large enough to be considered in the processing. The water features considered in this study need to be larger than a threshold size to be considered in the quantification. Objects, smaller than this threshold, are ignored in this study due to their similarity with noise. Two types of pixel connectivity can be considered. The first is 4-connectivity and requires the pixel being probed to be connected on the north, south, east and west directions. 8-connectivity requires the pixel being probed to be connected on the north-east, north-west, south-east and south-west directions along with the four directions discussed before. A connectivity of 8 is used in the algorithms presented here.

For a more in-depth understanding of the operations discussed here, refer to [144–146]. With this information about the morphological processing techniques used, we delve into the algorithms used in this investigation.

Area Coverage Ratio Algorithm Development

The algorithm developed for obtaining the Area Coverage Ratio (ACR) processes each video on a frame by frame basis. A graphic representation of the algorithm is shown in Figure 33. The first phase of the algorithm is responsible for image segmentation. Image segmentation is the division of an image into different regions based on specific properties [144]. In this case, image segmentation is used to identify the regions of liquid water within each image frame. A reference frame (R_{ij}) was obtained by averaging frames from a dry video as shown in Figure 34. The test video was processed one frame at a time, and finally compiled into an output video for optical evaluation of the

processing accuracy. As a first step in the algorithm, the reference frame was subtracted from test frame (W_{ij}) to obtain a difference image frame (D_{ij}) as shown in equation (16).

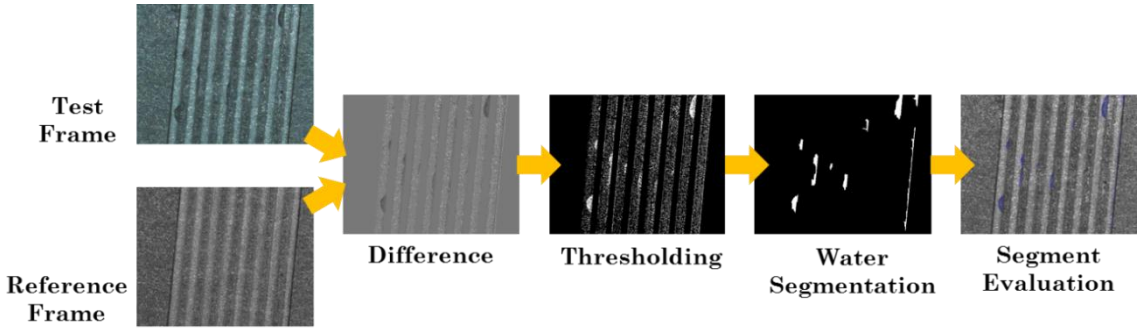

Figure 33: Graphical representation of the algorithm used for ACR (Area Coverage Ratio).

$$D_{ij} = W_{ij} - R_{ij} \tag{16}$$

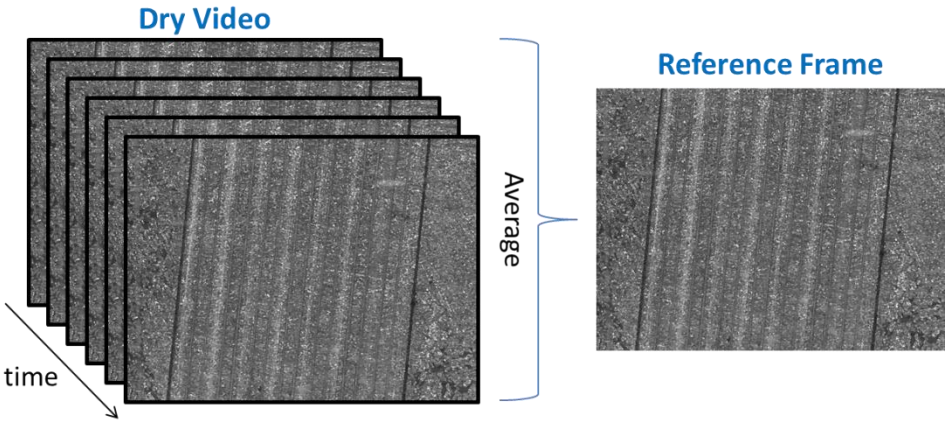

Figure 34: Reference frame obtained by averaging frames from a dry video.

The liquid water shows up much darker in the test frames, compared to the surrounding dry GDL, due to absorption of the incident light, providing significant contrast between GDL regions and water regions. Thus, a single sided threshold is adequate to isolate the regions of liquid water in the channels (eq. (17)), producing the threshold image (G_{ij}). The difference image is evaluated for pixel intensities, with pixels below a threshold value representing water regions. The pixels identified as water regions are allocated the value of 1, while the remaining regions are 0. Thus, a binary image of the water locations is obtained.

$$G_{ij} = \begin{cases} 1 & D_{ij} > Threshold \\ 0 & D_{ij} < Threshold \end{cases} \quad (17)$$

A binary mask file was created from the reference frame (Figure 35). Channel regions are foreground (1s) and land regions are background (0s). The threshold image (G_{ij}) is multiplied by the mask file to restrict future processing steps to the channel regions only. At this step, the water regions have been isolated. However, both the reference image and the test image contain 'noise' which percolates through the above stages to the threshold image. Morphological image processing steps need to be applied to refine the water segmentation.

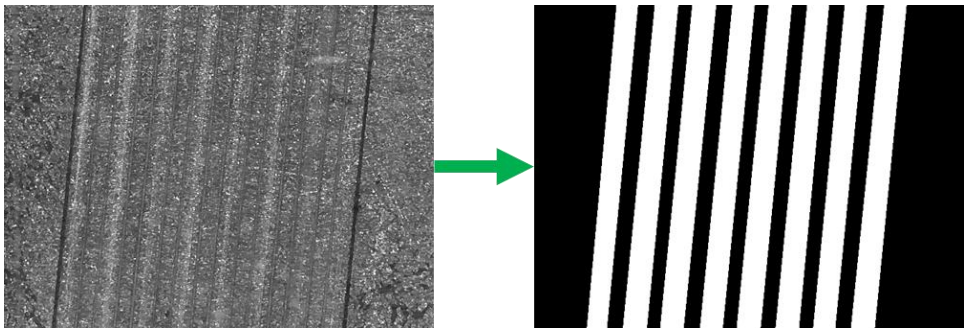

Figure 35: Creating mask file from reference frame

Morphological processing had been shown to be important for accurate detection of water by Sergi and Kandlikar [46]. The first step involves checking for connected clusters of pixels in the foreground. 100 pixels were chosen as representative of small water features. For checking for irregular structures such as water features, 8-connectivity is used. Water features larger than 100 pixels remain, while smaller features are considered as noise and are discarded. Just as noise can be detected as water pixels, noise can result in some water pixels to be below the threshold and therefore be neglected. However, holes can be filled in the binary image [144], by checking for connection with the background pixels. If a region of background pixels exists completely surrounded by foreground pixels, they are converted to foreground. This is implemented using a predefined MATLAB® function.

A closing operation is used as the final step of the morphological processing phase. The closing operation is a dilation step, followed by an erosion step. It is used to smooth the contours of the foreground water features. A disc of 5 pixel radius is used as the structuring element for best results. This concludes the morphological processing, and provides the final binary image identifying the liquid water features.

This foreground of the binary image is converted to a faint blue and then added to the original test frame. The frames are finally stacked up to form the final video output. The output video highlights the water regions in faint blue so that they can be visually inspected for the quality of the processing (Figure 36).

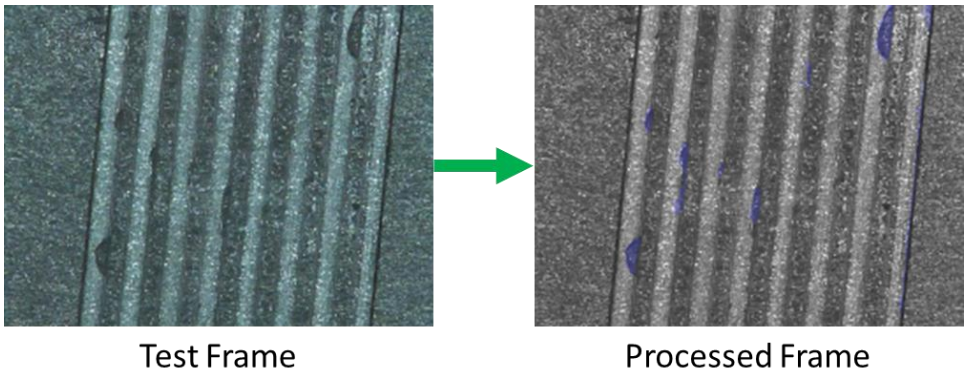

Figure 36: Processed frame is used for visual inspection of processing quality.

The channel pixels in the mask (Figure 35) define the interfacial area between the GDL and the gas channels available for reactant transport. The final processed frame in the ACR algorithm is a binary image with the foreground pixels representing liquid water. ACR is obtained at each frame by taking the ratio of the water pixels in the processed frame to the channel pixels of the mask file. The ratio is calculated for every frame in the video. The mean ACR is reported for each window. The final ACR value to be reported for every condition is the average of the ACR values reported at each window.

$$Area\ Coverage\ Ratio = \frac{Interfacial\ area\ blocked\ by\ liquid\ water}{Total\ interfacial\ area\ of\ GDL} \qquad (18)$$

The final reported value of ACR is spatially averaged over the length of the channels and is temporally averaged over the entire recording time of 48 minutes. The 48 minutes of recording time avoids any bias in favor or against any water feature being stuck in the channel for a short time.

Flow Pattern Identification Algorithm Development

A second algorithm has been developed to identify the different two-phase flow regimes dominant in the gas channel for PEMFC conditions. Several works in literature suggested that the commonly observed flow regimes observed in PEMFC reactant channels are slug flow, film flow, and mist flow [29,32]. This algorithm builds upon the detection of water features discussed in the previous section and categorized the water features into the different flow regimes. It detected and quantified slug flow and film flow but not mist flow. Mist flow is not captured in the images and therefore cannot be quantified. Figure 37 shows the graphical representation of the algorithm.

Each test video was processed on a frame by frame basis. The first step involved numbering each water feature in an ascending order, from left to right. This was achieved using a predefined function in MATLAB® called *'bwlabel'*. This frame was then added to a mask file (discussed in Figure 35). Each of the channel regions in the mask file was numbered one. Therefore, the binary mask file universally added one to the numbered objects frame. The channels were now numbered as 1s, the land regions were numbered 0s and the water features were numbered from 2 onwards to the number of objects present.

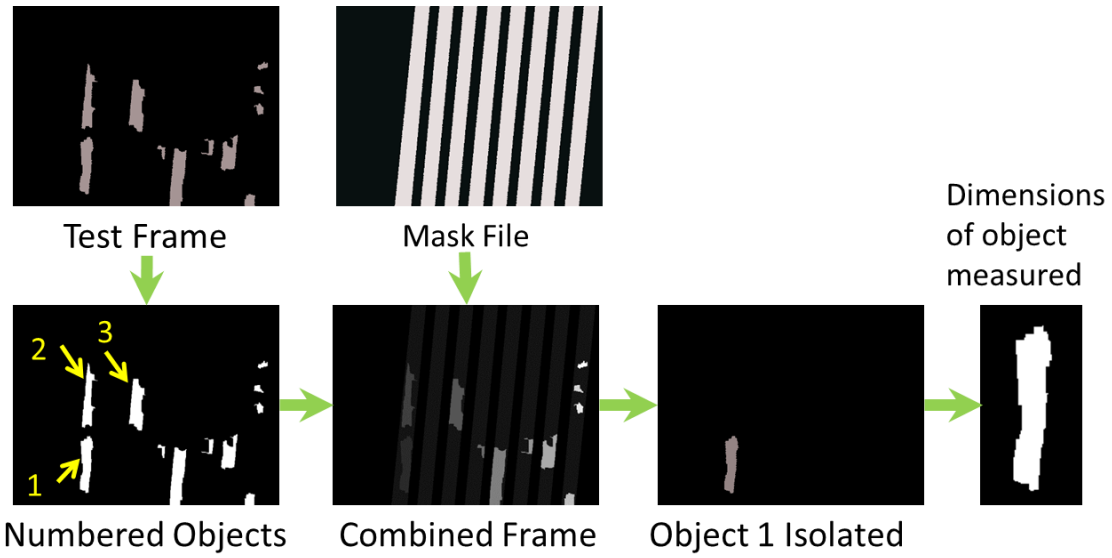

Figure 37: Graphical representation of the algorithm used to identify the flow regimes (Flow Pattern Identification Algorithm).

Each individual object was then selected and evaluated to distinguish between a slug feature and a film feature in the channel. The two sides of the water features (object) were evaluated for pixel values. If both sides were zeroes (representing land region), the object bridges the entire channel and therefore was considered as a slug, as represented in Figure 38a. If one of the sides was a pixel of value 1, it represented the object with one boundary within the channel. Thus the water feature does not bridge the entire channel and was classified as a film on the channel wall, as depicted in Figure 38b.

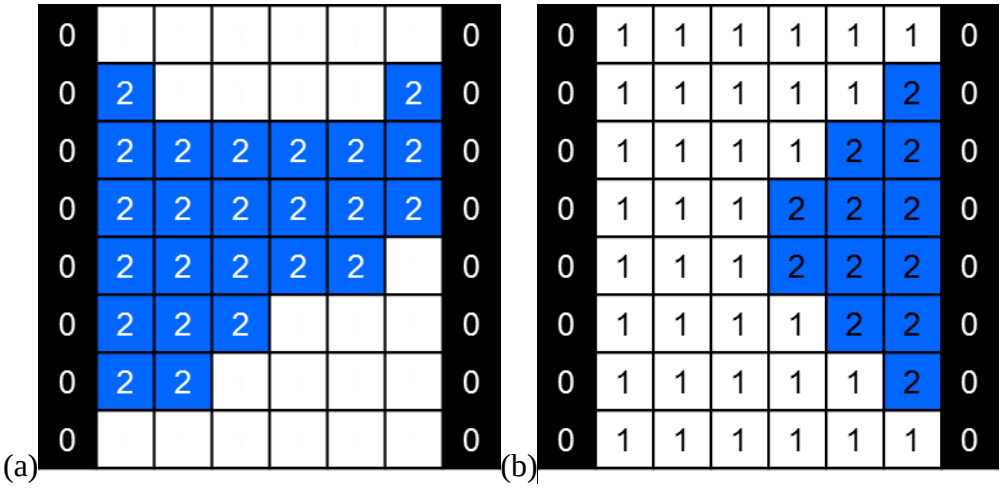

Figure 38: If the channel is completely bridged by water, it is classified as slug flow (fig a). If the channel is not bridged completely, it is classified as film flow (fig b).

Channel-to-channel Variation

When a single inlet header is used to supply a gas to multiple channels, such as in our current setup, the channels are subjected to flow maldistribution. This maldistribution in PEMFC reactant channels was documented and quantified by Kandlikar et al. [32,88]. The effect of flow maldistribution on the liquid water coverage in the gas channels has not been investigated. The information in the test videos enabled us to investigate the variation in ACR in the different channels.

Figure 39 shows a graphical representation of the algorithm used to detect the variation in liquid water presence in the different channels. The water segmented file generated in the first algorithm (area coverage ratio algorithm) is used to compare the water in the different channels. The mask file is imported and labeled from left to right in an ascending order (using the function *'bwlabel'*). The frame with the water object is added to the mask file. Each single channel mask is cycled through, to check for values greater

than 1. Once it is established into which channel the object is located, the size of the water object is assigned to the channel. Each object (in all the frames) is processed through the same process, to classify all liquid water in terms of the channel in which it is located. The process is then repeated for all frames and all videos of the tested condition.

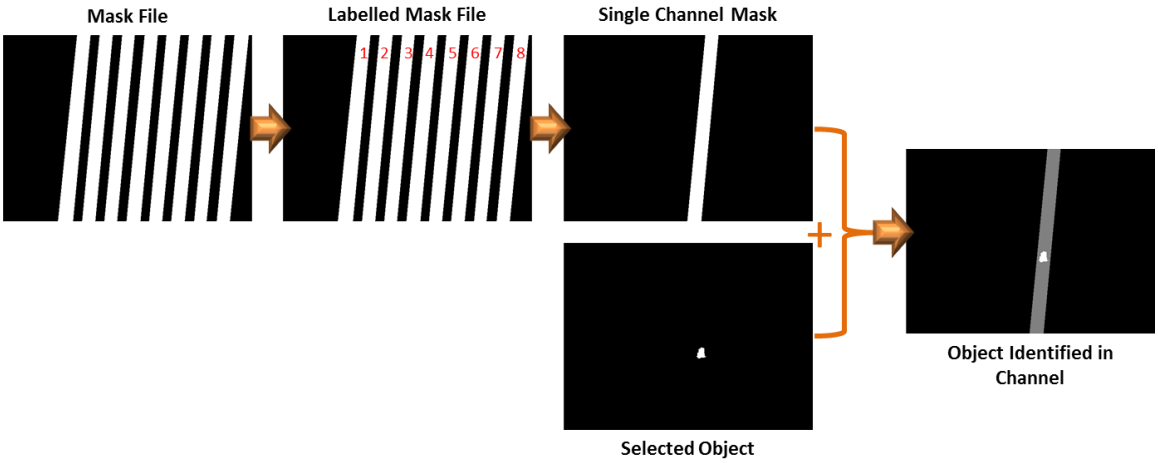

Figure 39: Graphical representation of the algorithm used to find variation in channel-to-channel liquid water area coverage ratio.

4.4.Results of Visual Quantification Study

The results from this ex-situ investigation are discussed in this section. The results from the ACR algorithm are presented, followed by the results from the FPI algorithm. The channel-to-channel variation is discussed in the third part of this section. The effects of temperature and inlet relative humidity are presented in the fourth and fifth parts of this section.

Area Coverage Ratio Results

Figure 40 shows the ACR for the setup operating at room temperature with dry inlet gases. Higher current densities along the x-axis correspond to higher air flow rates, as shown in Table 4. The higher current densities also result in higher water generation rate, which is simulated here by introducing the calculated water into the system using the syringe pumps. In Figure 40 it is seen that the ACR increases with increased equivalent current densities until 0.7 A/cm^2, and starts to decrease thereafter at higher current densities. A similar trend was also observed during in situ studies by Sergi and Kandlikar [46], although the peak ACR was observed at a lower current density. The ACR plot shows two trends. The ACR increases with increased equivalent current densities until a current density of 0.7 A/cm^2 is reached. This may be attributed to the fact that a greater quantity of water is being generated, and consequently more liquid water is being introduced into the reactant channels. The second trend observed is that of decreasing ACR at the higher current densities. This is attributed to higher air velocities, resulting in shorter residence times for the liquid water features. The liquid water is being removed at a faster rate; when averaged over time, the overall ACR begins to decrease and then stabilize as both the effects reach equilibrium. This shows that the higher air flow rates result in a more efficient removal of water from the channels.

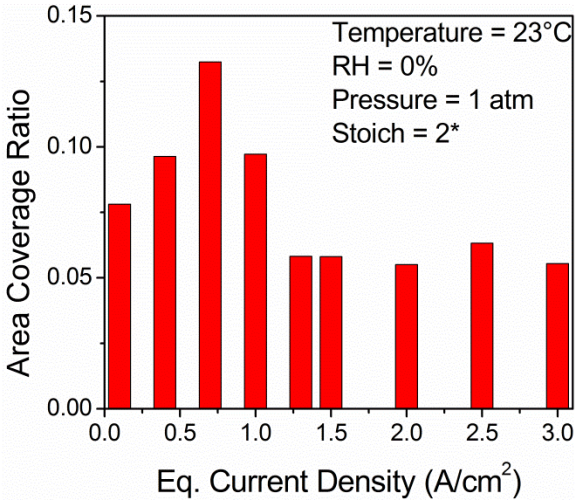

Figure 40: Area coverage ratio for a temperature of 23°C and a dry air inlet (0% RH).

Figure 41 shows the ACR obtained at 40°C with 0, 50 and 100% inlet RH respectively. For each of the conditions, we observe that the ACR decreases with increased equivalent current density. Comparing the three, we note that with 100% inlet RH, the quantity of liquid water is higher than equivalent cases with inlet gases being at 0 or 50% RH. This is expected as with a fully humidified inlet air stream, there is negligible water being removed from the reactant channels in the vapor form. ACR was also calculated for the three relative humidity conditions at 60°C (0, 50 and 100 % inlet RH). The ACR quantified in each of these conditions was on the order of 0.001, therefore negligible in comparison to the liquid water at 23 and 40°C.

As the temperature increases from 23°C to 40°C and then onto 60°C, there is a noticeable change in the trends. Instead of the dual trend observed at ambient temperatures, only a single dominant trend is observed at 40°C. The increased temperature changes the condition in two ways. One: the saturation pressure increases such that, at the lower inlet

RH values, most of the water is taken up by the air stream in vapor form, thereby leaving less liquid water in the channels. Second: the increased temperature and RH condition increases the total mass of gases flowing through the channels. This increases the air velocities, reducing the residence times of the liquid water features.

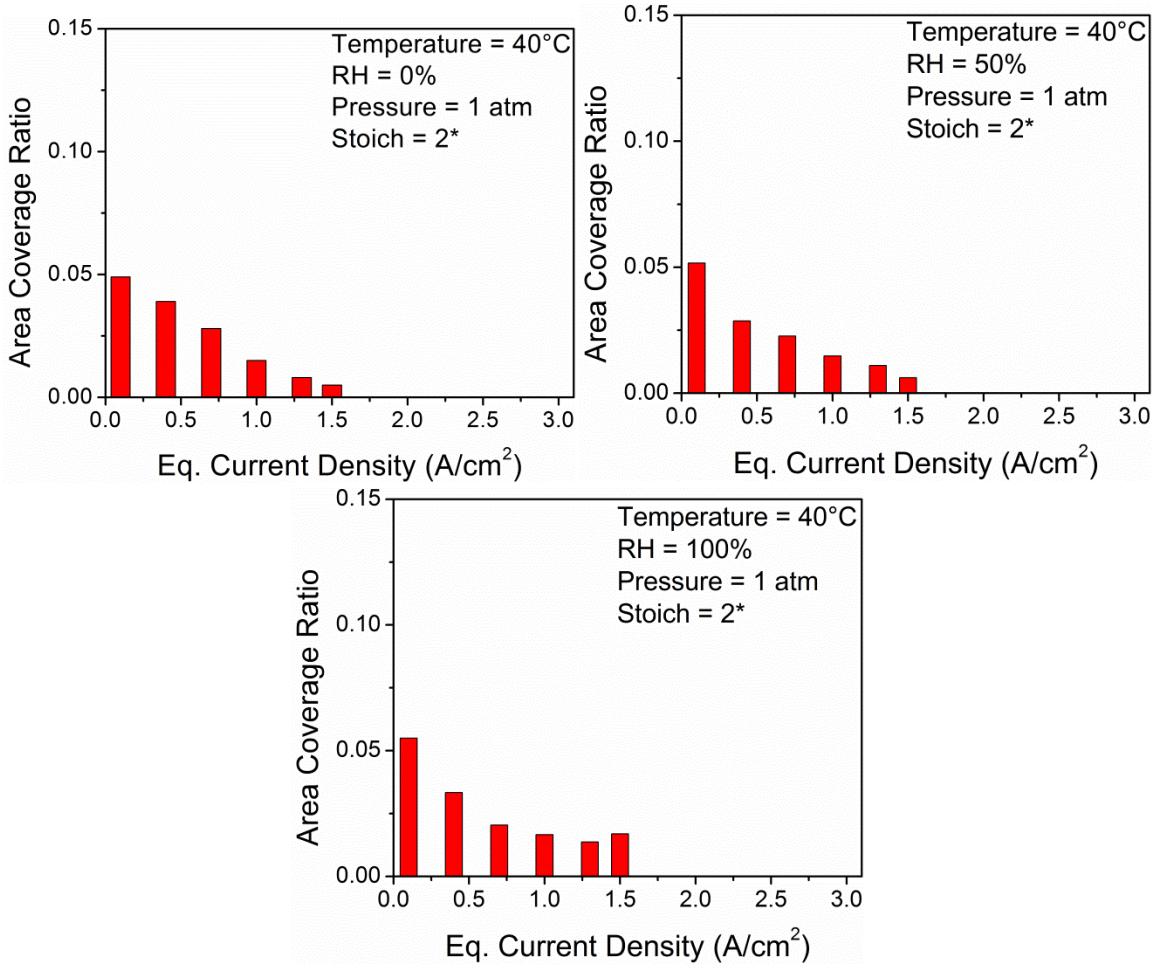

Figure 41: Area coverage ratio for temperature of 40°C, with air inlet at 0, 50 and 95% relative humidity.

Dominant Flow Patterns

Figure 42 shows the dominant flow regimes for increasing current densities at ambient room temperature of 23°C and a dry inlet condition. The total value of each data column is the ACR, which is then classified into slug flow and film flow. We can observe that the higher current densities were dominated by film flow regime, whereas significant slug flow was present at the lower current densities. The occurrence of slug flow decreases with increasing current densities and there is no significant slug flow after 1.0 A/cm^2.

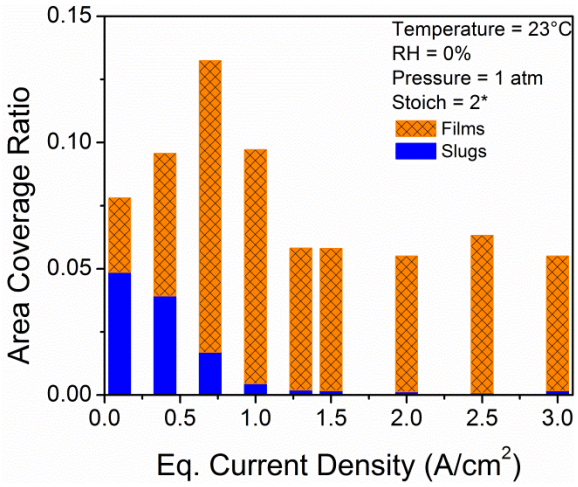

Figure 42: Dominant flow patterns for temperature of 23°C with dry air inlet (0% RH).

Figure 43 shows the two-phase pressure drop multiplier for the tests conducted at ambient temperature. From the figure, we observe that the two-phase multiplier decreases with increased equivalent current densities. At the lower equivalent current densities, slug flow is dominant (as seen in Figure 42) resulting in the higher two-phase multiplier. As the current density increases, air flow velocities increase, resulting in increased contribution of film flow. The two-phase multiplier decreases with increased contribution of film flow. Beyond an equivalent current density of 1.0 A/cm^2, we note that the ACR is

primarily in the film flow regime, and the two-phase multiplier decreases to an asymptotic value of 1.2. It can be observed that the two-phase multiplier reflects the findings of the ACR. As the flow becomes dominated by film flow, the channel is only partially blocked by the liquid water, allowing reacting gases to flow past through a constricted section. This allows a lower two-phase multiplier and is less of an issue for reactant distribution.

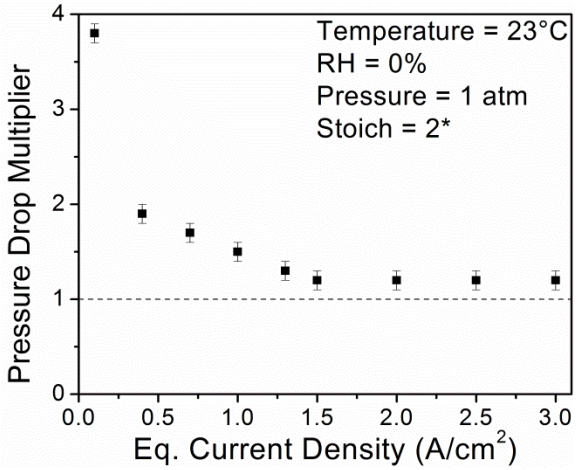

Figure 43: Two-phase pressure drop multiplier for temperature of 23°C and dry air inlet (0% RH).

Figure 44 shows the flow regimes present at different current densities at a temperature of 40°C. For dry inlet condition, only the lowest current density of 0.1 A/cm^2 has some slug flow, and the film flow is dominant. This minimal slug flow is not present for the condition of 50 and 100% inlet RH. The higher current densities are dominated by the film flow only. Therefore, at the higher temperatures, only film flow is present in the reactant channels. The increased temperature leads to higher saturation pressures, leading to more water removal in the vapor and therefore less liquid water in the channels. The ratio of water to air reduces thereby promoting film flow. Additionally, the increased air

velocities (due to the increase in temperature and RH) lead to film flow being the dominant flow regime at these conditions.

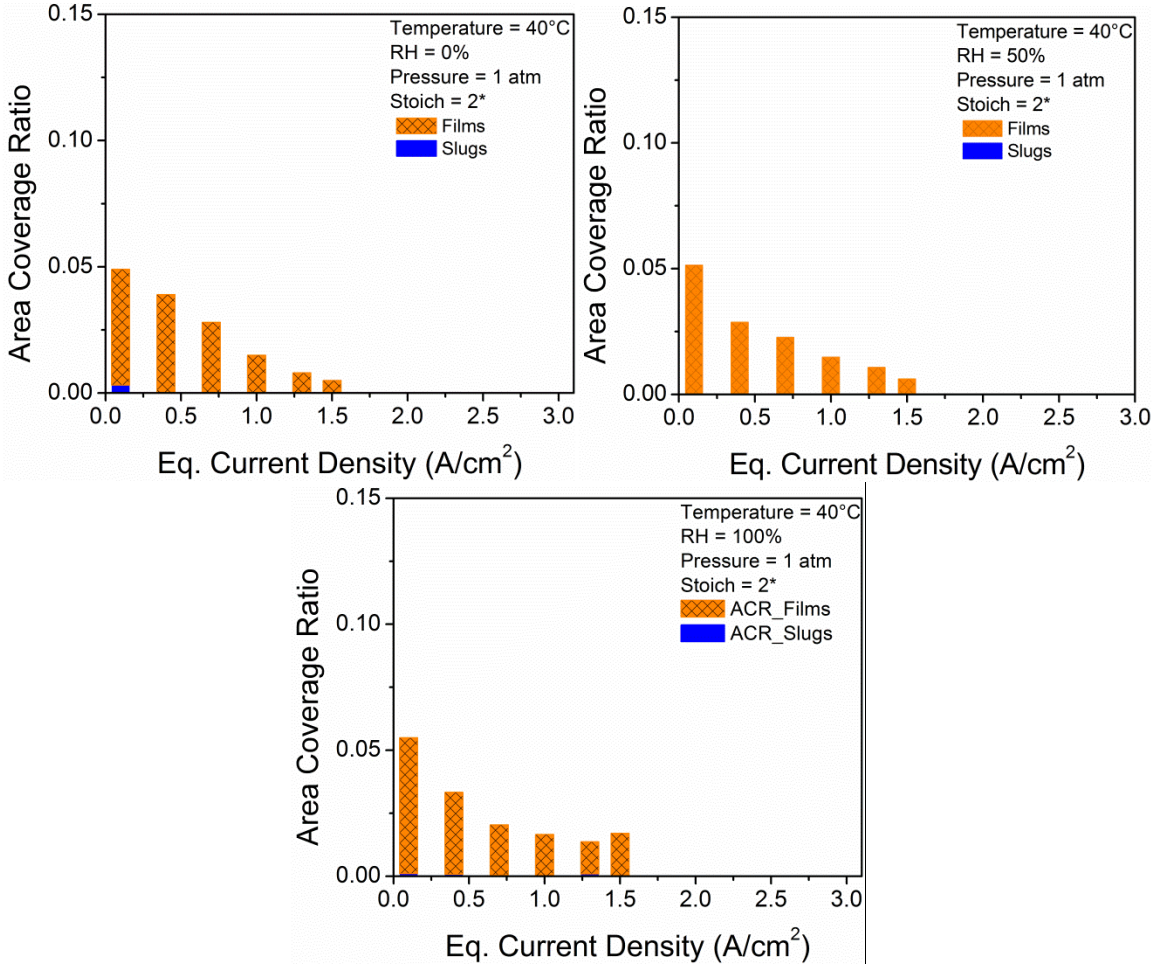

Figure 44: Flow pattern identification results for temperature of 40°C with air inlet at 0, 50 and 95% relative humidity.

Channel-to-channel Variation

It was previously established that the flow rates of individual channels vary in the case of parallel channel configuration. This leads to a variation in pressure drop in the individual channels [88]. An equivalent study in the variation of liquid water presence in the reactant channels of the PEMFC is conducted. Figure 45 shows the ratios of liquid water

detected in the individual channels. The ex-situ setup has eight channels (as described earlier) showing the variation in the liquid coverage ratios. The figure has six plots for six different flow rate conditions mapped to equivalent current densities of 0.1 to 1.5 A/cm^2. From these plots, we note that all of the channels have water being detected at different levels. There is no particular trend observed in the channel-to-channel variation of liquid water coverage of the reactant channels. Certain channels show more water detection at the lower current densities, while others show greater water detection at the higher current densities.

The lack of a definite trend indicates that the water being detected is based on the different channels to which the GDL is feeding water. It has been established by Lu et al. [147] that GDL with MPL have intermittent drainage characteristics which result in established flow paths through the GDL. Therefore water enters the same channel repeatedly. However, no particular characteristics can be seen in the channels. This indicates that there is no evidence of any of the channels having a biased presence or absence of liquid water.

These results are encouraging, as they indicate that the results are valid for flow fields with many more channels than tested here. The results would hold true even if more channels were introduced into the flow field. There would be no bias in the manner in which water enters any of the channels, regardless of the location at which they are. Therefore the results can also be used in the in-situ setup discussed earlier, with 22 channels or the full scale flow fields shown in Figure 12.

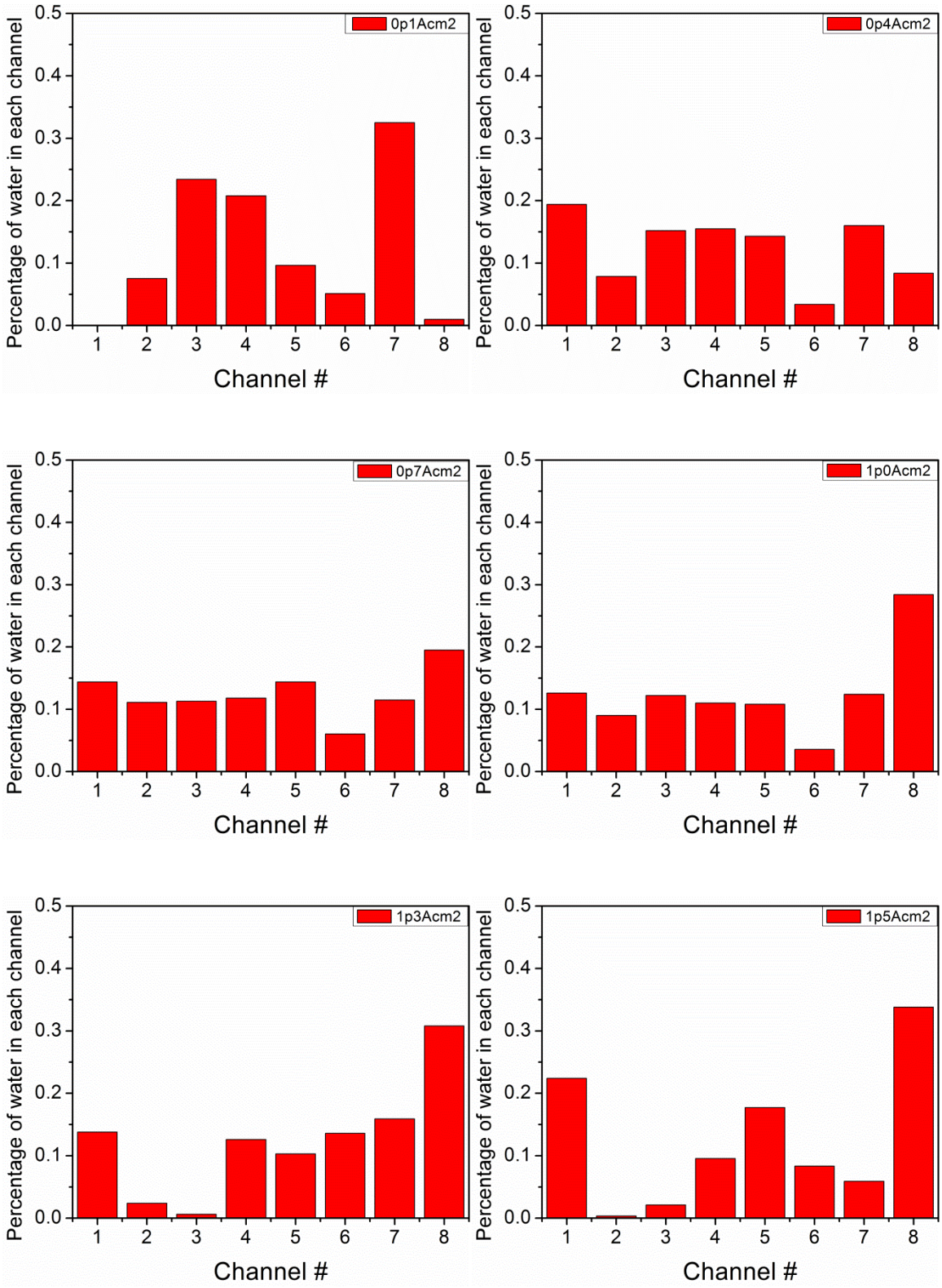

Figure 45: Channel-to-channel variation in the liquid water area coverage for 6 different current densities, at ambient temperatures.

Effect of Temperature

Although results of both the area coverage ratio and the flow pattern identification have been shown at both ambient temperatures and 40°C, there has been no direct discussion on the impact of temperature on the results. This section brings focus to the effect of temperature on the liquid water present in the reactant channels.

Figure 46 shows the ACR and the dominant flow patterns at three different temperatures of 23, 40 and 60°C. For investigating the effect of temperature, the inlet relative humidity of the inlet gases has been held constant at 0% RH (dry inlet gases). It can be observed that with the increase in temperature, the ACR decreases consistently. By 60°C, there is an insignificant quantity of water being detected, as the scale on the 60°C plot is an order of magnitude lower than the scale for the lower temperatures. Thus, it is safe to assume that the quantity of water residing in the channels at 80°C are even lower and therefore experiments have not been conducted at temperatures higher than 60°C.

The decrease in ACR is expected with increase in temperature. With increase in temperature, the saturation pressure of water in air increases too, as seen in Figure 11. Therefore, the majority of the water generated is transported in the vapor phase. The liquid water present in the reactant channels is not enough to leave a large enough ACR footprint.

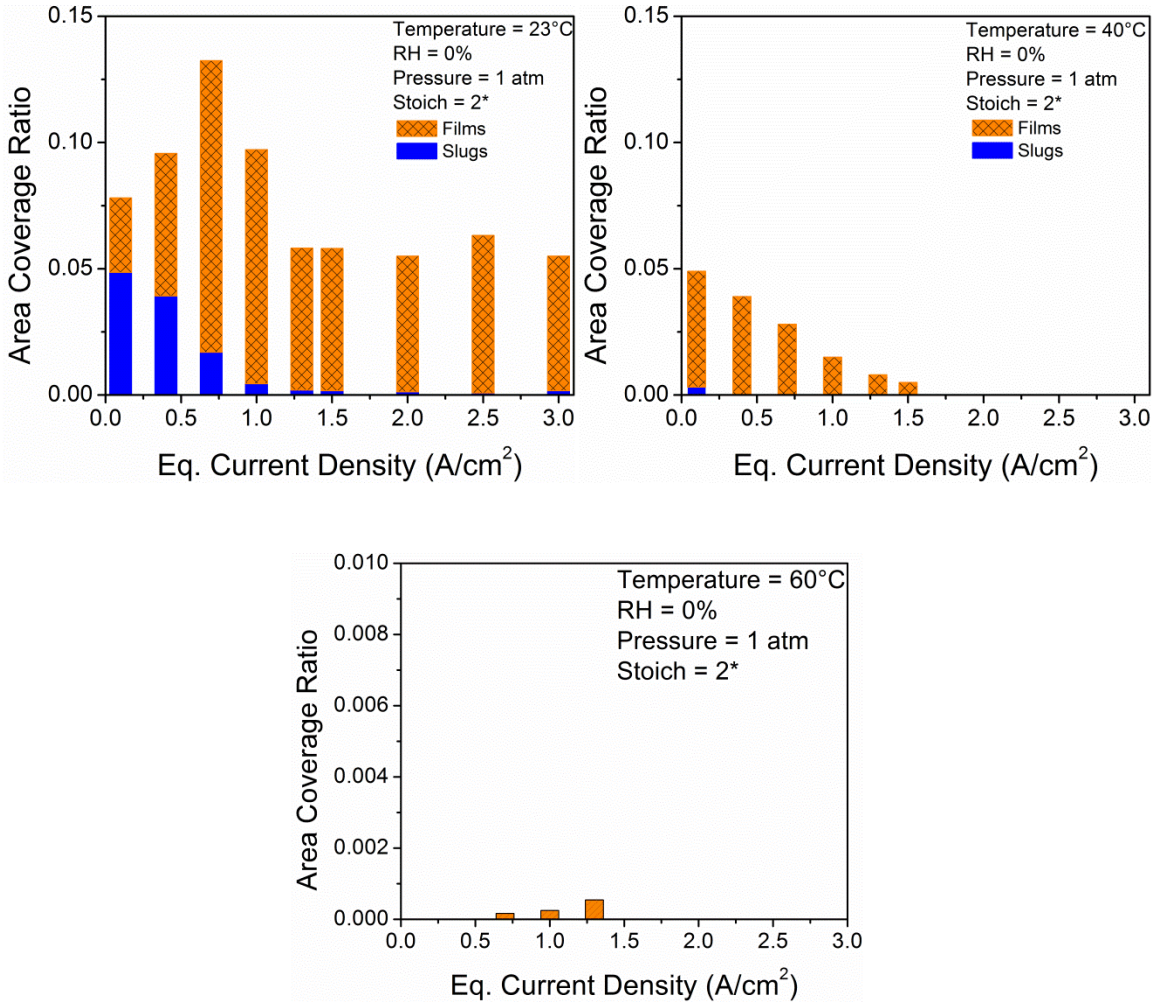

Figure 46: Effect of temperature on the ACR and flow pattern identification.

Effect of Inlet Relative Humidity

For investigating the effect of inlet RH of the reacting gases, the temperature is held constant at 40°C, while the ACR and the dominant flow pattern is reported as a function of increasing inlet RH.

Figure 44 shows the results for 40°C with the three inlet RH values of 0, 50 and 100%. With increasing RH, there is no significant effect on the ACR or the dominant flow

pattern. As discussed earlier, as the temperature increases to 40°C and beyond, the dominant flow pattern is film flow. The ACR increases very slightly for the case of fully humidified inlet gases. Therefore, it can be concluded that the inlet RH does not play a key role in the ACR detected. With increasing inlet RH, the total mass of air flowing through the channels also increases, resulting in an increase in the air velocity. The higher velocity results in lower ACR and improved efficiency of water removal. This factor results in the insignificant change in ACR with increase in inlet RH.

4.5. Area Coverage Ratio Correlation

The results discussed in the previous section describe the ACR obtained experimentally using the ex situ setup and the image processing algorithm discussed earlier. It is clearly shown that the two key parameters which dictate the ACR are the current density of operation and the temperature. Both these parameters have a direct impact on the gas flow velocity, with the current density directly impacting the mass of air that needs to flow through the reactant channels for stable operation. The temperature impacts the gas flow velocity through the change in density of the gases with change in temperature. The increase mass of water in the flow stream at the higher humidity values also increases the gas flow velocities in the reactant channels.

The temperature of the ex-situ setup dictates the saturation pressure of water in air. The saturation pressure of water increases exponentially with temperature and can be expressed as a polynomial between the temperatures of 15°C and 100°C (equation 6).

A correlation is proposed based on the experimental data obtained in this study. As discussed, the two major factors playing a key role in predicting the ACR would be the gas superficial velocity and the temperature. A new parameter K is defined to take the two parameters into consideration. The change in temperature of the cell effects the saturation pressure of water in the gases and therefore dictates how much of the water can be removed in the vapor phase. Thus, the effect of temperature is considered by using the saturation pressure. Equation 19 below defines the parameter K, as the product of the gas superficial velocity (u) and the saturation pressure P_{sat}.

$$K = u * P_{sat} \tag{19}$$

The superficial velocity u is measured in m/s, while the saturation pressure P_{sat} is measured in kPa. The following correlation is proposed to predict the Area Coverage Ratio for given operating conditions.

$$ACR = a * \exp(b * K) \tag{20}$$

where, a = 0.07876 and b = -0.005655, constants based on the operating conditions.

Figure 47 shows the comparison of the predicted and experimental ACR plotted against the parameter K, defined in equation 19. The difference between the prediction and experimental ACR is found to be less than 20% over the entire range. This difference takes into consideration 63 unique data points tested as part of this investigation.

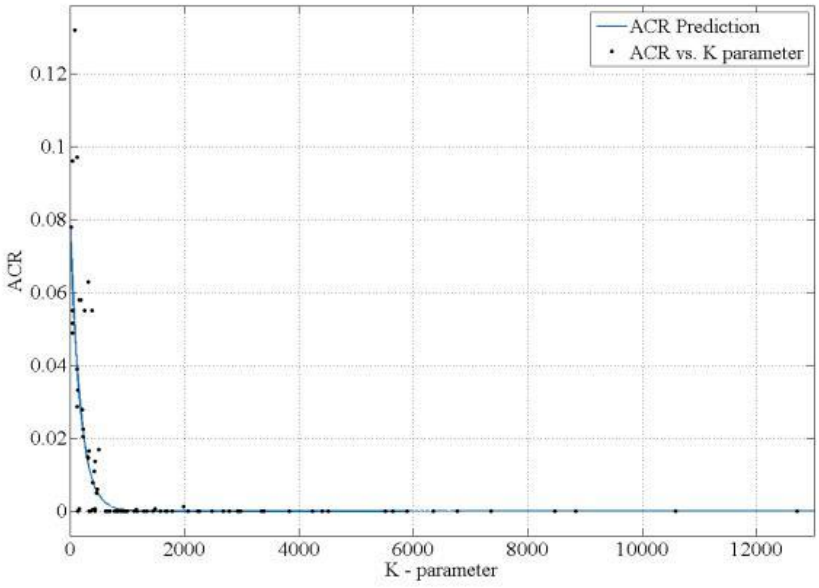

Figure 47: Comparison of predicted and experimental ACR for the entire data set with 60 unique data points.

The correlation developed here is an empirical relationship fitted to the experimental data. An analytical relationship between the fuel cell operating conditions and the area coverage ratio would have been better suited for understanding the physics behind the two-phase flow. However, developing an analytical relationship for the two-phase flow dynamics has been a complicated task with the various factors to be accounted for.

As discussed in section 2.2 (Two-phase flow in PEM fuel cell reactant channels), although different modeling efforts have focused on developing models for the two-phase flow in PEMFC reactant channels, the unique nature of these channels make them unsuitable for two-phase flow pressure drop relationships.

4.6.Summary of Visual Quantification Results

This chapter of this dissertation investigated the presence of liquid water in the reactant channels of PEMFCs. An ex-situ setup was used to visualize the two-phase flow interaction between the water generated in the PEMFC and the reacting gases flowing in the reactant channels. Three algorithms were developed and implemented to obtain the results. The liquid water present in the reactant channels was quantified as the area coverage ratio (ACR) and the dominant flow patterns were also found. The findings from this section are summarized here.

i) The ACR was determined for a range of flow and temperature conditions. The ACR was found to decrease at the higher current densities. This was attributed to the increased air velocities associated with the higher current densities.

ii) The ACR detected was then classified into slug and film dominated flows. Low current densities at ambient temperature were dominated by slug flow. Higher temperature and higher current densities promoted film flow in the channels.

iii) The variation of the ACR between the different channels was found to be insignificant. Each of the flow channels receives water without any bias towards or against any of the channels. However, it is evident that there is a variation between the channels which changes with the flow conditions. This also indicates that the results from this investigation can directly be applied to flow fields with significantly more channels without any bias.

iv) With increasing temperature, the ACR decreases drastically, and beyond 60°C, there is no significant quantity of liquid water present in the channels.

v) Inlet relative humidity does not seem to have any significant impact on the ACR in these studies.

vi) A correlation has been built for predicting the ACR for different operating conditions. The ACR is seen to have an inverse relationship with a parameter K, which is the product of the superficial gas velocity and the saturation pressure of water in air at the operating temperature.

5. Two-Phase Transient Behavior

For the successful implementation of PEMFCs in automotive drivetrains, the transient behavior of PEMFCs needs to be understood. The current work investigates the transient behavior of two-phase flow in the reactant channels using pressure drop as the characteristic parameter. The voltage response from the cell is used to characterize the performance. The effect of rapidly increasing and decreasing temperature on the two-phase pressure drop and the cell voltage is explored. Pressure drop responses from load changes are studied at three different temperatures. Two-phase pressure drop is compared for transient and steady state load conditions. The focus of the investigation is to obtain a better understanding of the two-phase flow behavior during transient operation of the PEMFC. The first part of this study focuses on identifying the factors such as transient temperature changes and transient load changes that impact the two-phase behavior in the PEMFC and can influence the cell performance. The study then delves into a parametric study to quantify the impact that different transient changes have on the two-phase flow behavior in the PEMFC reactant channels. The findings presented in this section have been presented at the Electrochemical Societies' 224th Meeting in San Francisco[148] and at the International Conference on Nano, Micro and Minichannels (ICNMM) in Chicago (August 2014) [149]. Part of the work has been accepted for publication in the Journal of Power Sources [150]. The latter part of this study has been submitted to the International Journal of Hydrogen Energy and is currently under review [151].

5.1. Objectives of Investigating Transient Behavior

From the literature review presented in section 2.4 , it can be summarized that transient operation consumes more power than steady state operation. Temperature increases slowly with increased power generation. However, the increase in temperature is a relatively slow process and therefore introduces long periods of transient behavior. It has also been established (in chapters 3 and 4) that the two-phase behavior within PEMFCs depends on the temperature of the cell, and the quantity of liquid water within the GDL and the channels plays a key role. However, the relationship between the voltage response and the two-phase flow within the PEMFC has not been explored under transient conditions.

The current work investigates the transient behavior of two-phase flow in the reactant channels using pressure drop as the characteristic parameter. The voltage response from the cell is used to characterize the performance. The effect of rapidly increasing and decreasing temperature on the two-phase pressure drop and the cell voltage is explored. Pressure drop responses from load changes are studied at three different temperatures. Two-phase pressure drop is compared for transient and steady state load conditions. The focus of the investigation is to obtain a better understanding of the two-phase flow behavior during transient operation of the PEMFC.

The work also focuses on identifying the two-phase characteristics when the load is changed at different ramp rates and for different amplitudes (of change in load current). The amplitude of the change in load current influences the change in water generation rate and the change in air flow velocities. Additionally, the change in ramp rates measure

the rate at which the changes can be made and how they impact the two-phase characteristics.

5.2.Experimental Setup for Transient Investigation

For investigating the transient behavior of the PEMFC, it was important to use an in situ setup. The setup used in chapter 3 has been used for this segment of the work as well. Cell conditioning is done following the same method as described before. For transient testing, the cell was allowed to first reach steady state using the cell conditioning. For transient load conditions, the cell was maintained at a set temperature to isolate the effects of transient load and transient temperature. The load was increased or decreased by 20 A (0.4 A/cm^2) over set time periods of 30 seconds and 300 seconds. To obtain a linear ramp during current changes, HyAl Fuel Cell Automated Testing System (FCATS) was used. The in-line heaters for the coolant were utilized in implementing rapid increases in temperature for transient temperature study. To decrease the temperature quickly, the heat exchanger cooling unit was used.

For testing the effect of transient temperature changes, the cell temperatures, gas line temperatures, and the dew point temperature were all preset on the control units at the start of the test. The test was considered completed when the cell temperature reached the set point, usually in 900 seconds for 40°C change in temperature. The inlet relative humidity was not controlled independently, as it reached the set point based on the temperature of the inlet gases and dew point temperature, both of which respond to temperature changes at a slower rate than the cell temperature.

For conducting the parametric investigation on the two-phase flow characteristics, the test condition was allowed to stabilize for 60 minutes, after which the change in condition was made. The data collection was started 10 seconds before the change in condition and was collected for the following 60 minutes. This allowed the transient change to be completed and reach the next steady state within the data collection time.

Steady State Test Conditions

Steady state testing was done at two different current densities for each of the three temperatures. This allowed us to gather six different baseline conditions to compare with the transient conditions. Table 6 provides the conditions for steady state testing. The dew point temperature was adjusted such that the inlet relative humidity remained at 95%.

Table 6: Steady state testing conditions for comparison to transient testing.

Test #	Cell Temperature (°C)	Load (A)	Inlet RH (%)
1	40	30	95
2	40	50	95
3	60	30	95
4	60	50	95
5	80	30	95
6	80	50	95

Transient Test Conditions

Table 7 shows the transient tests that were conducted as part of this study. Tests 1 – 6 show positive and negative load changes at steady temperatures of 40°C, 60°C and 80°C. Tests 7 – 10 focus on transient temperature changes while the load is held constant at 1.0

A/cm^2. The two-phase pressure drop from the transient tests was compared with the pressure drop during the steady state conditions.

Table 7: Transient testing conditions

Test #	Cell Temperature Start (°C)	Cell Temperature End (°C)	Load Start (A)	Load End (A)
1	40	40	30	50
2	40	40	50	30
3	60	60	30	50
4	60	60	50	30
5	80	80	30	50
6	80	80	50	30
7	40	60	50	50
8	40	80	50	50
9	60	40	50	50
10	80	40	50	50

5.3. Results from Transient Investigation

This section provides the details of the results obtained from the testing at specified conditions as discussed in section 5.2. The time required for the system to return to steady state is considered as an important parameter. Results for transient load changes show the variation of cell voltage and pressure drop as a function of time. The results for transient temperature are shown in terms of voltage response and pressure drop as a function of temperature.

Temporal dependence of pressure drop in PEMFC reactant channels

Work reviewed from the literature had been discussed in Section 2. There, it was noted that the time duration for transients in the electrochemical processes are very fast (relatively less than 1 second) [131]. However, the two-phase transport within the GDL occurs over a significantly longer time frame [114]. Figure 48 shows the cathode pressure drop associated with a change in the load from 0.8 A/cm^2 (40 A) to 0.1 A/cm^2 (5 A). The system was allowed to stabilize over 2 hours, by the end of which it had reached steady state as observed in region A in Figure 48. The load was changed, and the air flow rates followed the change in load based on the stoichiometry of 2 for the cathode side (as seen by the drop in pressure). The air flow rate is much lower for the current density of 0.1 A/cm^2 , and therefore the pressure drop decreases, as seen in Region B. Region B in Figure 48 is enlarged in Figure 49 and shows that the pressure drop requires almost 2500 seconds (over 40 minutes) in returning to a new steady state value. This shows that the two-phase flow in the gas channels has a transience period of the order of several minutes to an hour.

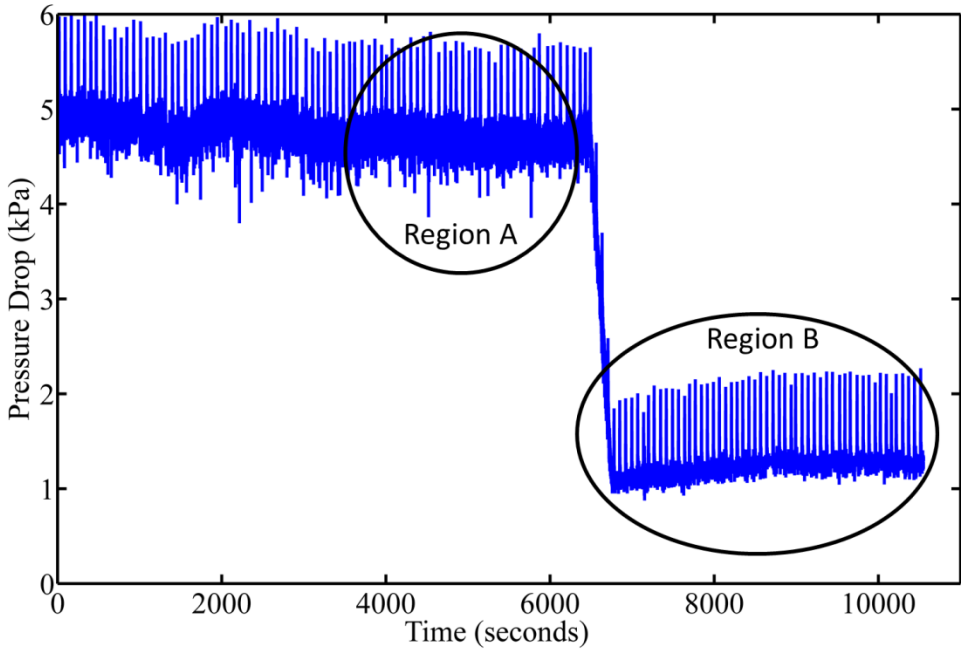

Figure 48: Time required for the pressure drop to reach steady state after a change in load on the PEMFC. Load changes from 0.8 A/cm^2 to 0.1 A/cm^2.

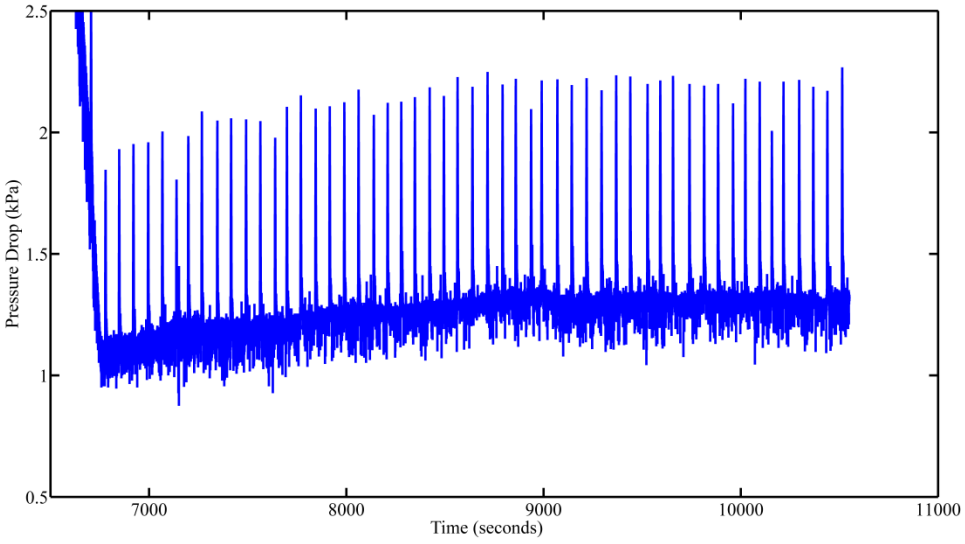

Figure 49: Region B from Figure 48. The 4000 seconds after changing of the load.

Effect of load changes on pressure drop and voltage response

Figure 50 shows the effect of increasing load on the pressure drop at three temperatures of 40°C, 60°C and 80°C. The load is increased from a current density of 0.6 A/cm^2 to 1.0 A/cm^2 over 300 seconds. It can be observed from the figure that the pressure drop response at the higher temperature is much steeper. At 40°C, the pressure drop remains high throughout as there is more liquid water present in the channels. The two-phase component keeps the pressure drop high in the channels. At 60°C, the saturation pressure is much higher; therefore little liquid water is left in the channels. Thus the pressure drop is significantly lower in the case of 60°C compared to that at 40°C. Table 2 shows the water vapor uptake into the gas stream at 40°C, 60°C and 80°C with an inlet relative humidity of 95% for each case. At a temperature of 80°C, over 8% of the water produced can be removed in the vapor stream even with the 95% inlet RH, compared to less than one percent at the lower temperature of 40°C. At 80°C, for the lower current density of 0.6 A/cm^2, the pressure drop is slightly higher than that at 60°C because of lower density and greater mass of water vapor being carried in the gas stream. At the higher current density of 1.0 A/cm^2, the pressure drop rises more rapidly. It can be observed that the pressure drop response from the change in load is steeper at the higher temperatures. At the lower temperature, there is more liquid water present in the channels as shown in a previous work [140], and therefore the pressure drop is higher. Following the flow pattern study conducted earlier by the authors, at the lower current density, there is a larger contribution of slug flow towards the liquid water in the channels, whereas with increase in the current density, the flow is dominated by film flow [32,64,140].

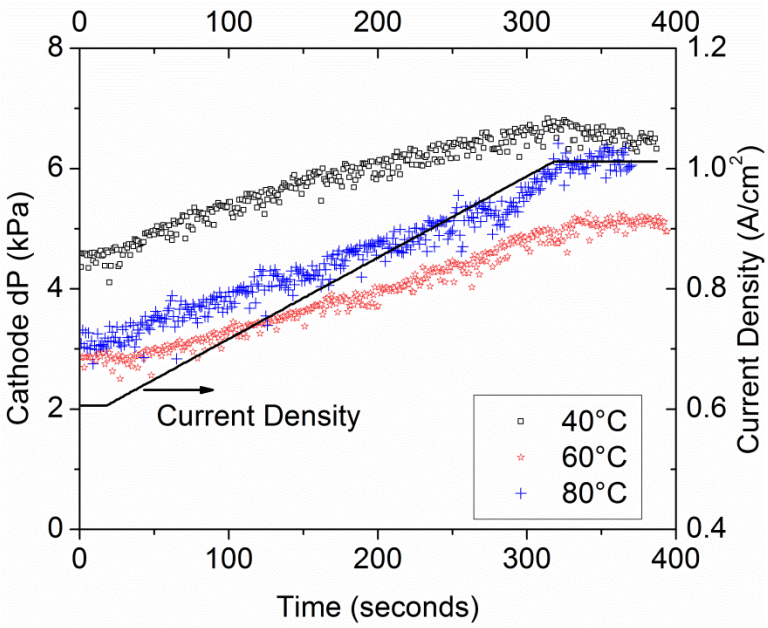

Figure 50: Effect of increasing load changes on pressure drop for the temperatures of 40°C, 60°C and 80°C as the current density is changed from 0.6 A/cm^2 to 1.0 A/cm^2.

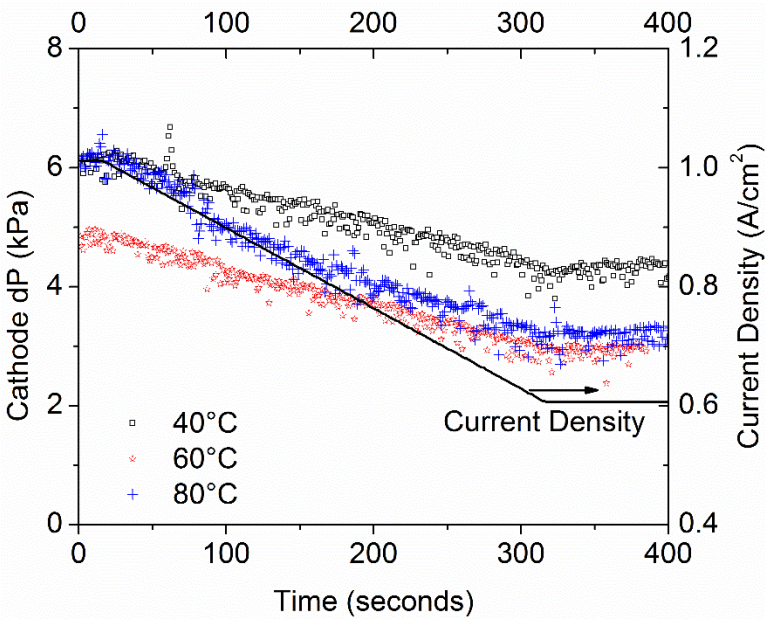

Figure 51: Effect of decreasing load changes on pressure drop for the temperatures of 40°C, 60°C and 80°C as the current density is changed from 0.6 A/cm^2 to 1.0 A/cm^2.

Figure 51 shows the effect of decreasing load on pressure drop at the same temperatures. The load is decreased from 1.0 A/cm^2 to 0.6 A/cm^2 over a period of 300 seconds. As seen in Figure 50, the change in pressure drop is steeper in the case of 80°C compared to 40°C. Although the pressure drop at the start of the test (at 1.0 A/cm^2) is very similar for both the temperatures, the pressure drop at the end of the test is much higher in the case of 40°C compared to 80°C. This again can be attributed to the increased quantity of liquid water at the lower temperatures, compared to that at higher temperatures, where most of the water is in vapor phase due to the higher saturation pressure of water at 80°C. It is seen that 60°C is the optimal condition (among the tests conducted) for the fuel cell with the lowest pressure drop, and smooth transition when the load is changed.

Thus, decreasing load at the lower temperatures does not decrease the pressure drop significantly and results in buildup of liquid water within the channels. Therefore, if possible, systems should strive to reduce transient load changes at lower operating temperatures (below 40°C). However, at the higher temperatures, the pressure drop follows rapidly with the reduction in load. Transient load changes at the higher temperatures are not as serious a concern.

Effect of temperature changes on pressure drop and voltage response

In this section, the rapid increase and decrease of temperature on the pressure drop and the cell voltage is discussed. An increase / decrease is classified as rapid if it is at a faster rate than the rate at which the dew point temperatures are changing, resulting in changes in the relative humidity.

Figure 52 shows the effect of increasing temperature on the pressure drop and the voltage response of the cell. The load is held constant at 1.0 A/cm^2. Therefore, there is no change in air flow or cell voltage due to the change in load current. In Figure 52, the temperature was increased from 40°C to 60°C. From the figure, it can be observed that the voltage response improves with increase in temperature from 40°C to 60°C. This improvement in voltage response is attributed to the reduced water flooding in the channels. Reduced water in the reactant channels reduces transport resistance and increases interfacial area available for the transport of reactants to the catalyst layer. The kinetics of reactant transport also improves with increase in the temperature. The pressure drop decreases with increase in temperature to 60°C as the saturation pressure increases, and more of the water is transported in vapor phase. This causes the two-phase contribution to decrease and the pressure drop is dictated by the single phase flow characteristics.

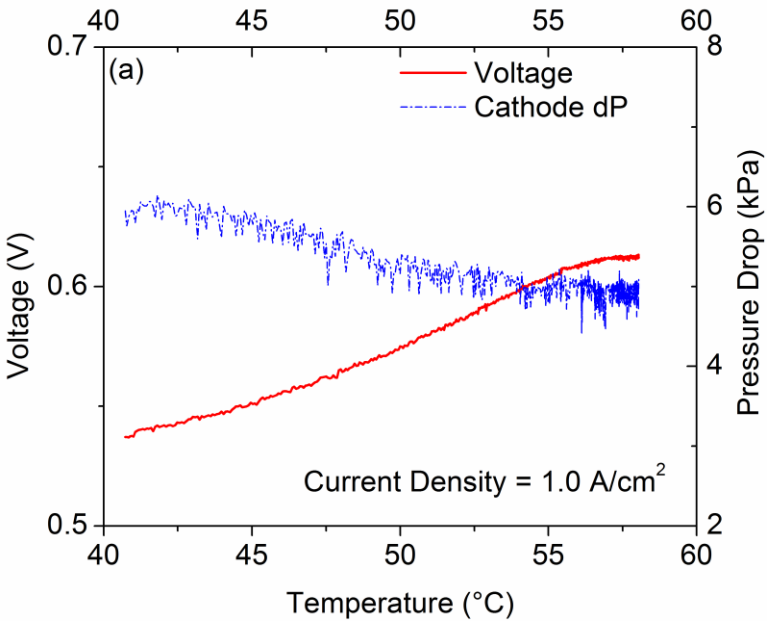

Figure 52: Effect of increasing temperature on the voltage response and the two-phase pressure drop in the channels, cell temperature increases from 40°C to 60°C.

In **Figure 53**, temperature was increased from 40°C to 80°C. In the first few seconds, as the temperature increases to 55°C, the cell voltage increases. Beyond this point, as the temperature continues to rise up towards 80°C, the voltage begins to decrease. This can be attributed to the rapid increase in temperature, which results in the drying of the membrane. The decrease in voltage is supplemented by sudden fluctuations. These fluctuations indicate flooding conditions and unstable cell behavior. As the cell temperature increases, the GDL begins to dry out followed by the membrane, resulting in a higher proton resistance and therefore a lower cell voltage. The pressure drop begins to increase due to the increase in the single phase pressure drop as the density decreases with increased temperature. This results in a higher flow velocity. Additionally, membrane dry out results in an increase in pressure drop as shown by See [37]. As the investigation is focused on the transient effects, the dew point temperature is changed at the same time as the cell temperature, but the response time of the dew point heater is slow and therefore cannot match the increase in cell temperature. Thus, the relative humidity of the inlet stream also decreases with increasing temperature, further leading to the drying of the membrane.

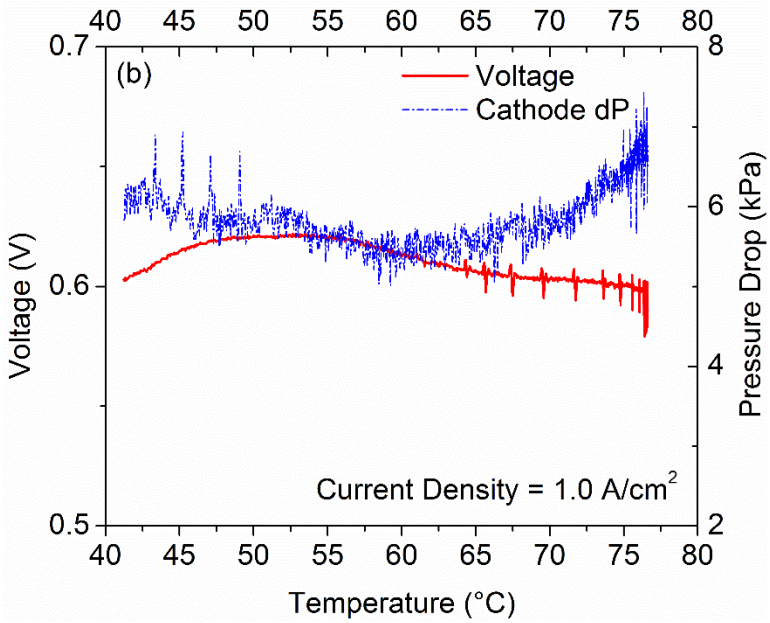

Figure 53: Effect of increasing temperature on the voltage response and the two-phase pressure drop in the channels, cell temperature increases from 40°C to 80°C.

Figure 54 shows the effect of decreasing temperature on the pressure drop and the voltage response of the cell at a constant current density of 1.0 A/cm^2. In the test represented in Figure 54, temperature is decreased from 80°C to 40°C in less than 15 minutes. The cell voltage remains steady until 60°C, beyond which it drops off. The pressure drop begins to decrease at the start of the test due to the increase in density of the gases resulting in lower gas velocities. However, after the initial dip, the pressure drop remains steady. The decrease in voltage and the steady pressure drop are explained by an increase in liquid water in the channels. The rapidly decreasing temperature increases condensation within the channels, resulting in an increased pressure drop and a higher mass transport resistance.

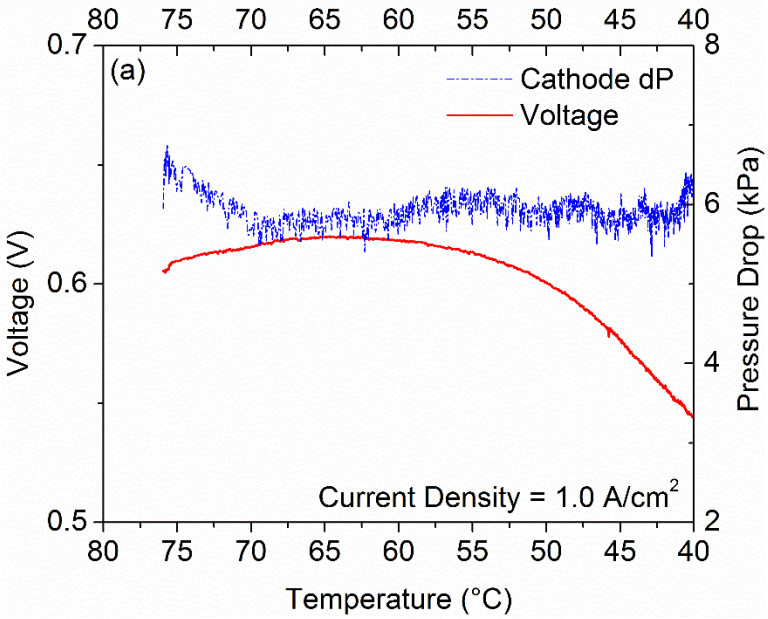

Figure 54: Effect of decreasing cell temperature on the voltage response and the two-phase pressure drop in the channels, (a) cell temperature decreases from 80°C to 40°C.

In Figure 55, when the temperature is decreased from 75°C to 55°C, the drop in temperature is smaller and therefore results in almost no change in cell voltage and a very small decrease in pressure drop. Therefore, reducing temperature rapidly to 55°C does not result in increased liquid water in the channels. The main concern with decreasing temperature rapidly is seen as temperature falls below 55°C.

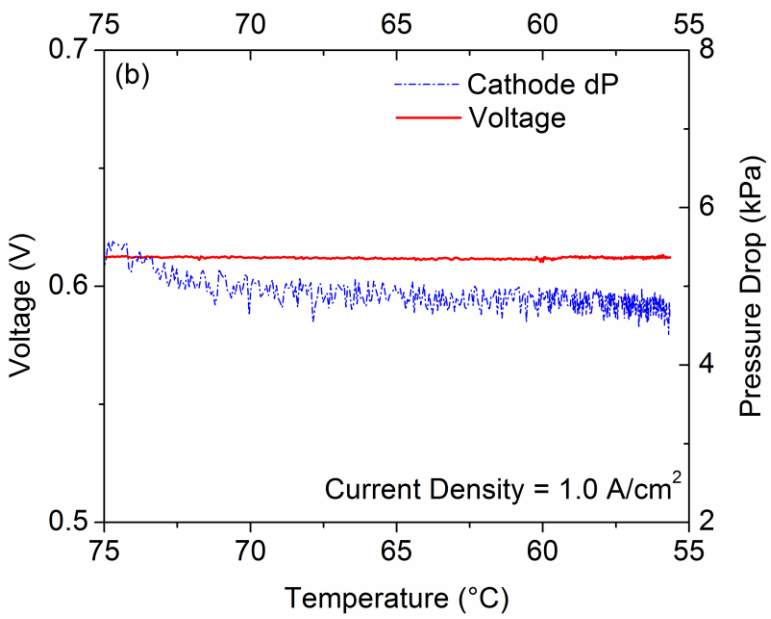

Figure 55: Effect of decreasing cell temperature on the voltage response and the two-phase pressure drop in the channels, (a) cell temperature decreases from 75°C to 55°C.

Identification of two-phase pressure drop overshoot / undershoot behavior

During the above discussed test routines, it was observed that the two-phase pressure drop does not reach the steady state value directly and goes through an overshoot when the current density is increased. Figure 56 shows the cathode manifold – to – manifold pressure drop recorded as a function of time for a sample case. For this case, the load was changed by 0.2 A/cm^2 (10 A) at a rate of 0.1 A/s. The cell temperature and gas temperature were maintained at 40°C, while the dew point temperature was kept at 30°C. The pressure drop increases with increase in current density as the air flow increases to maintain the required stoichiometric ratio. When the load reaches the maximum value, the cathode pressure drop displays the peak and proceeds to decrease, reaching a steady state value after about 1200 seconds. The peak pressure drop (ΔP_{peak}) observed is higher than the steady state pressure drop (ΔP_{ss}) and is termed as overshoot.

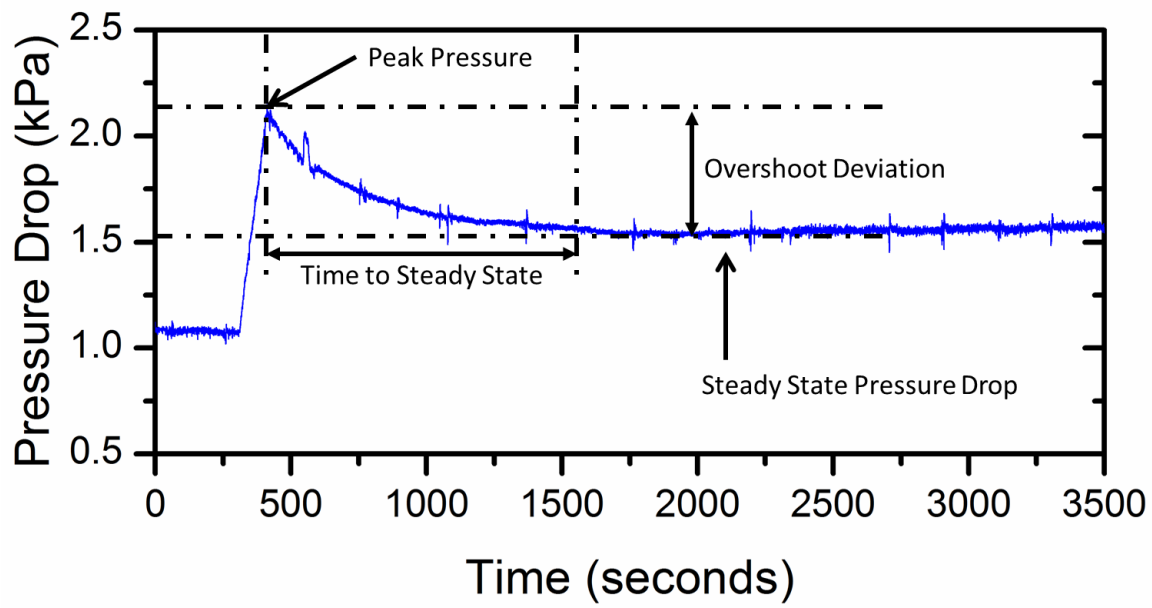

Figure 56: Two-phase pressure drop when load is increased by 0.2 A/cm^2 at a rate of 0.1 A/s and a temperature of 40°C.

Similarly, when the load is decreased by the same magnitude, the pressure drop begins to decrease as the air flow rate is decreased, reaching a minimum point when the current density has reached the target value. Beyond this point, the pressure drop begins to increase, even though the air flow rate remains constant, finally reaching a steady state value after about 500 seconds. This trough in the pressure drop reading is termed as undershoot. This can be seen in Figure 57. The magnitude of overshoot (ΔP_{MAG}) is defined as the difference between the peak pressure drop and the steady stated pressure drop, as shown in Figure 56. The magnitude of overshoot / undershoot behavior is characterized in the current work. The time required for the two-phase pressure drop to return to steady state is termed as the time to steady state (t_{ss}) and is defined as the time between the peak pressure drop and the time at which the pressure drop reaches the

steady state value. It is also shown graphically in Figure 56. The peak pressure drop is observed as the maximum value observed in the pressure drop signal. The time at steady state (t_{ss}) is obtained as the time at which the signal is within 0.1 kPa of the steady state value. The steady state value is obtained by averaging the pressure drop signal for the final ten minutes (600 seconds) of the data.

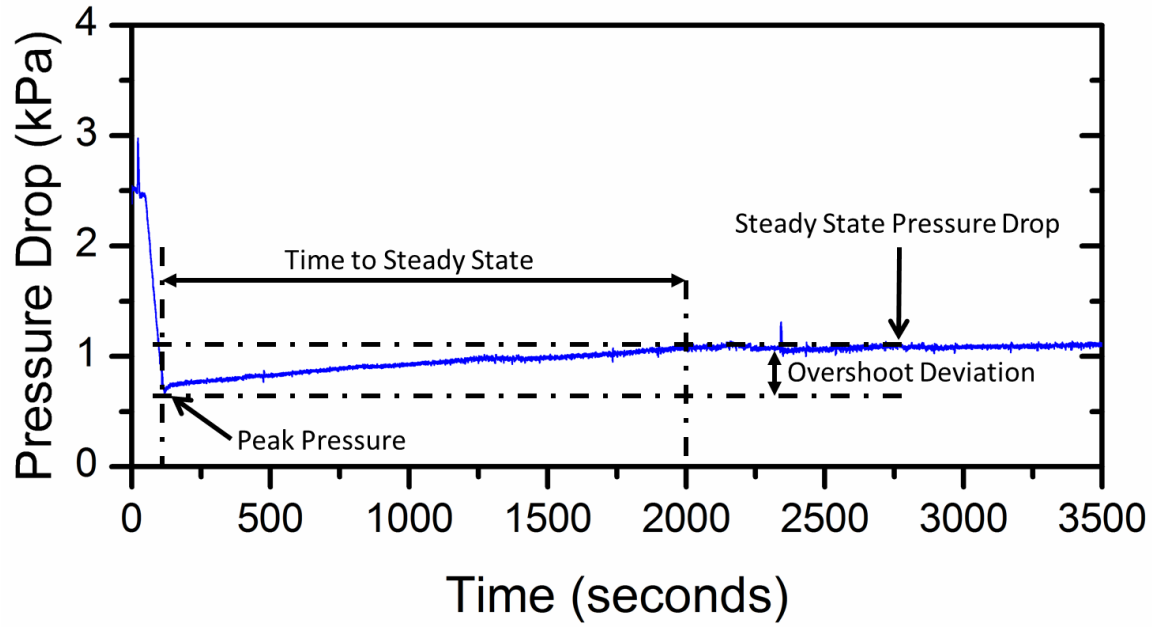

Figure 57: Two-phase pressure drop when the load current is decreased by 0.2 A/cm^2 at a rate of 0.1 A/s at a temperature of 40°C

$$\Delta P_{MAG} = \left|\Delta P_{peak} - \Delta P_{ss}\right| \tag{20}$$

Another parameter which can be used to compare the overshoot behavior is the percentage of overshoot (K_{over}). The percentage of overshoot can be defined as the ratio of magnitude of overshoot to the magnitude of the steady state pressure drop, and shown in the equation below.

$$K_{over} = \left(\frac{\Delta P_{MAG}}{\Delta P_{ss}}\right) * 100 \quad (21)$$

Although the following sections delve into the effects of temperature, ramp rate and amplitude of change on the overshoot behavior, the complete set of data from these tests is provided in Appendix 10.7. The parameters defined in this section, such as the peak pressure, the steady state pressure drop, time to steady state, magnitude of overshoot and the percentage of overshoot are all included in the data presented in the Appendix 10.7.

Effect of temperature on the overshoot behavior

Two-phase transient behavior has been studied at the higher temperatures by Wang and Wang [114]. However, the two-phase behavior in the reactant channels has not been investigated in the transient domain. The effect of temperature on the two-phase behavior has been explored and the results are presented in this section.

Table 8 shows the magnitude of overshoot / undershoot behavior observed at the temperatures of 40, 60 and 80°C when the load is changed by ±0.4 A/cm^2, at a ramp rate of 0.3 A/s. As the temperature is increased from 40°C to 60 and 80°C, no overshoot is observed and the pressure reaches a steady state within the first 10 seconds.

With increasing temperature, the magnitude of deviation decreases. Additionally, there is a decrease in the time required to reach steady state, therefore the duration of the transient behavior is decreased. With an increase in cell temperature, the saturation pressure of water in air increases exponentially, as seen in Figure 11. Therefore, there is significantly less water in the channels at the higher temperatures. This was also shown in a previous

section. Therefore, it may be concluded that increased presence of liquid water in the channels leads to longer transient durations as well as larger deviation from the steady state behavior. Wang and Wang [114] focused their investigation into two-phase transients at the higher temperatures. However, the effect is more significant at the lower temperatures, as observed here.

Table 8: Magnitude of overshoot / undershoot observed at the different temperatures, load change of 20 A (±0.4 A/cm^2) at a ramp rate of 0.3 A/s.

Change in Load (A/cm^2)	Temperature (°C)	Magnitude of Deviation (kPa)	Time to Steady State (sec)
+0.4	40	1.03	390
+0.4	60	0.00	10
+0.4	80	0.00	10
-0.4	40	0.44	1468
-0.4	60	0.20	2
-0.4	80	0.00	0

Effect of ramp rate on the overshoot behavior

The second key parameter to be investigated was the effect of ramp rate on the magnitude of overshoot and undershoot in the pressure drop signature. Figure 58 shows the effect of ramp rate on the magnitude of overshoot when the load current is increased. For two of the lower amplitudes tested, it may be noted that there is insignificant effect of the ramp rate. For the higher amplitudes tested, higher ramp rates show an increase in magnitude of overshoot. However, the effect of ramp rates may need further evaluation. The overshoot behavior currently does not show a distinct trend.

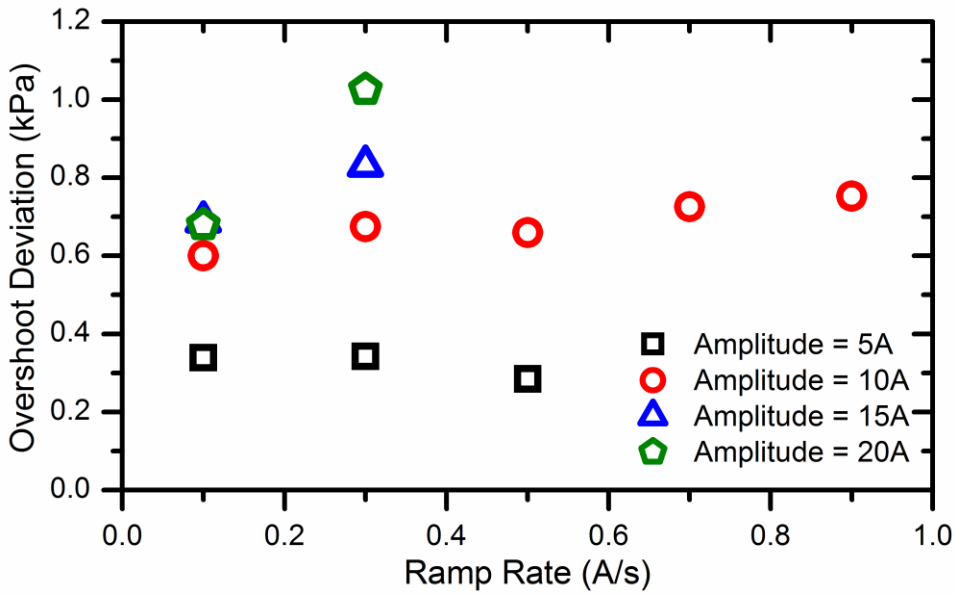

Figure 58: Effect of ramp rate on the overshoot behavior. Load is increased and the magnitude of overshoot is compared in this figure.

Figure 59 shows the effect of ramp rate on the magnitude of overshoot when the load current is decreased. The trend observed in Figure 58 is repeated in this figure. Ramp rate does not seem to have a strong effect on the magnitude of undershoot. For all four cases of amplitude it is observed that the variation as a function of ramp rates is very less. Therefore, from these two figures, it may be suggested that ramp rates do not play a key role in the magnitude of overshoot / undershoot behavior.

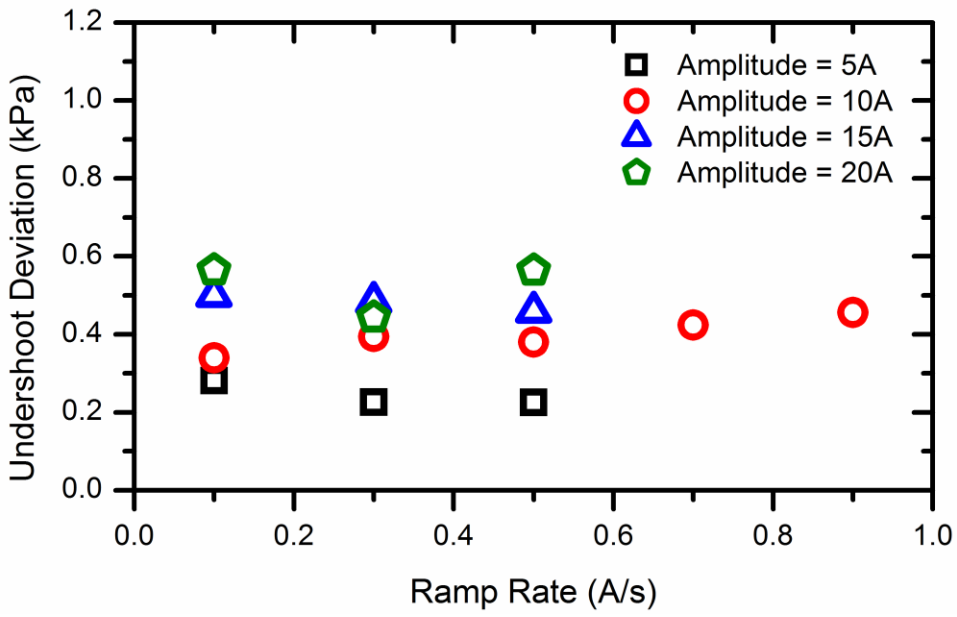

Figure 59: Effect of ramp rate on the undershoot behavior. Load is decreased and the magnitude of undershoot is compared in this figure.

Effect of amplitude of change on the overshoot behavior

The third and final parameter to be investigated was the effect of amplitude of change of load current on the magnitude of two-phase overshoot. Table 9 and 10 gives the change in load current used to investigate the effect of amplitude of change of load current. Figure 60 shows the effect of change in amplitude on the magnitude of overshoot behavior. A clear trend can be observed where the increase in amplitude of change in load current results in an increase in the magnitude of overshoot. The trend holds at all three of the ramp rates tested. The slope of increase in the magnitude of overshoot seems to be changing at the different ramp rates used. However, it is apparent that the effect of change in amplitude is to increase the magnitude of overshoot.

Table 9: Testing conditions for investigating the effect of amplitude of change of load current on the overshoot behavior.

Ramp Rate (A/s)	Amplitude of Change (A/cm^2)	Current Change (A)	Starting Current (A)	Ending Current (A)
0.1, 0.3, 0.5	0.1	5	10	15
0.1, 0.3, 0.5	0.2	10	10	20
0.1, 0.3, 0.5	0.3	15	10	25
0.1, 0.3, 0.5	0.4	20	10	30

Table 10: Testing conditions for investigating the effect of amplitude of change of load current on the undershoot behavior.

Ramp Rate (A/s)	Amplitude of Change (A/cm^2)	Current Change (A)	Starting Current (A)	Ending Current (A)
0.1, 0.3, 0.5	0.1	5	5	10
0.1, 0.3, 0.5	0.2	10	20	10
0.1, 0.3, 0.5	0.3	15	25	10
0.1, 0.3, 0.5	0.4	20	30	10

Figure 61 shows the effect of amplitude of change on the undershoot behavior. The magnitude of undershoot increases linearly with the increase in amplitude of change. The test conditions are shown in table 10 and the figure shows clearly the linear increase in the magnitude of overshoot. Therefore from these two figures in this section, it is shown that the amplitude of change in load current has a direct effect on the magnitude of overshoot / undershoot behavior.

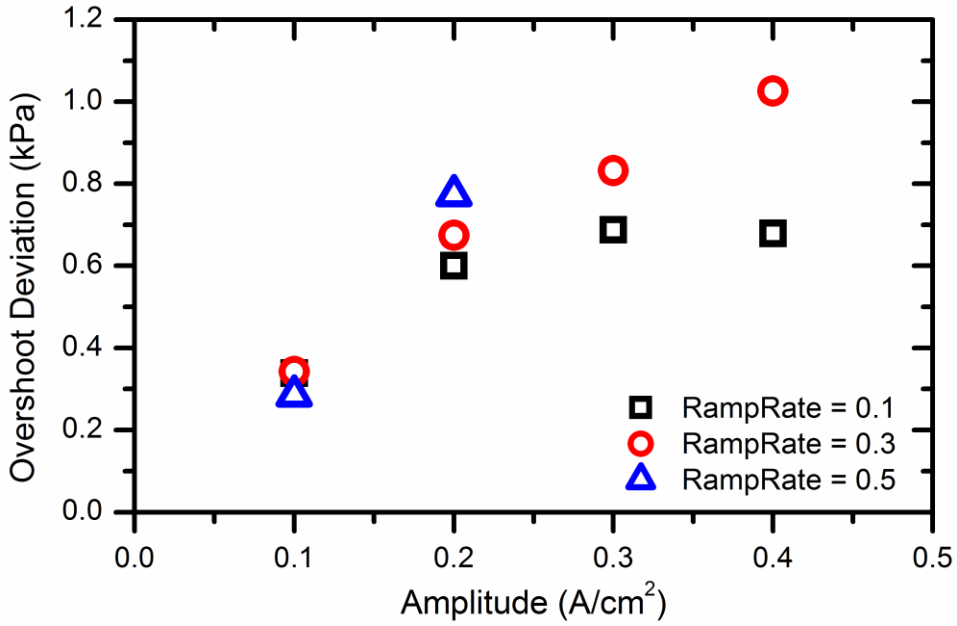

Figure 60: Effect of amplitude of change on the overshoot behavior. Load is increased and the magnitude of overshoot is compared in this figure.

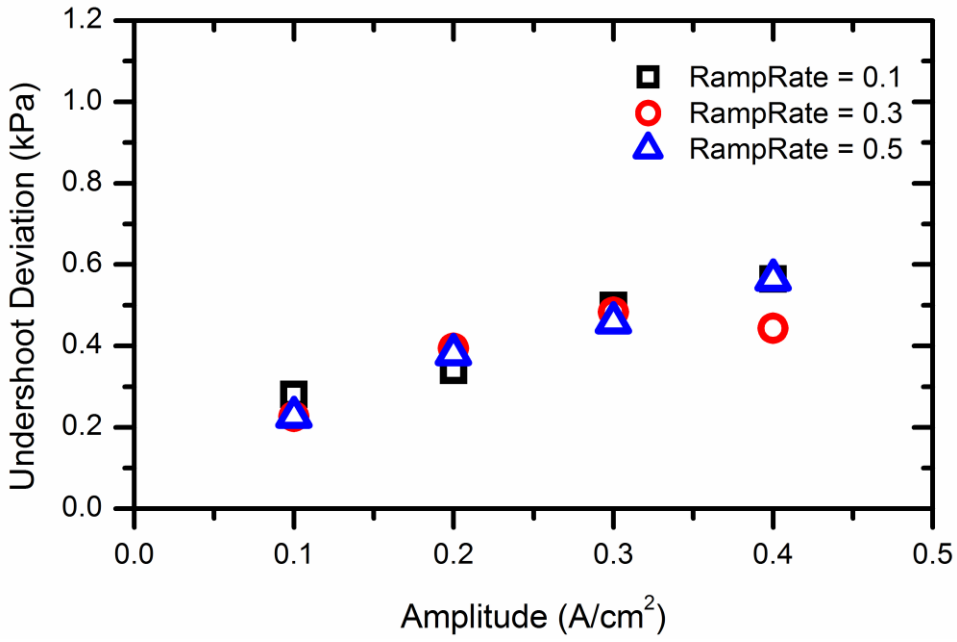

Figure 61: Effect of amplitude of change on the undershoot behavior. Load is decreased and the magnitude of undershoot is compared in this figure.

5.4. Discussion of Findings presented from the Transient Investigation

The results shown in section 5.3 are discussed in detail in this section. Transient behavior in PEMFCs has not been investigated in terms of the impact of transient changes in temperature and two-phase flow. Both these parameters can have a direct impact on the performance of the cell as they influence the saturation pressure of water in the system, and the volume of water in the system defines the area or paths available for reactant transport through the system to the reaction sites.

At first, the temporal dependence of the pressure drop in the reactant channels is investigated. It is observed that it takes about forty minutes to return to a steady state behavior. As there is a change in the operating current density, the test stand (controlling the flow rates based on reactant stoichiometric ratios) reduces the flow rate to maintain a constant stoichiometry of operation. The reduction of reactant flow reduces the gas superficial velocity and decreases the gas single phase pressure drop directly. The lower current density also means less water generation in the cell which will need to be removed. Although the current density changes quickly, it requires some time before the capillary forces remove the water from the catalyst layer and the porous GDL into the channels. Additionally, the saturation of the GDL with liquid water is a function of the air velocity in the channel, and therefore readjusts to the new air velocity. The time required for the saturation of the porous media to reach a steady value and the water from the catalyst layer to find its way out requires significant time. This is the source of this temporal dependence observed for transient changes affecting two-phase flow.

It is also observed that change in operating current density at different operating temperatures results in variation in the resulting pressure drop. At the lower temperature

(40°C), the change in pressure drop is less in magnitude compared to the change at the higher temperature (80°C). The transient change in pressure drop was less steep as the actual change in pressure drop was less at the lower temperature. The flow in the reactant channels at the lower temperatures was dominated by the liquid contribution and therefore was not affected as much with the change in air velocities. However, at the higher temperature, the contribution of liquid water to the two-phase pressure drop is significantly decreased and therefore, the single-phase gas pressure drop dominates the behavior. The single-phase pressure drop is inherently linear and the steep slope at 80°C can be attributed to the reduced contribution of liquid water to the two-phase flow in the reactant channels. The same behavior can be observed when the load is increased and when the load is decreased.

At start-up and shut-down conditions, the cell temperature is expected to change quickly. Rapidly increasing temperature improves the cell performance from 40°C to 60°C due to the reduction in liquid water in the reactant channels and the GDL. This is in agreement to the results observed in Chapter 3. The pressure drop decreases due to the reduced liquid water contribution and the cell performance increases due to the decreased reactant transport resistance. However, as the temperature continues to increase to 80°C, the membrane starts to get dehydrated due to the increased temperature and significantly higher saturation pressure. This results in the decreased performance that has been observed. The increase in pressure drop is contrary to this assumption of loss in membrane hydration. However, See [37] in his thesis shows similar behavior during membrane dry-out and shows an increase in the two-phase pressure drop observed in the reactant channels. See hypothesizes that the water from the membrane is pushed into the

channels. In a transient condition, such as here, this effect would be more pronounced and would result in an increased pressure drop, as has been observed. Therefore, it may be stated with confidence, that the increase in cell temperature should be carefully controlled and rapid rates of increase need to be avoided.

In the instance of the temperature decreasing rapidly, it is observed that the decrease in temperature from 80°C to 60°C has a smaller impact compared to the decrease from 60°C to 40°C. The pressure drop does not change when the temperature is decreasing. This can be attributed to the increase in liquid water in the reactant channels. As the temperature reduces, the water condenses out of the gas stream and increases the resistances, thereby keeping the pressure drop same even when the gas flow velocity continues to decrease. The sudden drop in voltage is also due to this increased resistance to mass transport.

The two-phase pressure drop shows a peak when the operating current density is increased, before settling back down to the steady state pressure drop. As the operating current density is increased, the air flow velocity increases as the volume of reactant gases being supplied increases. However, water is present in the reactant channels and therefore blocks the flow of the reactant gases. With the blockages present, the pressure drop continues to increase, until the pressure forces the water features to be removed from the channels. As more of the water leaves the channels, the pressure drop begins to decrease. With time, the new steady state is reached, where there is a new balance between the air flow rate and the water present in the reactant channels. It was observed in Chapter 4 that with increasing gas flow rates, there is different liquid water present, which needs to be reached for the pressure drop to reach steady state.

When the current density is decreased, the two-phase pressure drop decreases. It reaches a minimum point and then begins to increase, finally reaching the steady state pressure drop. This dip can be explained due to changes in the saturation of the GDL. At a higher air flow rate, the GDL would have a lower saturation. As the gas flow rate decreases, the GDL would have a higher saturation, resulting in the ability of the GDL to store more water. Therefore, in the initial few seconds, the GDL continues to store the water produced by the reaction and therefore the pressure drop continues to reduce. However, once the saturation reaches a steady value, the water begins to enter the reactant channels and the pressure increases to reach the final steady state pressure drop value.

From the pressure drop overshoot / undershoot, it becomes apparent that liquid water increases the overshoot behavior in the reactant channels. This is further reinforced by our investigation of the effect of temperature on the overshoot behavior. It was observed that overshoot behavior decreased when the temperature of the cell was increased to 60°C. As the temperature is increased, it had been observed from the findings of Chapter 4 that liquid water presence is drastically reduced in the reactant channels. With this decrease in the presence of liquid water, the two-phase pressure drop overshoot is also almost eliminated. Therefore, it seems conclusive that more liquid water in the reactant channels result in larger overshoots and larger transients. This is in contrast to the findings from literature that point to more water in the porous layers reduces the time of transience in the PEMFC operational behavior.

The ramp rate of ‘change of load’ shows no particular change in the magnitude of overshoot / undershoot deviation. This indicates that the rate of change in the load does not directly affect the two-phase pressure drop. This is encouraging as this points out that

changing load does not need to be limited by the ramp rate. Thus, frequent changes in load can be made. However, the changes would also have an impact on the temperature of the cell and the associated systems, which has not been considered in this discussion. In essence, this means that the rate at which water is introduced into the reactant channels does not have much of an impact on the two-phase pressure drop overshoot.

The effect of the amplitude of change is much more compared to the effect of ramp rate. Both the plots for the effect of amplitude of change on overshoot and undershoot show that there is a direct linear trend in the amplitude of change and the magnitude of deviation. The larger the change in load current, the larger the magnitude of overshoot that was observed. This indicates how the large change in gas flow rate and water generation directly plays into the overshoot behavior and therefore, it needs to be suggested that large changes in load current should be avoided to avoid the larger pressure drop. From these two trends, it can be suggested that short but rapid changes in the load current would be better, as rapid changes don't show any deviation from slow changes and would help to reduce the need for large changes in load current, which result in larger overshoot and more transient pumping power for the reactant supply systems. This would directly address the findings of Rabbani and Rokni [130] where they highlight the excess power consumed by the PEMFC auxiliary systems during transient operation.

However, this suggestion would be incomplete without the cautionary note that similar trends may exist in the thermal transients and those need to be scrutinized to a greater degree. This chapter seeks to explore the possible directions in which transients can affect the PEMFC performance and open new avenues of research into those directions.

A future aspect of this work would be the phenomenological modeling of the overshoot behavior in the two-phase pressure drop overshoot observed in the reactant channels. There is a time constant involved with the time water takes to emerge through the GDL from the catalyst layer. Additionally, there is a time constant involved with the change in saturation of the GDL. These two factors combined with the prediction of two-phase pressure drop modeling in PEMFC channels would be able to predict the magnitude of overshoot.

5.5. Summary of Findings from the Transient Study of PEM Fuel Cell

The effects of transient load and temperature changes on the two-phase flow behavior in the reactant channels of the PEMFC were investigated. An in situ setup was used with an in-house built fuel cell, designed to automotive specifications. Voltage response and the pressure drop in the reactant channels are used to interpret the transient behavior of the PEMFC. The following conclusions can be drawn from the current work.

I. Two-phase flow requires several minutes to return to steady state following a transient event. As automotive powertrains encounter continuously changing power demand, it is therefore a fair assumption that the two-phase flow would never achieve a steady state behavior.

II. Transient load changes are less significant above 60°C. At the higher temperatures, more water is transported in the vapor form. Therefore, there is less impact of liquid water on the pressure drop in the reactant channels. Transient behavior at the higher temperatures is not as serious a concern.

III. At the lower temperature of 40°C, decreasing loads result in a longer transient duration compared to increasing loads. This is due to the increased water presence during decreasing loads.

IV. More work needs to be done to remove the water at the lower temperature of 40°C compared to the water removal at the higher temperatures. Additionally, there is more water to be removed when the load is being decreased compared to increasing load.

V. Increasing temperature to 80°C leads to membrane dry-out and loss in fuel cell performance. With rapidly increasing cell temperature, the performance improves initially (up to 60°C) due to improved water management and lower liquid water presence in the reactant channels. However, as the cell temperature continues to increase towards 80°C, the cell performance reduces as the membrane begins to dry out. Therefore, if the cell is being heated beyond 60°C, it should be slower than done here.

VI. Decreasing temperature below 60°C leads to increased condensation and liquid water in the channels. When rapidly cooling the cell, going from 80°C to 60°C, the cell performance remains steady. As the temperature continues to decrease below 60°C, the cell performance starts to decrease. The pressure drop remains high due to increased condensation and larger quantity of liquid water held in the channels. This increases the mass transport resistance and decreases the performance.

VII. Two-phase pressure drop reaches steady state quicker at the higher temperatures. Load changes result in longer transients at the lower temperature of 40°C, with

the pressure-drop requiring more than 500 seconds in returning to a new steady state value. At 60°C, the two-phase flow reaches steady state within seconds of a load change. At the higher temperature, the transient behavior is less prominent. This can be attributed to increased vapor transport in the channels and therefore less liquid water to introduce two-phase effects.

VIII. Overshoot/undershoot is observed in the two-phase pressure drop at 40°C. Although this phenomenon has been observed in current and voltage response, it had not been reported for two-phase pressure measurements. Tendency for overshoot/undershoot reduces at the higher temperatures of 60°C and 80°C.

IX. Ramp rates of the load change do not have as much of an impact on the overshoot behavior. The total amplitude of change of load has a much more significant effect on the magnitude of overshoot. Magnitude of overshoot increases with an increase in the amplitude of change.

X. Therefore, it is safe to suggest that short rapid changes should be implemented in order to minimize the overshoot tendencies of the two-phase flow in PEMFC reactant channels.

6. Conclusions

Three sets of studies were conducted as part of this investigation. The overall objective is to obtain a better understanding of the liquid water transport in the reactant channels of PEMFCs. To begin with, the impact of liquid water on the cell performance is studied. This is followed up with a visualization study of the amount of liquid water present in the cathode reactant channels. Finally, the transient behavior of two-phase flow in the PEMFC reactant channels is investigated. Each set of investigation is summarized in the same chapter. The overall conclusions that can be drawn as part of this study are presented below:

a) Two-phase pressure drop multipliers can be directly used in the prediction of water management in the PEMFC reactant channels.
b) There is a distinct change in behavior in water management issues at 60°C. Below this temperature, issues of flooding dominate the cell, while above this temperature, membrane dry-out is the pre-dominant concern.
c) Temperature and relative humidity directly impact the saturation conditions in the PEMFC reactant channels, and therefore play a key role on the water management and cell performance.
d) Liquid water in the reactant channels can be quantified in the reactant channels using optical visualization techniques, in the form of Area Coverage Ratio (ACR).
e) The two-phase flow is dominated by film flow at the higher current densities and at the higher temperatures. Increased attention needs to be provided for future

investigations to explore the reactant transport during film flow in the reactant channels.

f) The ACR can be correlated with the superficial gas velocity in the reactant channels and the saturation pressure of water within the reactant channels.

g) Transient behavior has been given less attention, but needs to be explored further for automotive drivetrain applications.

h) Transients in temperature and operating current density also impact the two-phase flow in the reactant channels. The transient behavior of two-phase flow in the reactant channels has not been investigated in the past. The transient of two-phase flow is most important at the lower temperatures of operation, due to the large quantities of water present in the reactant channels.

i) The two-phase flow pressure drop in the reactant channels goes through an overshoot / undershoot behavior trend when the operating load current is changed. The ramp rate used to change the load does not have much effect on the magnitude of overshoot observed in the pressure drop signature. However, the magnitude of overshoot is linearly proportional to the amplitude of change of load current implemented.

7. Major Contributions

The work conducted as part of this investigation has focused on generating an improved understanding of the liquid water in the reactant channels of the PEM fuel cells. Quantitative tools are developed for predicting the effect of liquid water content on available surface area for reactant transport and gas channel pressure drop. These predictive parameters are applied in understanding the effects of temperature and load transients on the pressure drop response of gas channels. A combination of in situ and ex situ studies have been used in this investigation. The major contributions from this work are highlighted here.

i) The two-phase pressure drop multiplier has been experimentally demonstrated as a diagnostic tool for the prediction of cell flooding and membrane dehydration. A range of 1.2 to 1.5 has been suggested for the two-phase multiplier for optimized performance of PEMFCs. The two-phase multiplier is proposed as a low cost non-intrusive diagnostic tool for an operating fuel cell.

ii) The liquid water in the reactant channels has been visualized and quantified. A new parameter, Area Coverage Ratio (ACR) has been defined for the quantification of liquid water in the channels. The dominant flow patterns exhibited in fuel cell operating conditions were investigated. The variation in ACR among different channels in a multi-channel system was brought forth.

iii) The ACR is being used as an area reduction factor for the area available for the diffusive transport of gases to the reaction sites. Therefore, it is being used as an increased mass transport resistance. The data and the trends are being

used in the 1+1D modeling effort being undertaken at GM and described in section 1.6.

iv) The need to understand the transient behavior of two-phase flow in PEMFC has been highlighted. The impact of temperature and two-phase flow on the cell performance under transient conditions is highlighted.

v) Overshoot behavior in the two-phase pressure drop during transient changes in load current was observed for the first time.

8. Publications

8.1 Conference Presentations

1. See, E. J., **Banerjee, R.**, Daino, M. M., Sergi, J. M., Koz, M., Owejan, J. P., Gagliargo, J. J., and Kandlikara, S. G., "Thermal Management Considerations in the design of an Experimental Fuel Cell with Material Evaluation", Rome, Italy – 2011.
2. Kandlikar, S., See, E. J., Gopalan, P., Koz, M., and **Banerjee, R**., 2013, "Two-phase Flow in GDL and Reactant Channels of a Proton Exchange Membrane Fuel Cell," Jeju, Korea - 2013.
3. **Banerjee, R.**, See, E., and Kandlikar, S. G., 2013, "Pressure Drop and Voltage Response of PEMFC Operation under Transient Temperature and Loading Conditions," ECS Trans., 58(1), pp. 1601–1611.
4. **Banerjee, R**., and Kandlikar, S., 2014, "Two-phase pressure drop characteristics during low temperature transients in PEMFCs," Chicago, USA - 2014.

8.2 Journal Publications

1. **Banerjee, R.**, and Kandlikar, S. G., 2014, "Liquid water quantification in the cathode side gas channels of a proton exchange membrane fuel cell through two-phase flow visualization," J. Power Sources, 247, pp. 9–19.
2. Kandlikar, S. G., See, E. J., Koz, M., Gopalan, P., and **Banerjee, R.**, 2014, "Two-phase flow in GDL and reactant channels of a proton exchange membrane fuel cell," Int. J. Hydrog. Energy, 39(12), pp. 6620–6636.

3. **Banerjee, R.**, and Kandlikar, S.G., "Experimental investigation of two-phase flow pressure drop transients in polymer electrolyte membrane fuel cell reactant channels and their impact on the cell performance," J. Power Sources, 268, pp. 194 – 203.
4. **Banerjee, R.**, Mejia, V., Howe, D., and Kandlikar, S.G., "Experimental validation of two-phase pressure drop multiplier as a diagnostic tool for characterizing PEM fuel cell performance," Int. J. Hydrog. Energy, *Accepted*.
5. **Banerjee, R.**, and Kandlikar S.G., "Two-phase pressure drop response during load transients in a PEMFC", Int. J. Hydrog. Energy, *Accepted.*
6. **Banerjee, R.,** and Kandlikar, S.G., "Current status and research needs to elucidate the effects of two-phase flow and thermal transients in Proton Exchange Membrane Fuel Cells", *In Preparation.*

9. References

[1] 2013, Annual Energy Outlook 2013, United States.

[2] Hughes N., and Gnolucci P., 2012, "Hydrogen Economics and Policy," Comprehensive Renewable Energy, Sayigh, ed., Elsevier, Oxford, pp. 45 – 75.

[3] 2014, Annual Energy Outlook 2014, United States.

[4] Dunn S., 2002, "Hydrogen futures: toward a sustainable energy system," Int. J. Hydrog. Energy, **27**(3), pp. 235–264.

[5] Browne S., Neill D., and Takahashi P., 1988, "The Hawaii hydrogen from renewable energy program," Int. J. Hydrog. Energy, **13**(8), pp. 483–488.

[6] Kandlikar S. ., 2009, "Hydrogen Horizons," Mech. Eng., **131**(5), p. 4.

[7] Mench M. M., 2008, Fuel Cell Engines, John Wiley & Sons, New Jersey.

[8] 2013, Fuel Cell Technical Team Roadmap, US Drive, Michigan.

[9] Costamagna P., and Srinivasan S., 2001, "Quantum jumps in the PEMFC science and technology from the 1960s to the year 2000: Part II. Engineering, technology development and application aspects," J. Power Sources, **102**(1–2), pp. 253–269.

[10] Viel W., Lamm A., and Hubert G., 2003, Handbook of Fuel Cells - Fundamentals Technology and Applicaations, John Wiley.

[11] Spiegel C., 2007, Designing and Building Fuel Cells, Mcgraw-hill.

[12] Barbir F., 2013, PEM fuel cells: theory and practice, Elsevier/Academic Press, Amsterdam ; Boston.

[13] Kandlikar S. G., 2008, "Microscale and Macroscale Aspects of Water Management Challenges in PEM Fuel Cells," Heat Transf. Eng., **29**(7), pp. 575–587.

[14] Kandlikar S. G., and Lu Z., 2009, "Fundamental Research Needs in Combined Water and Thermal Management Within a Proton Exchange Membrane Fuel Cell Stack Under Normal and Cold-Start Conditions," J. Fuel Cell Sci. Technol., **6**(4), p. 044001.

[15] Nguyen T. V., and White R. E., 1993, "A Water and Heat Management Model for Proton-Exchange-Membrane Fuel Cells," J. Electrochem. Soc., **140**(8), pp. 2178–2186.

[16] Van Nguyen T., and Knobbe M. W., 2003, "A liquid water management strategy for PEM fuel cell stacks," J. Power Sources, **114**(1), pp. 70–79.

[17] Hui L., Yanghua T., Zhenwei W., Zheng S., Shaohong W., Datong S., Jianlu Z., Fatih K., Jiujun Z., Haijiang W., Zhongsheng L., Abouatallah R., and Mazza A., 2008, "A review of water flooding issues in the proton exchange membrane fuel cell," J. Power Sources, **178**(1), pp. 103–17.

[18] Yousfi-Steiner N., Moçotéguy P., Candusso D., Hissel D., Hernandez A., and Aslanides A., 2008, "A review on PEM voltage degradation associated with water management: Impacts, influent factors and characterization," J. Power Sources, **183**(1), pp. 260–274.

[19] Yu L., Chen W., Qin M., and Ren G., 2009, "Experimental research on water management in proton exchange membrane fuel cells," J. Power Sources, **189**(2), pp. 882–887.

[20] Kim S.-G., and Lee S.-J., 2013, “A review on experimental evaluation of water management in a polymer electrolyte fuel cell using X-ray imaging technique,” J. Power Sources, **230**, pp. 101–108.
[21] Jiao K., and Li X., “Water transport in polymer electrolyte membrane fuel cells,” Prog. Energy Combust. Sci., **In Press, Corrected Proof**.
[22] Owejan J. P., Owejan J. E., Gu W., Trabold T. A., Tighe T. W., and Mathias M. F., 2010, “Water Transport Mechanisms in PEMFC Gas Diffusion Layers,” J. Electrochem. Soc., **157**(10), pp. B1456–B1464.
[23] Zhang J., Tang Y., Song C., Xia Z., Li H., Wang H., and Zhang J., 2008, “PEM fuel cell relative humidity (RH) and its effect on performance at high temperatures,” Electrochimica Acta, **53**(16), pp. 5315–5321.
[24] Stumper J., Löhr M., and Hamada S., 2005, “Diagnostic tools for liquid water in PEM fuel cells,” J. Power Sources, **143**(1-2), pp. 150–157.
[25] Wu J., Zi Yuan X., Wang H., Blanco M., Martin J. J., and Zhang J., 2008, “Diagnostic tools in PEM fuel cell research: Part II: Physical/chemical methods,” Int. J. Hydrog. Energy, **33**(6), pp. 1747–1757.
[26] Chen J., 2010, “Dominant frequency of pressure drop signal as a novel diagnostic tool for the water removal in proton exchange membrane fuel cell flow channel,” J. Power Sources, **195**(4), pp. 1177–1181.
[27] Trabold T. A., 2005, “Minichannels in Polymer Electrolyte Membrane Fuel Cells,” Heat Transf. Eng., **26**(3), pp. 3–12.
[28] See E. J., and Kandlikar S. G., 2013, “A Two-Phase Pressure Drop Model Incorporating Local Water Balance and Reactant Consumption in PEM Fuel Cell Gas Channels,” ECS Trans., **50**(2), pp. 99–111.
[29] Grimm M., See E. J., and Kandlikar S. G., 2012, “Modeling gas flow in PEMFC channels: Part I – Flow pattern transitions and pressure drop in a simulated ex situ channel with uniform water injection through the GDL,” Int. J. Hydrog. Energy, **37**(17), pp. 12489–12503.
[30] Kandlikar S., See E. J., Gopalan P., Koz M., and Banerjee R., 2013, “Two-phase Flow in GDL and Reactant Channels of a Proton Exchange Membrane Fuel Cell,” Jeju, Korea.
[31] Triplett K. A., Ghiaasiaan S. M., Abdel-Khalik S. I., and Sadowski D. L., 1999, “Gas–liquid two-phase flow in microchannels Part I: two-phase flow patterns,” Int. J. Multiph. Flow, **25**(3), pp. 377–394.
[32] Lu Z., Kandlikar S. G., Rath C., Grimm M., Domigan W., White A. D., Hardbarger M., Owejan J. P., and Trabold T. A., 2009, “Water management studies in PEM fuel cells, Part II: Ex situ investigation of flow maldistribution, pressure drop and two-phase flow pattern in gas channels,” Int. J. Hydrog. Energy, **34**(Compendex), pp. 3445–3456.
[33] Pacheco A. F., Martins M. E. S., and Zhao H., 2013, “New European Drive Cycle (NEDC) simulation of a passenger car with a HCCI engine: Emissions and fuel consumption results,” Fuel, **111**, pp. 733–739.
[34] Tie S. F., and Tan C. W., 2013, “A review of energy sources and energy management system in electric vehicles,” Renew. Sustain. Energy Rev., **20**, pp. 82–102.

[35] Corbo P., Corcione F. E., Migliardini F., and Veneri O., 2005, "Experimental study of a fuel cell power train for road transport application," J. Power Sources, **145**(2), pp. 610–619.
[36] Uzunoglu M., and Alam M. S., 2006, "Dynamic modeling, design, and simulation of a combined PEM fuel cell and ultracapacitor system for stand-alone residential applications," Energy Convers. IEEE Trans. On, **21**(3), pp. 767–775.
[37] See E., 2013, "In situ measurement, characterization, and modeling of two-phase pressure drop incorporating local water saturation in PEMFC gas channels," Thesis.
[38] Kandlikar S. G., See E. J., Koz M., Gopalan P., and Banerjee R., 2014, "Two-phase flow in GDL and reactant channels of a proton exchange membrane fuel cell," Int. J. Hydrog. Energy, **39**(12), pp. 6620–6636.
[39] Quick, C., Ritzinger, D., Lehnert, W., and Hartnig, C., 2009, "Characterization of water transport in gas diffusion media," J. Power Sources, **190**, pp. 110 – 120.
[40] Owejan J. P., Gagliardo J. J., Sergi J. M., Kandlikar S. G., and Trabold T. A., 2009, "Water management studies in PEM fuel cells, Part I: Fuel cell design and in situ water distributions," Int. J. Hydrog. Energy, **34**(8), pp. 3436–3444.
[41] You L., and Liu H., 2006, "A two-phase flow and transport model for PEM fuel cells," J. Power Sources, **155**(2), pp. 219–230.
[42] Chen F., Chang M.-H., and Fang C.-F., 2007, "Analysis of water transport in a five-layer model of PEMFC," J. Power Sources, **164**(2), pp. 649–658.
[43] Su A., Weng F.-B., Hsu C.-Y., and Chen Y.-M., 2006, "Studies on flooding in PEM fuel cell cathode channels," Int. J. Hydrog. Energy, **31**(8), pp. 1031–1039.
[44] Nguyen T. V., 2006, "Water Management by Material Design and Engineering for PEM Fuel Cells," ECS Trans., **3**(1), pp. 1171–1180.
[45] Sergi J. M., Lu Z., and Kandlikar S. G., 2009, "In Situ Characterization of Two-Phase Flow in Cathode Channels of an Operating PEM Fuel Cell With Visual Access," ASME, pp. 303–311.
[46] Sergi J. M., and Kandlikar S. G., 2011, "Quantification and characterization of water coverage in PEMFC gas channels using simultaneous anode and cathode visualization and image processing," Int. J. Hydrog. Energy, **36**(19), pp. 12381–12392.
[47] Owejan J. P., Trabold T. A., and Mench M. M., 2014, "Oxygen transport resistance correlated to liquid water saturation in the gas diffusion layer of PEM fuel cells," Int. J. Heat Mass Transf., **71**, pp. 585–592.
[48] Ramos-Alvarado B., Sole J. D., Hernandez-Guerrero A., and Ellis M. W., 2012, "Experimental characterization of the water transport properties of PEM fuel cells diffusion media," J. Power Sources, **218**, pp. 221–232.
[49] Jang J.-H., Yan W.-M., and Shih C.-C., 2006, "Effects of the gas diffusion-layer parameters on cell performance of PEM fuel cells," J. Power Sources, **161**(1), pp. 323–332.
[50] Kandlikar S. G., and Lu Z., 2009, "Thermal management issues in a PEMFC stack–A brief review of current status," Appl. Therm. Eng., **29**(7), pp. 1276–1280.
[51] Zhang G., and Kandlikar S. G., 2012, "A critical review of cooling techniques in proton exchange membrane fuel cell stacks," Int. J. Hydrog. Energy, **37**(3), pp. 2412–2429.

[52] Hosseinzadeh E., Rokni M., Rabbani A., and Mortensen H. H., 2013, "Thermal and water management of low temperature Proton Exchange Membrane Fuel Cell in fork-lift truck power system," Appl. Energy, **104**, pp. 434–444.
[53] Dai W., Wang H., Yuan X.-Z., Martin J. J., Yang D., Qiao J., and Ma J., 2009, "A review on water balance in the membrane electrode assembly of proton exchange membrane fuel cells," Int. J. Hydrog. Energy, **34**(23), pp. 9461 – 9478.
[54] Carnes B., and Djilali N., 2006, "Analysis of coupled proton and water transport in a PEM fuel cell using the binary friction membrane model," Electrochimica Acta, **52**(3), pp. 1038–1052.
[55] Amirinejad M., Rowshanzamir S., and Eikani M. H., 2006, "Effects of operating parameters on performance of a proton exchange membrane fuel cell," J. Power Sources, **161**(2), pp. 872–875.
[56] Yan W.-M., Chen C.-Y., Mei S.-C., Soong C.-Y., and Chen F., 2006, "Effects of operating conditions on cell performance of PEM fuel cells with conventional or interdigitated flow field," J. Power Sources, **162**(2), pp. 1157–1164.
[57] Yan Q., Toghiani H., and Causey H., 2006, "Steady state and dynamic performance of proton exchange membrane fuel cells (PEMFCs) under various operating conditions and load changes," J. Power Sources, **161**(1), pp. 492–502.
[58] Wang L., Husar A., Zhou T., and Liu H., 2003, "A parametric study of PEM fuel cell performances," Int. J. Hydrog. Energy, **28**(11), pp. 1263–1272.
[59] Zhang J., Tang Y., Song C., Cheng X., Zhang J., and Wang H., 2007, "PEM fuel cells operated at 0% relative humidity in the temperature range of 23–120°C," Electrochimica Acta, **52**(15), pp. 5095–5101.
[60] Coppo M., Siegel N. P., and Spakovsky M. R. von, 2006, "On the influence of temperature on PEM fuel cell operation," J. Power Sources, **159**(1), pp. 560–569.
[61] Tohidi M., Mansouri S. H., and Amiri H., 2010, "Effect of primary parameters on the performance of PEM fuel cell," Int. J. Hydrog. Energy, **35**(17), pp. 9338–9348.
[62] Kim S., and Hong I., 2008, "Effects of humidity and temperature on a proton exchange membrane fuel cell (PEMFC) stack," J. Ind. Eng. Chem., **14**(3), pp. 357–364.
[63] Saleh M. M., Okajima T., Hayase M., Kitamura F., and Ohsaka T., 2007, "Exploring the effects of symmetrical and asymmetrical relative humidity on the performance of H2/air PEM fuel cell at different temperatures," J. Power Sources, **164**(2), pp. 503–509.
[64] Lu Z., Rath C., Zhang G., and Kandlikar S. G., 2011, "Water management studies in PEM fuel cells, part IV: Effects of channel surface wettability, geometry and orientation on the two-phase flow in parallel gas channels," Int. J. Hydrog. Energy, **36**(16), pp. 9864–9875.
[65] Anderson R., Zhang L., Ding Y., Blanco M., Bi X., and Wilkinson D. P., 2010, "A critical review of two-phase flow in gas flow channels of proton exchange membrane fuel cells," J. Power Sources, **195**(15), pp. 4531–4553.
[66] He W., Lin G., and Van Nguyen T., 2003, "Diagnostic tool to detect electrode flooding in proton-exchange-membrane fuel cells," AIChE J., **49**(12), pp. 3221–3228.
[67] Chen J., and Zhou B., 2008, "Diagnosis of PEM fuel cell stack dynamic behaviors," J. Power Sources, **177**(1), pp. 83–95.

[68] Wu J., Yuan X. Z., Wang H., Blanco M., Martin J. J., and Zhang J., 2008, "Diagnostic tools in PEM fuel cell research: Part I Electrochemical techniques," Int. J. Hydrog. Energy, **33**(6), pp. 1735–1746.
[69] Daino M. M., and Kandlikar S. G., 2009, "Evaluation of Imaging Techniques Applied to Water Management Research in PEMFCs," ASME, pp. 467–479.
[70] Bazylak A., 2009, "Liquid water visualization in PEM fuel cells: A review," Int. J. Hydrog. Energy, **34**(9), pp. 3845–3857.
[71] Kramer D., Zhang J., Shimoi R., Lehmann E., Wokaun A., Shinohara K., and Scherer G. G., 2005, "In situ diagnostic of two-phase flow phenomena in polymer electrolyte fuel cells by neutron imaging: Part A. Experimental, data treatment, and quantification," Electrochimica Acta, **50**(13), pp. 2603–2614.
[72] Owejan J. P., Trabold T. A., Jacobson D. L., Arif M., and Kandlikar S. G., 2007, "Effects of flow field and diffusion layer properties on water accumulation in a PEM fuel cell," Int. J. Hydrog. Energy, **32**(17), pp. 4489–4502.
[73] Boillat P., Kramer D., Seyfang B. C., Frei G., Lehmann E., Scherer G. G., Wokaun A., Ichikawa Y., Tasaki Y., and Shinohara K., 2008, "In situ observation of the water distribution across a PEFC using high resolution neutron radiography," Electrochem. Commun., **10**(4), pp. 546–550.
[74] Trabold T. A., Owejan J. P., Jacobson D. L., Arif M., and Huffman P. R., 2006, "In situ investigation of water transport in an operating PEM fuel cell using neutron radiography: Part 1 – Experimental method and serpentine flow field results," Int. J. Heat Mass Transf., **49**(25–26), pp. 4712–4720.
[75] Geiger A. b., Tsukada A., Lehmann E., Vontobel P., Wokaun A., and Scherer G. g., 2002, "In Situ Investigation of Two-Phase Flow Patterns in Flow Fields of PEFC's Using Neutron Radiography," Fuel Cells, **2**(2), pp. 92–98.
[76] Satija R., Jacobson D. L., Arif M., and Werner S. A., 2004, "In situ neutron imaging technique for evaluation of water management systems in operating PEM fuel cells," J. Power Sources, **129**(2), pp. 238–245.
[77] Park J., Li X., Tran D., Abdel-Baset T., Hussey D. S., Jacobson D. L., and Arif M., 2008, "Neutron imaging investigation of liquid water distribution in and the performance of a PEM fuel cell," Int. J. Hydrog. Energy, **33**(13), pp. 3373–3384.
[78] Spernjak D., Advani S. G., and Prasad A. K., 2009, "Simultaneous Neutron and Optical Imaging in PEM Fuel Cells," J. Electrochem. Soc., **156**(1), pp. B109–B117.
[79] Manke I., Hartnig C., Grünerbel M., Lehnert W., Kardjilov N., Haibel A., Hilger A., Banhart J., and Riesemeier H., 2007, "Investigation of water evolution and transport in fuel cells with high resolution synchrotron x-ray radiography," Appl. Phys. Lett., **90**(17), pp. 174105–174105–3.
[80] Lee S.-J., Kim S.-G., Park G.-G., and Kim C.-S., 2010, "Quantitative visualization of temporal water evolution in an operating polymer electrolyte fuel cell," Int. J. Hydrog. Energy, **35**(19), pp. 10457–10463.
[81] Deevanhxay P., Sasabe T., Tsushima S., and Hirai S., 2011, "Investigation of water accumulation and discharge behaviors with variation of current density in PEMFC by high-resolution soft X-ray radiography," Int. J. Hydrog. Energy, **36**(17), pp. 10901–10907.
[82] Markötter H., Haußmann J., Alink R., Tötzke C., Arlt T., Klages M., Riesemeier H., Scholta J., Gerteisen D., Banhart J., and Manke I., 2013, "Influence of cracks in the

microporous layer on the water distribution in a PEM fuel cell investigated by synchrotron radiography," Electrochem. Commun., **34**, pp. 22–24.
[83] Sasabe T., Tsushima S., and Hirai S., 2010, "In-situ visualization of liquid water in an operating PEMFC by soft X-ray radiography," Int. J. Hydrog. Energy, **35**(20), pp. 11119–11128.
[84] Tüber K., Pócza D., and Hebling C., 2003, "Visualization of water buildup in the cathode of a transparent PEM fuel cell," J. Power Sources, **124**(2), pp. 403–414.
[85] Zhan Z., Wang C., Fu W., and Pan M., 2012, "Visualization of water transport in a transparent PEMFC," Int. J. Hydrog. Energy, **37**(1), pp. 1094–1105.
[86] Jiao K., Park J., and Li X., 2010, "Experimental investigations on liquid water removal from the gas diffusion layer by reactant flow in a PEM fuel cell," Appl. Energy, **87**(9), pp. 2770–2777.
[87] Borrelli J., Kandlikar S., Trabold T., and Owejan, Jon, "Water transport visualization and two-phase pressure drop measurements in a simulated pemfc cathode minichannel," ICMM 2005, Toronto, Canada.
[88] Kandlikar S. G., Lu Z., Domigan W. E., White A. D., and Benedict M. W., 2009, "Measurement of flow maldistribution in parallel channels and its application to ex-situ and in-situ experiments in PEMFC water management studies," Int. J. Heat Mass Transf., **52**(7–8), pp. 1741–1752.
[89] Weng F.-B., Su A., Hsu C.-Y., and Lee C.-Y., 2006, "Study of water-flooding behaviour in cathode channel of a transparent proton-exchange membrane fuel cell," J. Power Sources, **157**(2), pp. 674–680.
[90] Yang H., Zhao T. S., and Cheng P., 2004, "Gas–liquid two-phase flow patterns in a miniature square channel with a gas permeable sidewall," Int. J. Heat Mass Transf., **47**(26), pp. 5725–5739.
[91] Zhang L., Bi X. T., Wilkinson D. P., Anderson R., Stumper J., and Wang H., 2011, "Gas–liquid two-phase flow behavior in minichannels bounded with a permeable wall," Chem. Eng. Sci., **66**(14), pp. 3377–3385.
[92] Hossain M., Islam S. Z., Colley-Davies A., and Adom E., 2013, "Water dynamics inside a cathode channel of a polymer electrolyte membrane fuel cell," Renew. Energy, **50**, pp. 763–779.
[93] English N. J., and Kandlikar S. G., 2006, "An Experimental Investigation into the Effect of Surfactants on Air-Water Two-Phase Flow in Minichannels," Heat Transf. Eng., **27**(4), pp. 99–109.
[94] Anderson R., 2012, "Characterization of gas-liquid two-phase flow in a proton exchange membrane fuel cell," University of British Columbia.
[95] Ding Y., Anderson R., Zhang L., Bi X., and Wilkinson D. P., 2013, "Simulations of two-phase flow distribution in communicating parallel channels for a PEM fuel cell," Int. J. Multiph. Flow, **52**, pp. 35–45.
[96] Cheah M. J., Kevrekidis I. G., and Benziger J. B., 2013, "Water Slug to Drop and Film Transitions in Gas-Flow Channels," Langmuir, **29**(48), pp. 15122–15136.
[97] Spernjak D., Prasad A. K., and Advani S. G., 2010, "In situ comparison of water content and dynamics in parallel, single-serpentine, and interdigitated flow fields of polymer electrolyte membrane fuel cells," J. Power Sources, **195**(11), pp. 3553–3568.
[98] Kandlikar S., Garimella S., Li D., Colin S., and King M. R., 2005, Heat Transfer and Fluid Flow in Minichannels and Microchannels, Elsevier.

[99] Anderson R., Wilkinson D. P., Bi X., and Zhang L., 2011, "Two-phase flow pressure drop hysteresis in an operating proton exchange membrane fuel cell," J. Power Sources, **196**(19), pp. 8031–8040.
[100] Lee J., Hinebaugh J., and Bazylak A., 2013, "Synchrotron X-ray radiographic investigations of liquid water transport behavior in a PEMFC with MPL-coated GDLs," J. Power Sources, **227**, pp. 123–130.
[101] Dunbar Z., and Masel R. I., 2007, "Quantitative MRI study of water distribution during operation of a PEM fuel cell using Teflon® flow fields," J. Power Sources, **171**(2), pp. 678–687.
[102] Minard K. R., Viswanathan V. V., Majors P. D., Wang L.-Q., and Rieke P. C., 2006, "Magnetic resonance imaging (MRI) of PEM dehydration and gas manifold flooding during continuous fuel cell operation," J. Power Sources, **161**(2), pp. 856–863.
[103] Gao B., Steenhuis T. S., Zevi Y., Parlange J.-Y., Carter R. N., and Trabold T. A., 2009, "Visualization of unstable water flow in a fuel cell gas diffusion layer," J. Power Sources, **190**(2), pp. 493–498.
[104] Hussaini I. S., and Wang C.-Y., 2009, "Visualization and quantification of cathode channel flooding in PEM fuel cells," J. Power Sources, **187**(2), pp. 444–451.
[105] Nirunsin S., and Khunatorn Y., 2010, "Quantification of Liquid Water Saturation in a Transparent Single Serpentine Cathode Flow Channel of PEM FC by Using Image Processing," J. Sustain. Energy Environ., (1), pp. 129 – 135.
[106] Carton J. G., Lawlor V., Olabi A. G., Hochenauer C., and Zauner G., 2012, "Water droplet accumulation and motion in PEM (Proton Exchange Membrane) fuel cell mini-channels," Energy, **39**(1), pp. 63–73.
[107] Lee D., and Bae J., 2012, "Visualization of flooding in a single cell and stacks by using a newly-designed transparent PEMFC," Int. J. Hydrog. Energy, **37**(1), pp. 422–435.
[108] Anderson R., Wilkinson D. P., Bi X., and Zhang L., 2010, "Two-phase flow pressure drop hysteresis in parallel channels of a proton exchange membrane fuel cell," J. Power Sources, **195**(13), pp. 4168–4176.
[109] Hellstern T., Gauthier E., Cheah M. J., and Benziger J. B., 2013, "The role of the gas diffusion layer on slug formation in gas flow channels of fuel cells," Int. J. Hydrog. Energy, **38**(35), pp. 15414–15427.
[110] Nishida K., Tanaka S., Tsushima S., and Hirai S., 2011, "Image Measurement of Water Droplets in Cathode of PEFC Based on Background Subtraction Method," ECS Transactions, pp. 419–428.
[111] Amphlett J. C., Mann R. F., Peppley B. A., Roberge P. R., and Rodrigues A., 1996, "A model predicting transient responses of proton exchange membrane fuel cells," J. Power Sources, **61**(1–2), pp. 183–188.
[112] Pukrushpan J. T., Peng H., and Stefanopoulou A. G., 2004, "Control-Oriented Modeling and Analysis for Automotive Fuel Cell Systems," J. Dyn. Syst. Meas. Control, **126**(1), pp. 14–25.
[113] Yan W.-M., Chu H.-S., Chen J.-Y., Soong C.-Y., and Chen F., 2006, "Transient analysis of water transport in PEM fuel cells," J. Power Sources, **162**(2), pp. 1147–1156.

[114] Wang Y., and Wang C.-Y., 2007, "Two-Phase Transients of Polymer Electrolyte Fuel Cells," J. Electrochem. Soc., **154**(7), p. B636.
[115] Meng H., 2007, "Numerical investigation of transient responses of a PEM fuel cell using a two-phase non-isothermal mixed-domain model," J. Power Sources, **171**(2), pp. 738–746.
[116] Corbo P., Migliardini F., and Veneri O., 2007, "Performance investigation of 2.4 kW PEM fuel cell stack in vehicles," Int. J. Hydrog. Energy, **32**(17), pp. 4340–4349.
[117] Hamelin J., Agbossou K., Laperrière A., Laurencelle F., and Bose T. ., 2001, "Dynamic behavior of a PEM fuel cell stack for stationary applications," Int. J. Hydrog. Energy, **26**(6), pp. 625–629.
[118] Tang Y., Yuan W., Pan M., Li Z., Chen G., and Li Y., 2010, "Experimental investigation of dynamic performance and transient responses of a kW-class PEM fuel cell stack under various load changes," Appl. Energy, **87**(4), pp. 1410–1417.
[119] Kim S., Shimpalee S., and Van Zee J. W., 2004, "The effect of stoichiometry on dynamic behavior of a proton exchange membrane fuel cell (PEMFC) during load change," J. Power Sources, **135**(1–2), pp. 110–121.
[120] Liu D., and Case S., 2006, "Durability study of proton exchange membrane fuel cells under dynamic testing conditions with cyclic current profile," J. Power Sources, **162**(1), pp. 521–531.
[121] Lin R., Li B., Hou Y. P., and Ma J. M., 2009, "Investigation of dynamic driving cycle effect on performance degradation and micro-structure change of PEM fuel cell," Int. J. Hydrog. Energy, **34**(5), pp. 2369–2376.
[122] Wu J., Yuan X. Z., Martin J. J., Wang H., Zhang J., Shen J., Wu S., and Merida W., 2008, "A review of PEM fuel cell durability: Degradation mechanisms and mitigation strategies," J. Power Sources, **184**(1), pp. 104–119.
[123] Schmittinger W., and Vahidi A., 2008, "A review of the main parameters influencing long-term performance and durability of PEM fuel cells," J. Power Sources, **180**(1), pp. 1–14.
[124] Jiang Zou, Wei-Mon Yan, and Xiao-Feng Peng, 2006, "Dynamic analysis of gas transport in cathode side of PEM fuel cell with interdigitated flow field," J. Power Sources, **159**(1), pp. 514–23.
[125] Um S., Wang C.-Y., and Chen K. S., 2000, "Computational Fluid Dynamics Modeling of Proton Exchange Membrane Fuel Cells," J. Electrochem. Soc., **147**(12), pp. 4485–4493.
[126] Tiss F., Chouikh R., and Guizani A., 2013, "Dynamic modeling of a PEM fuel cell with temperature effects," Elsevier Ltd, pp. 8532–8541.
[127] Yan W.-M., Chen F., Wu H.-Y., Soong C.-Y., and Chu H.-S., 2004, "Analysis of thermal and water management with temperature-dependent diffusion effects in membrane of proton exchange membrane fuel cells," J. Power Sources, **129**(2), pp. 127–137.
[128] Kim H., Cho C. Y., Nam J. H., Shin D., and Chung T.-Y., 2010, "A simple dynamic model for polymer electrolyte membrane fuel cell (PEMFC) power modules: Parameter estimation and model prediction," Int. J. Hydrog. Energy, **35**(8), pp. 3656–3663.

[129] Hwang S. S., Lee P. H., Jo S. H., Cha C. L., Hong S. W., Han S. S., and Koo J. Y., 2012, "Transient behavior of proton exchange membrane fuel cell under non-isothermal condition," Renew. Energy, **42**, pp. 54–59.
[130] Rabbani R. A., and Rokni M., 2013, "Dynamic characteristics of an automotive fuel cell system for transitory load changes," Sustain. Energy Technol. Assess., **1**(1), pp. 34–43.
[131] Chang S.-M., and Chu H.-S., 2006, "Transient behavior of a PEMFC," J. Power Sources, **161**(2), pp. 1161–1168.
[132] Wu H., Li X., and Berg P., 2007, "Numerical analysis of dynamic processes in fully humidified PEM fuel cells," Int. J. Hydrog. Energy, **32**(12), pp. 2022–2031.
[133] Natarajan D., and Van Nguyen T., 2001, "A two-dimensional, two-phase, multicomponent, transient model for the cathode of a proton exchange membrane fuel cell using conventional gas distributors," J. Electrochem. Soc., **148**(12), pp. A1324–A1335.
[134] Wang Y., and Wang C.-Y., 2005, "Transient analysis of polymer electrolyte fuel cells," Electrochimica Acta, **50**(6), pp. 1307–1315.
[135] Wang Y., and Wang C.-Y., 2006, "Dynamics of polymer electrolyte fuel cells undergoing load changes," Electrochimica Acta, **51**(19), pp. 3924–3933.
[136] Chen F., Su Y.-G., Soong C.-Y., Yan W.-M., and Chu H.-S., 2004, "Transient behavior of water transport in the membrane of a PEM fuel cell," J. Electroanal. Chem., **566**(1), pp. 85–93.
[137] Song D., Wang Q., Liu Z.-S., and Huang C., 2006, "Transient analysis for the cathode gas diffusion layer of PEM fuel cells," J. Power Sources, **159**(2), pp. 928–942.
[138] Zhiani M., and Majidi S., 2013, "Effect of MEA conditioning on PEMFC performance and EIS response under steady state condition," Int. J. Hydrog. Energy, **38**(23), pp. 9819–9825.
[139] Didierjean S., Lottin O., Maranzana G., and Geneston T., 2008, "PEM fuel cell voltage transient response to a thermal perturbation," Electrochimica Acta, **53**(24), pp. 7313–7320.
[140] Banerjee R., and Kandlikar S. G., 2014, "Liquid water quantification in the cathode side gas channels of a proton exchange membrane fuel cell through two-phase flow visualization," J. Power Sources, **247**, pp. 9–19.
[141] Yu S., and Jung D., 2008, "Thermal management strategy for a proton exchange membrane fuel cell system with a large active cell area," Renew. Energy, **33**(12), pp. 2540–2548.
[142] Endoh E., Terazono S., Widjaja H., and Takimoto Y., 2004, "Degradation Study of MEA for PEMFCs under Low Humidity Conditions," Electrochem. Solid-State Lett., **7**(7), pp. A209–A211.
[143] Incropera F. P., 2007, Fundamentals of heat and mass transfer, John Wiley.
[144] Soille P., 2003, Morphological image analysis: principles and applications, Springer, Berlin ; New York.
[145] Dougherty E. R., and Society of Photo-optical Instrumentation Engineers, 1992, An introduction to morphological image processing, SPIE Optical Engineering Press, Bellingham, Wash., USA.

[146] Solomon C., 2011, Fundamentals of digital image processing: a practical approach with examples in Matlab, Wiley-Blackwell, Chichester, West Sussex ; Hoboken, NJ.
[147] Lu Z., Daino M. M., Rath C., and Kandlikar S. G., 2010, "Water management studies in PEM fuel cells, part III: Dynamic breakthrough and intermittent drainage characteristics from GDLs with and without MPLs," Int. J. Hydrog. Energy, **35**(9), pp. 4222–4233.
[148] Banerjee R., See E., and Kandlikar S. G., 2013, "Pressure Drop and Voltage Response of PEMFC Operation under Transient Temperature and Loading Conditions," ECS Trans., **58**(1), pp. 1601–1611.
[149] Banerjee R., and Kandlikar S., 2014, "Two-phase pressure drop characteristics during low temperature transients in PEMFCs," Chicago.
[150] Banerjee R., and Kandlikar S. G., "Experimental investigation of two-phase flow pressure drop transients in polymer electrolyte membrane fuel cell reactant channels and their impact on the cell performance," J. Power Sources.
[151] Banerjee R., and Kandlikar S., "Two-phase pressure drop response during load transients in a PEMFC," Int. J. Hydrog. Energy.

10.Appendices

10.1PhD Program Checklist

- ✓ Admission to the program
- ✓ Successfully complete the foundation courses
- ✓ Register to take Qualifying Examination
- ✓ Pass the Qualifying Examination
- ✓ Submit a Program of Study
- ✓ Finish all required coursework
- ✓ Research and define dissertation research topic
- ✓ Submit an Advisory Committee form
- ✓ Meet with librarian for College of Engineering (WML)
- ✓ Write the dissertation proposal
- ✓ Register to take the Candidacy Examination (proposal defense)
- ✓ Pass the Candidacy Examination
- ✓ Continue your research
- ✓ Hold periodic reviews of your progress with your advisory committee
- ✓ Hold a Research Review Milestone Meeting
- ✓ Publish at least two papers during the course of research (at least one of with is refereed)
- ✓ Write your dissertation manuscript
- ✓ Register for graduation with Microsystems Engineering program office
- ✓ Register for the dissertation defense
- ✓ Pass the dissertation defense
- ✓ Submit thesis title to the Registrar
- ✓ Meet with program office to ensure completion of all certification requirement

10.2Air and Water Flow Rate Calculations – Ex-situ Experiments

Current Density = 0.1 – 3.0 A/cm^2

Active Area = 18.4 cm^2 0.00184 m^2

F = 96485 C/mol

Stoic = 2 (3 for current density of 0.1 A/cm^2)

N (no. of electrons per mole) = 4 (for air) and 2 (for water)

Molecular Wt. of Air = 28.97 g/mol

Molecular Wt. of Water = 18.02 g/mol

$$Air\ Flow\ Rate = \frac{\frac{iA}{nF}x\ Stoic}{0.21} x\ Molecular\ Wt. Of\ Air$$

$$Water\ Flow\ Rate = \frac{iA}{nF}\ x\ Molecular\ Wt. Of\ Air$$

Air Flow Rate for 0.1 A/cm^2 for stoic of 3 is 1.973x10^{-3} g/s or 1.973x10^{-6} kg/s.

Density of air (@STP) = 1.1614 kg/m^3

Air flow rate = 0.1006 slm = 101 sccm

Water generation = 9.54E-6 mol/s

Water flow rate = 1.72E-4 g/s = 0.000172 cm^3/s

= 0.0103 sccm (ml/min)

10.3 MATLAB Script for Area Coverage Ratio

The Area Coverage Ratio is obtained using two scripts. The first script is called 'Water Segmentation'. The second script being used is 'Data Reduction'.

Water Segmentation

```
function Water_Segmentation(directory_name)

% Updated by Rupak Banerjee

% Structuring element was changed from a rectangle of 20 x 5 to a disc % of radius 5.

%% Directory Processing

% directory_name = 'L:\existu_videos\Two_Phase\Temp40C_1\0RH\0p1Acm2';
Mask_Location='L:\Ex_Situ_DVP\Mask_Files';
Dry_Frame_Location='L:\Ex_Situ_DVP\Ave_Dry_Frame';
Output_Location=directory_name;
d_name=strcat(directory_name,'\*.avi');
Test_dir=dir(d_name);
File_Names={Test_dir.name};
Num_Videos=length(File_Names);

for k=1:Num_Videos

   % Load Video Name
   Video_Name=File_Names{k};
   % Determine Window from Video Name
   Window=str2double(Video_Name(7));

   % Get Mask and Dry frame for the window:
   if Window==1
      Mask=imread(strcat(Mask_Location,'\Window1_Mask_Final.tif'));
      Ref_im=imread(strcat(Dry_Frame_Location,'\Average_Dry_Window1.tif'));
   elseif Window==2
      Mask=imread(strcat(Mask_Location,'\Window2_Mask_Final.tif'));
      Ref_im=imread(strcat(Dry_Frame_Location,'\Average_Dry_Window2.tif'));
   elseif Window==3
      Mask=imread(strcat(Mask_Location,'\Window3_Mask_Final.tif'));
      Ref_im=imread(strcat(Dry_Frame_Location,'\Average_Dry_Window3.tif'));
   elseif Window==4
      Mask=imread(strcat(Mask_Location,'\Window4_Mask_Final.tif'));
      Ref_im=imread(strcat(Dry_Frame_Location,'\Average_Dry_Window4.tif'));
   end

   % Load the test video
   Test_Vid=mmreader(strcat(directory_name,'\',Video_Name));
   % Create the outputs
   % Output color video
   tmp=strfind(Video_Name,'.');
   tmp2=Video_Name(1:tmp-1);
   Video_Color=avifile(strcat(Output_Location,'\',tmp2,'proc','.avi'),'compression','iyuv','fps',30);
   Im_File_Name=strcat(Video_Name(1:tmp-1),'_Water_Seg.tiff');
```

```
Num_Frames=Test_Vid.NumberOfFrames;

% Allocation Proclamation!
im=zeros(size(read(Test_Vid,1)));
d=zeros(size(im,1),size(im,2));
d2=d;
d3=d;
d4=d;
d5=d;
d6=d;
d7=d;
d8=d;
d9=im;
Water_Pixels=zeros(Num_Frames,1);
Area_Coverage=Water_Pixels;
% Timing
tic

%% Segmentation
for k2=1:Num_Frames
   % Current Frame
   im=read(Test_Vid,k2);
   % Subtract Ref Frame
   d=double(im(:,:,2))-double(Ref_im);
   % Threshold ->  Needs to be adjusted if results are not satisfactory
   % d2=d<-20; Used in 23C data. Changed to -35 for 40C data.
   % 21 January 2013
   % Changed to -40 for 40C data on 27 January 2013
   % Updated to -45 as test case.
   d2=d<-45;
   % Mask to isolation Channels
   d3=d2.*Mask;
   % Remove connected cluster that are less than 100 pixels
   d4=bwareaopen(d3,100);
   % Fill in holes
   d5=imfill(d4,'holes');
   d6=imclose(d5,strel('disk',5));
   % Mask again for good measure
   d7=d6.*Mask;
   % Count the number of water pixels
   Water_Pixels(k2)=numel(find(d7));
   Area_Coverage(k2)=Water_Pixels(k2)/numel(find(Mask));

   % Store Segmentated frames

   if k2==1
      imwrite(logical(d7),strcat(Output_Location,'\',Im_File_Name),'compression','none');
   else
      imwrite(logical(d7),strcat(Output_Location,'\',Im_File_Name),'WriteMode','append');
   end

   % Prepare color frame for review with water as faint blue/purple
   d8=uint8(50*d7)+im(:,:,2);
   d9=cat(3,im(:,:,2),im(:,:,2),d8);
   Video_Color=addframe(Video_Color,d9);
```

```
    end

    % Print time and video number to command line
    strcat('Video',' ',num2str(k),' ','Took ',num2str(toc),' seconds')
    Video_Color=close(Video_Color);

end
```

Data Reduction

```
function Data_Reduction(directory_name)

%  Post-processing for water pixels and coverage ratio

% directory_name='L:\existu_videos\Two_Phase\Temp23C\0RH\0p1Acm2';
Mask_Location='L:\Ex_Situ_DVP\Mask_Files';
Output_Location=directory_name;
d_name=strcat(directory_name,'\*.tiff');
Test_dir=dir(d_name);
File_Names={Test_dir.name};
Num_images=length(File_Names);

for k=1:Num_images
    % current file
    Image_Name=File_Names{k};

    % Import the mask
    Window=str2double(Image_Name(7));
    if Window==1
        Mask=imread(strcat(Mask_Location,'\Window1_Mask_Final.tif'));
    elseif Window==2
        Mask=imread(strcat(Mask_Location,'\Window2_Mask_Final.tif'));
    elseif Window==3
        Mask=imread(strcat(Mask_Location,'\Window3_Mask_Final.tif'));
    elseif Window==4
        Mask=imread(strcat(Mask_Location,'\Window4_Mask_Final.tif'));
    end

    % How many pages are in the tiff
    Num_pages=size(imfinfo(strcat(directory_name,'\',Image_Name)),1);
    Water_pixels=zeros(Num_pages,1);
    Water_Coverage_Ratio=Water_pixels;

    % grab number of channel pixels from mask
    channel_pixels=numel(find(Mask));

    for k2=1:Num_pages
        im=imread(Image_Name,k2);
        Water_pixels(k2)=numel(find(im));
        Water_Coverage_Ratio(k2)=Water_pixels(k2)./channel_pixels;
    end

    Data_out=cat(2,Water_pixels,Water_Coverage_Ratio);
```

```
    Water_pixels_mean=mean(Water_pixels);
    Water_Coverage_Ratio_mean=mean(Water_Coverage_Ratio);

   % Store only Water Coverage Average for each window
   Vid_Num=mod(k,4);
   if Vid_Num==0
       Vid_Num=4;
   end

   Window_Data(Window,Vid_Num)=Water_Coverage_Ratio_mean;

   tmp=-1*ones(size(Water_pixels));
   tmp2=tmp;
   tmp(1)=Water_pixels_mean;
   tmp2(1)=Water_Coverage_Ratio_mean;
   Data_out=cat(2,Data_out,tmp,tmp2);

    Header={'Water_Pixels','   ','Water_Coverage_Ratio','   ','Mean_Water_Pixels','
','Mean_Water_Coverage_Ratio'};

    tmp3=strfind(Image_Name,'.');
    tmp4=Image_Name(1:tmp3-1);

    dlmwrite(strcat(tmp4,'_RawWaterData.txt'),Header,'delimiter','');
    dlmwrite(strcat(tmp4,'_RawWaterData.txt'),Data_out,'-append','delimiter',' ');

end

    % Write Overall data

    Window_Data_mean=mean(Window_Data,2);
    Window_Data_out=cat(2,Window_Data,Window_Data_mean);

    Header2={'Video1','          ','Video2','          ','Video3','          ','Video4','          ','Average'};

   dlmwrite(strcat(directory_name(end-6:end),'_mean_WCR.txt'),Header2,'delimiter','');
   dlmwrite(strcat(directory_name(end-6:end),'_mean_WCR.txt'),Window_Data_out,'-
append','delimiter','\t','precision',15);
```

10.4 MATLAB Script for Flow Pattern Identification

The flow pattern identification is conducted by the following algorithm. The algorithm is run directly after the Area Coverage Ratio algorithm showed in Appendix 10.3.

```
function flow_structure(directory_name)


%Function to differentiate the flow structures

% directory_name = 'F:\Flow_Structure_Identification';
Mask_Location='L:\Ex_Situ_DVP\Mask_Files';

proc_Videos = dir(strcat(directory_name,'\*_Water_Seg.tiff'));
proc_FileNames = {proc_Videos.name};
nVideos = length(proc_FileNames);
Header1 = {'Frame ',' # of Objects ','Slugs ','Film ',' Total Pixels ',' Slug Ratio ',' Film Ratio '};
Header2 = {'Object # ',' Obj Pix ',' Slug? ',' length of slug ',' slug pixel ',' film width ',' film pixel '};

for k = 1:nVideos
   % Pick the tiff file to work with
   Image_Name = proc_FileNames{k};
   Full_Image_Name = strcat(directory_name,'\',Image_Name);

   % Import the mask
   Window=str2double(Image_Name(7));
   if Window==1
      Mask=imread(strcat(Mask_Location,'\Window1_Mask_Final.tif'));
   elseif Window==2
      Mask=imread(strcat(Mask_Location,'\Window2_Mask_Final.tif'));
   elseif Window==3
      Mask=imread(strcat(Mask_Location,'\Window3_Mask_Final.tif'));
   elseif Window==4
      Mask=imread(strcat(Mask_Location,'\Window4_Mask_Final.tif'));
   end

   mask = im2double(Mask);

   % Length of tiff file
   Num_pages = size(imfinfo(Image_Name),1);

   %Allocating Data Matrices
   frames_data_matrix = zeros(Num_pages,7);

   for k2 = 1:Num_pages
      im = imread(Full_Image_Name,'Index',k2);

      %label connected objects
      [L,num] = bwlabel(im);
      num_obj = num;
      combined = imadd(L,mask);
      label_matrix = zeros(num_obj,7);
      data_out = zeros(1,7);      % Used to collect / collate data from label_matrix
```

```
%% loop for determining flow structure of objects

for k3 = 1:num_obj
   % This loop goes through each object and calculates film widht,
   % slug length and film / slug ratios

   obj = combined==k3+1;          % Single object being analysed
   obj_numpix = length(find(obj)); % # of pixels in object
   label_matrix(k3,1) = k3;       % Object #
   label_matrix(k3,2) = obj_numpix;% Pixels of object

   [r c] = find(combined==k3+1);

   ind = [r c];
   % Tried putting the ind[r c] directly, but started giving error
   row_min = min(ind(:,1));
   row_max = max(ind(:,1));
   rows = row_max - row_min;
   row = row_min;
   width = zeros(rows,4);
   k4=1;
   while row>=row_min && row<=row_max

      cols = combined(row,:); % All columns in that row
      b = find(cols==k3+1);   % Finds columns that have this object
      col_start = min(b);     % Starting point of object on that row
      col_end = max(b);       % Ending point of object on that row
      width(k4,1) = col_end - col_start+1;
      width(k4,2) = combined(row,col_start-1);
      width(k4,3) = combined(row,col_end+1);
      width(k4,4) = (width(k4,2))+(width(k4,3));
      k4=k4+1;
      row = row+1;
   end

   if min(width(:,4)) == 0
      % This is a slug
      % row = row_max+1;
      label_matrix(k3,3) = 1;
      label_matrix(k3,4) = rows;
      label_matrix(k3,5) = label_matrix(k3,2);
   else
      % This is a film
      % row = row+1;
      label_matrix(k3,3) = 0;
      label_matrix(k3,6) = max(width(:,1));
      label_matrix(k3,7) = label_matrix(k3,2);
   % No droplet case.
   end

end

pix_total = sum(label_matrix(:,2));
pix_slugs = sum(label_matrix(:,5));
```

```
        pix_films = sum(label_matrix(:,7));

        slug_ratio = pix_slugs/pix_total;
        film_ratio = pix_films/pix_total;
        % drop_ratio = pix_drops/pix_total;


        %% Output results per frame
        slugs = sum(label_matrix(:,3));
        % drops = sum(label_matrix(:,8));
        films = num_obj - slugs;

        frames_data_matrix(k2,1) = k2;          % Frame number
        frames_data_matrix(k2,2) = num_obj;     % # of objects
        frames_data_matrix(k2,3) = slugs;       % # of slugs
        frames_data_matrix(k2,4) = films;       % # of films
        % frames_data_matrix(k2,5) = drops;       % # of drops
        frames_data_matrix(k2,5) = pix_total;   % Total # of pixsls
        frames_data_matrix(k2,6) = slug_ratio;  % Slug ratio
        frames_data_matrix(k2,7) = film_ratio;  % Film ratio
        % frames_data_matrix(k2,9) = drop_ratio;  % Drop ratio

        data_out = cat(1,data_out,label_matrix);
    end

    tmp = strfind(Image_Name,'.');
    tmp2 = Image_Name(1:tmp-1);

    dlmwrite(strcat(tmp2,'_FilmData.txt'),Header1,'delimiter','');
    dlmwrite(strcat(tmp2,'_FilmData.txt'),frames_data_matrix,'-append','delimiter','\t');

    dlmwrite(strcat(tmp2,'_FilmDetails.txt'),Header2,'delimiter','');
    dlmwrite(strcat(tmp2,'_FilmDetails.txt'),data_out,'-append','delimiter','\t');

    data_out = 0;

    strcat('Video ','  ',num2str(k),'  ',' Took ',num2str(toc),' seconds')

end
```

10.5 MATLAB Script for Channel to Channel variation

The channel to channel variation among the channels was identified using the algorithm showed below.

```
function maldistribution(directory_name)
% Function to detect differences in channel to channel ACR

% directory_name = 'E:\Exsitu_Data\Temp23C_1\0RH\0p1Acm2';

Mask_Location='E:\Exsitu_Data\Ex_Situ_DVP\Mask_Files\23C_MaskFiles';

proc_Videos = dir(strcat(directory_name,'\*_Water_Seg.tiff'));
proc_FileNames = {proc_Videos.name};
nVideos = length(proc_FileNames);

Header1 = {'Frame ','Ch 1','Ch 2','Ch 3','Ch 4','Ch 5','Ch 6','Ch 7','Ch 8'};
Header2 = {'Ch 1','Ch 2','Ch 3','Ch 4','Ch 5','Ch 6','Ch 7','Ch 8'};

final_data = zeros(1,8);

for k = 2:nVideos
   % Pick the tiff file to work with
   Image_Name = proc_FileNames{k};
   Full_Image_Name = strcat(directory_name,'\',Image_Name);

   % Import the mask
   Window=str2double(Image_Name(7));
   if Window==1
      Mask=imread(strcat(Mask_Location,'\Window1_Mask_Final.tif'));
   elseif Window==2
      Mask=imread(strcat(Mask_Location,'\Window2_Mask_Final.tif'));
   elseif Window==3
      Mask=imread(strcat(Mask_Location,'\Window3_Mask_Final.tif'));
   elseif Window==4
      Mask=imread(strcat(Mask_Location,'\Window4_Mask_Final.tif'));
   end

   mask = im2double(Mask);
   % Label the mask. Channels are now numbered left to right.
   mask_l = bwlabel(mask);

   % Length of tiff file
   Num_pages = size(imfinfo(Image_Name),1);

   % Allocating Data Matrices
   data_out = zeros(Num_pages+1,9);
   channel_data = zeros(1,8);

   for k2 = 1:Num_pages
      % Loop to measure maldistribution
      im = imread(Full_Image_Name,'Index',k2);
      im = im2double(im);
      combined = imadd(mask_l,im);
```

```
        data_out(k2,1) = k2;
        data_out(k2,2) = numel(find(combined == 2)); % Channel 1
        data_out(k2,3) = numel(find(combined == 3)); % Channel 2
        data_out(k2,4) = numel(find(combined == 4)); % Channel 3
        data_out(k2,5) = numel(find(combined == 5)); % Channel 4
        data_out(k2,6) = numel(find(combined == 6)); % Channel 5
        data_out(k2,7) = numel(find(combined == 7)); % Channel 6
        data_out(k2,8) = numel(find(combined == 8)); % Channel 7
        data_out(k2,9) = numel(find(combined == 9)); % Channel 8

    end

    %% Calculating mean for the video
    channel_data(1,1) = mean(data_out(k2,2));
    channel_data(1,2) = mean(data_out(k2,3));
    channel_data(1,3) = mean(data_out(k2,4));
    channel_data(1,4) = mean(data_out(k2,5));
    channel_data(1,5) = mean(data_out(k2,6));
    channel_data(1,6) = mean(data_out(k2,7));
    channel_data(1,7) = mean(data_out(k2,8));
    channel_data(1,8) = mean(data_out(k2,9));

    final_data = cat(1,final_data,channel_data);

    %% Writing output file for the video
    dlmwrite(strcat(Image_Name(1:end-5),'_channel_acr.txt'),Header2,'delimiter','\t');
    dlmwrite(strcat(Image_Name(1:end-5),'_channel_acr.txt'),channel_data,'-append','delimiter','\t');

    dlmwrite(strcat(Image_Name(1:end-5),'_frame_acr.txt'),Header2,'delimiter','\t');
    dlmwrite(strcat(Image_Name(1:end-5),'_frame_acr.txt'),data_out,'-append','delimiter','\t');

end
```

10.6 Data for two-phase pressure drop overshoot behavior

Test #	Temperature	Ramp Rate	Amplitude	Starting Current	Ending Current	Peak Pressure	Steady Pressure	Time to SS	% Overshoot
	°C	*A/s*	*A/cm^2*	*A*	*A*	*kPa*	*kPa*	*seconds*	*%*
1	40	0.1	0.2	10	20	2.15	1.55	1224	38.74
2	40	0.1	-0.2	20	10	0.78	1.12	1072	30.22
3	40	0.3	0.2	10	20	2.35	1.68	713	40.16
4	40	0.3	-0.2	20	10	0.74	1.13	711	34.84
5	40	0.5	0.2	10	20	2.42	1.76	358	37.56
6	40	0.5	-0.2	20	10	0.75	1.13	1215	33.64
7	40	0.9	0.2	10	20	2.48	1.72	642	43.74
8	40	0.9	-0.2	20	10	0.74	1.20	2515	38.18
9	40	0.1	0.1	10	15	1.76	1.42	799	23.89

10	40	0.1	-0.1	15	10	0.89	1.17	1554	24.09
11	40	0.1	0.3	10	25	2.60	1.92	322	35.92
12	40	0.1	-0.3	25	10	0.75	1.25	2112	39.92
13	40	0.1	0.4	10	30	3.24	2.56	226	26.53
14	40	0.1	-0.4	30	10	0.75	1.32	1670	42.94
15	40	0.7	0.2	10	20	2.48	1.75	594	41.37
16	40	0.7	-0.2	20	10	0.77	1.20	1903	35.46
17	40	0.3	0.4	10	30	3.53	2.50	418	41.03
18	40	0.3	-0.4	30	10	0.67	1.11	1412	39.91
19	40	0.3	0.1	10	15	1.77	1.43	685	23.98
20	40	0.3	-0.1	15	10	0.87	1.10	575	20.62
21	40	0.3	0.3	10	25	2.83	2.00	336	41.61
22	40	0.3	-0.3	25	10	0.70	1.18	2306	40.93

23	40	0.5	-0.4	30	10	0.65	1.21	2122	46.44
24	40	0.5	0.1	10	15	1.76	1.47	555	19.34
25	40	0.5	-0.1	15	10	0.90	1.12	698	20.14